## UNIVERSITÀ DEGLI STUDI FIRENZE

International Doctorate in
Atomic and Molecular Photonics

CYCLE XXXVI

COORDINATOR Prof. Diederik S. Wiersma

# Development of an optical system for three-dimensional multicolour super-resolution microscopy and its application to the study of subcellular compartmentalization

Academic Discipline (SSD) FIS/03

**Candidate**
Chiara Caldini

**Coordinator**
Prof. Diederik S. Wiersma

**Supervisor**
Prof. Francesco Saverio Pavone

**Co-Supervisor**
Dr. Lucia Gardini

Years 2020/2023

# Contents

# Introduction

Over the last decades, the field of optical microscopy has been completely revolutionized by the development of super-resolution microscopy. Super-resolution microscopy encloses all the microscopic techniques (STORM, PALM, STED… etc.) that bypass the diffraction limit and increase the spatial resolution by an order of magnitude with respect to conventional light microscopy. Each of these techniques has inherent advantages and limitations when applied to different biological questions.

Among the various existing super-resolution microscopy methods, Photo-Activated Localization Microscopy (PALM) and Stochastic Optical Reconstruction Microscopy (STORM) are those that achieve the highest image resolution thanks to their capability to localize single molecules with few tens of nanometers' accuracy in the three dimensions. Thanks to these techniques it is now possible to observe previously unresolved details of cellular structures and to elucidate biological processes at the molecular scale.

However, despite the remarkable improvement in resolution when compared to conventional optical microscopy, there are still some challenges to be faced. Currently, performing multicolour super-resolution imaging is not trivial. In fact, despite the availability of several commercial setups for multicolour super-resolution microscopy, achieving reliable results requires fine correction of all potential aberrations and artifacts that could significantly impact the outcomes. Moreover, multicolour super-resolution imaging is even more challenging in small volume samples, such as bacterial cells, as the aforementioned corrections must be at the nanoscale level.

This doctoral dissertation reports my work on developing and characterizing an optical system for three dimensional multicolours

super-resolution microscopy with nanometers accuracy. In the first chapter, after introducing the concept of diffraction limit and explaining the principles behind super-resolution microscopy, I compare the benefits and limitations of different super-resolution techniques and focus on the ongoing challenges. In the second chapter, after elucidating the main critical issues of multicolour super-resolution imaging – mechanical and thermal drifts, crosstalk and chromatic aberrations – I describe the development and characterization of a multicolours super-resolution setup explaining in detail the methods I developed to overcome these technical difficulties. In the third chapter, I show how I used our setup to study the sub-cellular organization in bacteria. In particular, I studied the spatial distribution of two interacting proteins (HisH, HisF) of the histidine metabolic pathway in engineered *Escherichia Coli* (E. Coli) bacteria in which each protein of interest is tagged with a photoactivable fluorescent protein (PAmCherry1-HisH, PAGFP-HisF) and thus can be imaged and localized. After explaining how to prepare the sample and to perform the acquisitions, I describe the analysis method I developed to identify co-localizing pairs of molecules and estimate the distance between them. To prove the reliability of the algorithm, I applied it to both simulated and real data and checked the consistency of the results. Finally, in chapter four, I show the effort to further improve the resolution of the system by combining two super-resolution techniques, Expansion Microscopy (ExM) sample preparation protocol and PALM imaging process, to reach the nanometer accuracy in the three dimensions.

# Chapter 1

# Super-resolution microscopy

Advancements in microscopy have consistently contributed to unravelling the complexities of cell functions and subcellular processes. A substantial portion of our comprehension concerning cellular and subcellular biological processes has arisen from our capability to directly observe and visualize them. Since its development, fluorescence microscopy has become an invaluable tool for understanding biological systems' inner mechanisms because of its two principal advantages: distinct cellular elements may be observed through molecule-specific labelling, and light microscopy allows real-time observation of structures within a living specimen [1], [2].

Although fluorescence microscopy provides multiple approaches to visualize different aspects of biological structures and activities, classical optical microscopes have an intrinsic spatial resolution limitation due to the wave nature of light, as first reported by Ernst Abbe in 1873 [3]. Since light propagates as an electromagnetic wave, it cannot be focused to an area smaller than the half of its wavelength, as shown in **Figure 1.1**, which directly determines the dimensions of
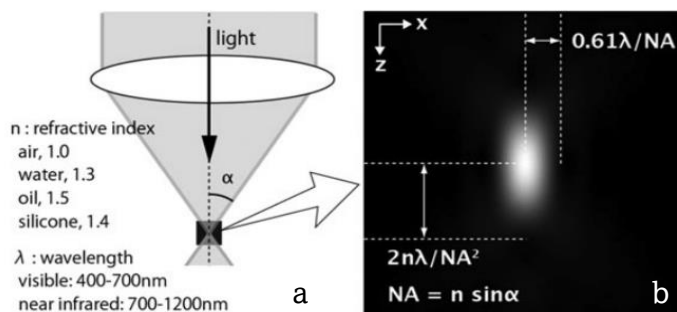


**Figure 1.1: (a)** Light distribution for focused light; **(b)** Abbe's law: light with wavelength $\lambda$, traveling in a medium with refractive index n and converging to a spot with half-angle $\theta$ will have a minimum resolvable lateral and axial distances of $\lambda/2n\sin\theta$ and $2n\lambda/(n\sin\theta)^2$. Image retrieved from [4].

the smallest structures that can be resolved. This limitation, known as *diffraction limit*, depends on the wavelength of light $\lambda$ used to create the image – the longer the wavelength, the larger the distance, the lower the resolution – and on the numerical aperture of the microscope objective $NA$. For visible light microscopy the diffraction limit sets to about 200–300 nm in the lateral direction and 500–700 nm in the axial direction. Since it is comparable to or larger than many subcellular structures, it makes hard to observe them in detail [4]. Yet, in recent years, several "super-resolution" fluorescence microscopy techniques have been developed to overcome the diffraction barrier. These methods have led to a significant enhancement in spatial resolution by an order of magnitude in all three dimensions compared to traditional light microscopy. The observation of previously unresolved details of cellular structures has proven the immense potential of super-resolution fluorescence microscopy in elucidating biological processes at the cellular and molecular scale [4], [5].

In this chapter, I will describe the principles of super-resolution optical microscopy, the advantages and the limitations of currently the available techniques as well as the ongoing challenges to be faced.

## 1.1 Diffraction limit and optical resolution

In nineteenth century, the German physicist Ernst Abbe demonstrated that the resolution of an optical system is limited by the diffraction of light. Diffraction comes from the wave nature of light and the finite size of the optical elements. When light passes through a circular aperture, it is diffracted creating a diffraction pattern with a central spot, surrounded by bright rings, which is known as the *Airy disk* [6]. The angular radius of the Airy disk is given by:

$$\theta \approx 1.22 \frac{\lambda}{D} \tag{1.1}$$

where $\theta$ is the angular resolution in radians, $\lambda$ is the wavelength of light in meters and $D$ is the diameter of the lens aperture in metres.
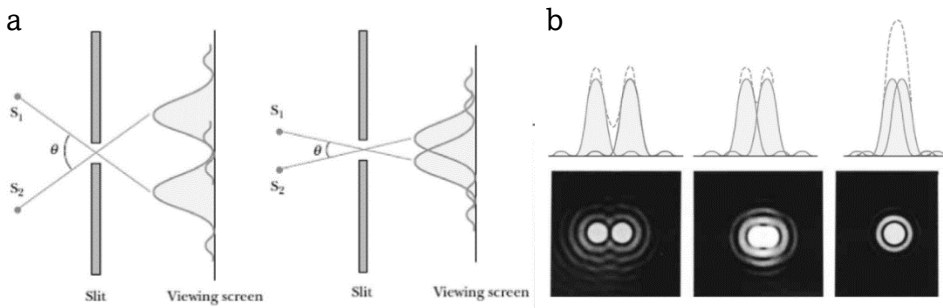
Figure 1.2: (a) Diffraction pattern generated by the light of two point-like sources passing through a circular aperture; (b) Rayleigh criterion: points whose distance is greater than (left) or equal to the Rayleigh limit (middle) can be resolved, points closer than the criterion (right) are indistinguishable.

Since two adjacent points give rise to two diffraction patterns, if their angular separation is greater than or equal to the Airy disk angular radius distinct images of the two points are formed and they can be resolved, otherwise not (*Rayleigh criterion*, **Figure 1.2**) [7], [8]. Thanks to the Rayleigh criterion, knowing the wavelength of the observed light and the diameter of the aperture, we can obtain the minimum distance between two point-like sources for them to be optically resolvable.

In an optical microscope, the objective lens acts like a circular aperture and so every point-like source of light in the observed sample will appear as an Airy disk pattern in the final image. The three-dimensional representation of the Airy disk is called *point spread function* (PSF) (see **Figure 1.3**). Experimentally, the size of the PSF determines the resolution of the microscope: if two points are closer than the *full width at half-maximum* (FWHM) of the PSF, their images overlap and they won't be distinguishable. Following *Abbe's law*, the FWHM of the PSF in the lateral (perpendicular to the optical axis) and axial directions can be approximated as:

$$\Delta xy \approx \frac{\lambda}{2NA} \tag{1.2}$$

$$\Delta z \approx \frac{2\lambda}{(NA)^2} \tag{1.3}$$
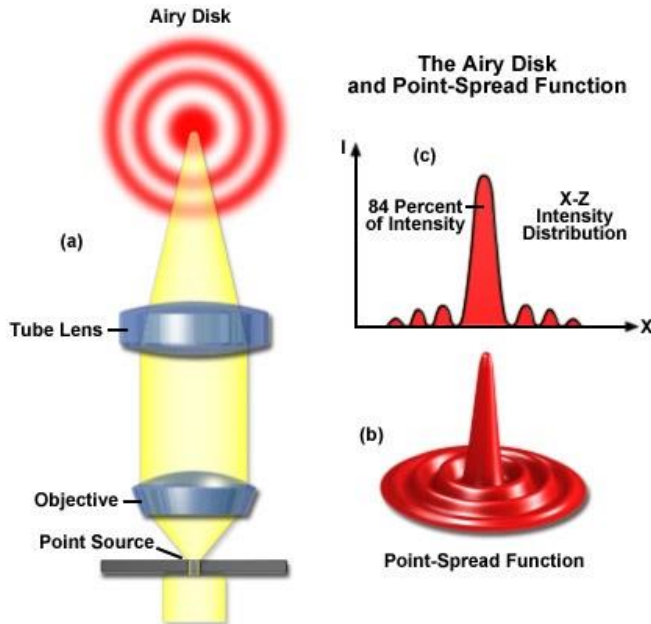
**Figure 1.3:** Airy disk and point spread function produced because of the propagation of the light emitted from a point-like source through a microscope. Image retrieved from [9].

where $\lambda$ is the wavelength of the light, and $NA$ is the numerical aperture of the objective defined as $NA = n \sin \theta$, with $n$ being the refractive index of the medium and $\theta$ being the half-cone angle of the focused light produced by the objective. The axial width of the PSF is about 2–3 times as large as the lateral width for ordinary high NA objectives. When imaging with visible light ($\lambda \approx 550$ nm), the commonly used oil immersion objective with NA = 1.40 yields a PSF with a lateral size of ~200 nm and an axial size of ~500 nm in a refractive index-matched medium [6], [9]. This resolution is sufficient to image features such as organs or tissues, but it's not enough for studying those subcellular structures with sizes much smaller than the wavelength of light. Super-resolution microscopy arises from the need to improve the spatial resolution of traditional fluorescence microscopy without compromising its non-invasiveness and biomolecular specificity.

Over the last twenty years, multiple microscopic techniques have been developed to overcome the diffraction limit and allow imaging of

biological sub-cellular structures, such as nuclear pores, viruses, chromatin complexes, cytoskeletal filaments...etc., with few nanometers resolution [10]. Current super-resolution microscopies break the diffraction limit by either temporally or spatially modulating the excitation or the activation of light. Therefore, they are often divided between patterned excitation methods and localization-based methods.

## 1.2 Super-resolution by spatially patterned excitation

One approach to overcome the diffraction limit is to incorporate sub-diffraction-limit features into the excitation pattern so that fine-scale information can be retrieved. We refer this method, including Stimulated Emission Depletion (STED) microscopy and Structured Illumination Microscopy (SIM), as super-resolution microscopy by spatially patterned excitation.

### 1.2.1 Stimulated Emission Depletion (STED) microscopy

STimulated Emission Depletion (STED) microscopy employs stimulated emission to confine fluorescence emission to a small region within the broader excitation laser spot [11]. As shown in **Figure 1.4a**, STED microscopy excites the fluorescent probes in the sample with focused laser light. Before the spontaneous emission of fluorescence occurs – within only few ns –, a second red-shifted doughnut-shaped beam with zero intensity in the central part illuminates the sample, depleting the emission of fluorophore outside the central region. Since the depletion beam could potentially excite the fluorophore, it shouldn't be too close to the absorption band. This second beam, known as the STED beam, forces fluorophores from their excited electronic state back to their ground state by stimulating the emission of a photon of the same wavelength. By applying a wavelength filter to remove the stimulated emission and the STED beam, we can selectively detect only the spontaneous emission coming from the
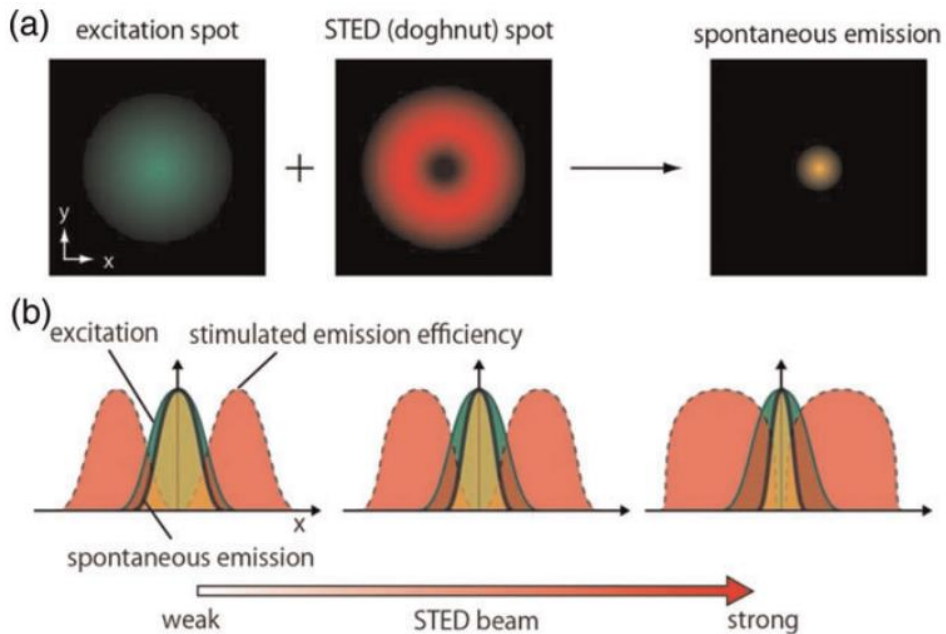
**Figure 1.4: (a)** Principle of the resolution improvement in STED microscopy; **(b)** Saturation effect in stimulated emission reduces the region for spontaneous emission. Image retrieved from [4].

central area of the excitation spot where fluorophores have not been quenched. Although both excitation and STED beams are pulsed lasers and they are synchronized, the depletion pulse is temporally extended relative to the other, thus generating "de-excitation" outside the central spot. By overlapping these two beams, fluorescence emission is only permitted from the central region, resulting in the creation of a much smaller effective excitation focal spot. In practice, it's impossible to achieve 100% depletion of spontaneous emission using the STED beam, but 90% to 95% depletion is often sufficient to generate images with a high contrast ratio. Employing this principle, researchers have managed to reach up to a tenfold enhancement in resolution along one dimension [12].

**Figure 1.5** shows fluorescence images of neurofilaments in human neuroblastoma observed by confocal (**Figure 1.5a**) and STED microscopy (**Figure 1.5b**). As we can see from the image, STED microscopy significantly enhances the spatial resolution, enabling the fine visualization of small structures that couldn't be resolved in the

8
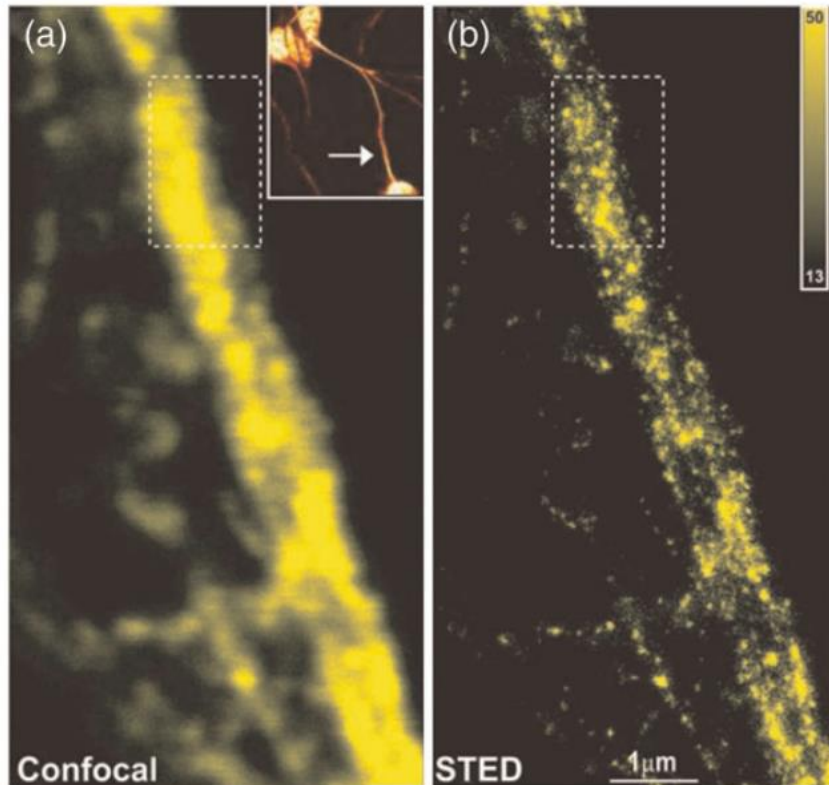
**Figure 1.5:** Neurofilaments in human neuroblastoma observed by confocal **(a)** and STED microscopy **(b)**. Image retrieved from [16].

confocal image. The spatial resolution of STED microscopy is strictly related to the size of the area where the spontaneous emission is allowed, which in turn depends on the size of the doughnut hole of the STED beam. Since the doughnut hole is produced by interference of light waves its size cannot be smaller than the half the STED beam wavelength, and the corresponding spatial resolution is equivalent to that of confocal microscopy. However, by increasing the intensity of the STED beam, also fluorophores at the inner ring of the doughnut can be switched off and this can produce a central fluorescent spot smaller than the diffraction limit (as shown in **Figure 1.4b**). Yet, achieving this enhanced resolution requires laser powers approximately 1000 times greater than those used in conventional confocal microscopy. While theoretically, there's no strict resolution limit to STED images, in practical biological applications, there's a

constraint imposed by the photo-damage risk for biological samples due to the high laser intensities required. Thus, the intensity limit on the depletion beam in biological contexts is often set by the need to preserve the integrity and viability of the samples being studied. Usually STED achieves 20–70 nm resolution when imaging fixed biological samples labelled with either synthetic dyes or fluorescent proteins. Moreover, STED can also be applied in 3D using two STED beams to improve xy and z resolutions at the same time [13].

The complexity of the STED system limits fluorophore choices and can make multicolour imaging difficult. Multicolour imaging can be challenging because two laser wavelengths are required for each dye: a conventional excitation laser beam and a red-shifted doughnut-shaped STED beam. This means that for dual-colour imaging, four laser beams, each with a different wavelength, would be required which easily produce undesired interference and create even greater photobleaching issues. Nevertheless, multicolour STED imaging has been achieved in some cases [14], [15]. To simplify two-colour imaging, one approach involves combining a fluorophore with a second fluorophore that has a similar emission spectrum but a larger Stokes shift between excitation and emission wavelengths. In this way, only a single STED laser for both dyes is required [16].

Live-cell imaging can be challenging too due to the phototoxic effects of the added STED beam. While the excitation laser power is comparable to that used in conventional confocal microscopy, the STED laser power can be around 1000 times higher, which can lead to significant photobleaching and photodamage [17], [18]. Nonetheless, it has been demonstrated that using fast scanning techniques and selecting the appropriate STED wavelength can minimize these effects [18], [19]. Fast beam scanners enable live-cell imaging in small regions, typically of few microns in size, at speeds of 60 to 80 frames per second with reduced photobleaching and phototoxicity [19], [20].

## 1.2.2 Structured Illumination Microscopy (SIM)

The concept of super-resolution imaging by structured illumination was first introduced by Lukosz for brightfield microscopy [21] and then implemented in fluorescence microscopy [22]. Structured Illumination Microscopy (SIM) is based on widefield microscopy and is compatible with standard fluorophores and labelling protocols. What sets SIM apart from conventional fluorescence microscope is the illumination pattern. SIM use a structured grid-like pattern to excite the whole field of view [22]. When a high spatial frequency grid is projected onto a sample and the emission from fluorophores is detected, it results in a certain degree of blurring in the observed fluorescence. This blurring is a consequence of the interaction between the excitation pattern, which is the grid in this case, and the spatial pattern of the sample being imaged. When these two patterns combine, they give rise to an interference pattern known as *moiré fringes*, shown in **Figure 1.6b**. These fringes, while coarser than the individual patterns they arise from, contain valuable information that can be analyzed to extract high-resolution details about the sample's structure. Knowing the position and the period of the illumination grid, information of the fine structure can be recovered from the moiré fringes. Whereas, in conventional fluorescence microscopy, the fine
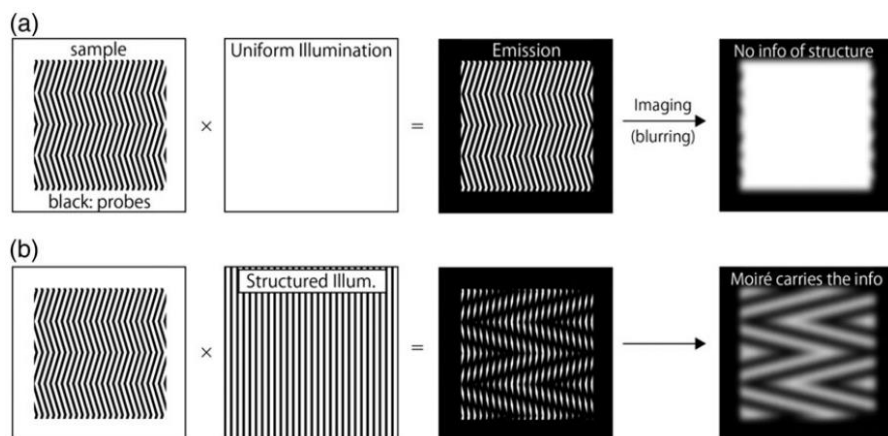


**Figure 1.6:** Comparison of image formation between conventional widefield (a) and (b) SIM. Image retrieved from [4].
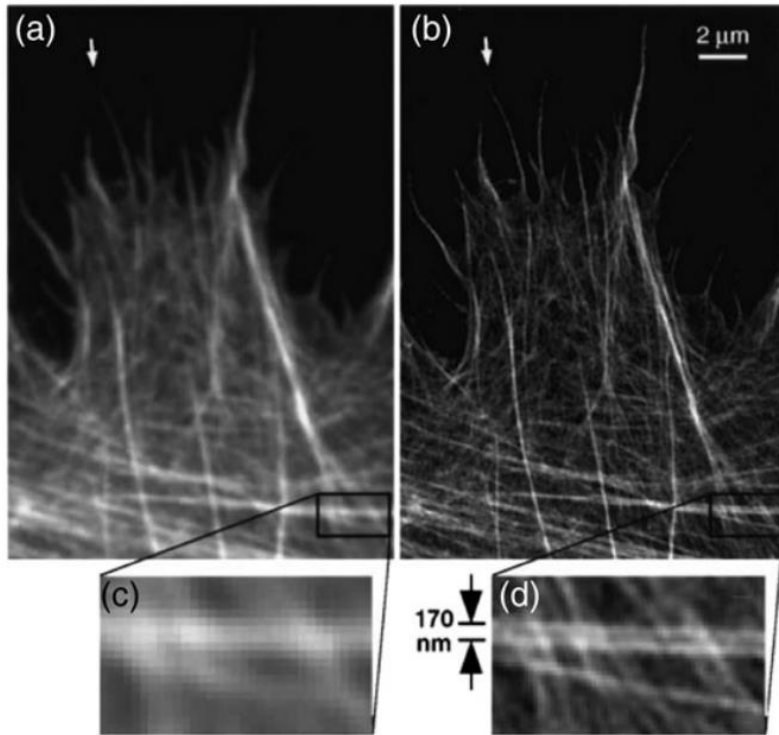
**Figure 1.7:** Actin cytoskeleton observed by conventional widefield **(a)** and structured illumination microscopy **(b)**. Image retrieved from [22].

structures cannot be recovered because they are fundamentally missing from the imaging process (**Figure 1.6a**). **Figure 1.7** compares images of actin cytoskeleton observed by conventional widefield (**Figure 1.7a**) and SIM (**Figure 1.7b**).

The improvement of the spatial resolution in SIM can be understood more clearly using mathematics [4]. **Figure 1.8** shows the mathematical view of image formation in conventional fluorescence microscopy and SIM. In conventional microscopy (**Figure 1.8a**), the output image is given by the convolution of the sample's fluorescence emission pattern and the point spread function of the imaging optics. This corresponds to applying a low pass filter to the emission distribution. Since the high spatial-frequency components, which represent small structures in the sample, are cutoff by the low-pass filtering, they cannot be recovered even by post-processing of the image. On the other hand, in SIM (**Figure 1.8b**), the high spatial-frequency

components remain in the resultant images because the grid illumination shifts the high spatial-frequency components near to the direct current (DC) frequency, allowing them to pass through the low-pass filter intrinsic in the image formation. This frequency shift is seen as the moiré fringes, in which the high- and low frequency components are overlapped. Since high frequency components contain information about the fine structure, to get a super-resolution image they must be separated from the low ones. Thanks to an inverse Fourier transform the components are extracted and the final image with high spatial-frequency information is reconstructed. SIM spatial resolution can be improved at maximum by a factor of 2 with respect to conventional microscopy [23]. As shown in **Figure 1.8b**, the convolution of
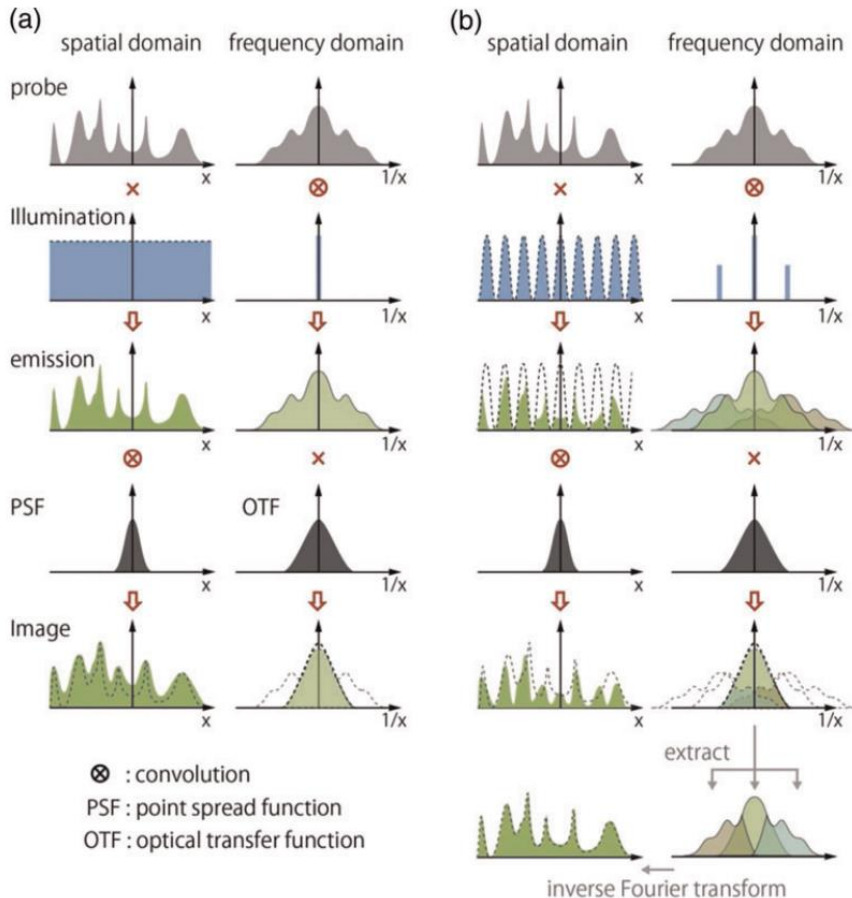


**Figure 1.8**: Image formation in conventional wide-field **(a)** and structured illumination microscopy **(b)**. Image retrieved from [4].

frequencies between the illumination pattern and the sample causes the shift from high- to low frequency components that can be imaged through the low-pass filter. Theoretically, the finer is the illumination grid, the higher should be the resolution. However, since the illumination pattern itself is produced by the objective lens, the periodicity of the grid pattern is also limited by diffraction. Therefore, the finest grid corresponds to the smallest structure resolvable by conventional microscopy, and the maximum frequency shift is located at the edge of the low-pass filter. Under these conditions, the extent of the frequency shift corresponds to the bandwidth of the imaging system in conventional microscopy, and the maximum resolution improvement is hence a factor of 2.

SIM can also be performed in three dimensions employing three-beam interference to extend the 2D illumination pattern into 3D [24], by using side illumination – either light sheet or Bessel beam illumination – to create the structured pattern [25] or placing a mirror directly opposite the sample to enable four-beam interference [26]. Based on the method chosen to perform 3D SIM, the resolution can be around 100-130 nm in xy and 160-300 nm in z. Multicolour SIM can be easily performed too. Using multicolour 3D SIM, the structures of chromatin and colocalization of single nuclear pore complexes and nuclear laminas in a mammalian cell were observed [27]. Investigations of immune synapses in natural killer cell [28], intermediate states of abscission in human cells [29] and pericentriolar material in the centrosome [30], [31] were also performed. Furthermore, SIM is currently the most widely used super-resolution technique for live-cell imaging and has been applied to a broad range of biological studies, including, for example, live-cell 2D SIM imaging of microtubules [32]. A difficulty encountered with live-cell SIM is that 9 to 15 recorded frames are required to image the sample. If the object in question moves even slightly during image acquisition, artefacts are created that can prevent a reliable reconstruction.

## 1.3 Super-resolution by single-molecule localization

Super-resolution techniques based on single-molecule localization relies on the detection of fluorescence emitted from individual fluorophores, followed by the precise determination of their molecular positions. Although localizing single molecule with nanometers accuracy has been done for many years [33], [34], [35], it wasn't considered a standalone microscopy technique because in densely labelled structures diffraction-limited images of single fluorophores overlap and single molecule imaging cannot be performed. Localization-based super-resolution microscopies, such as Stochastic Optical Reconstruction Microscopy (STORM) and Photo-Activated Localization Microscopy (PALM), have been developed independently to address this limitation and enable breakthroughs in imaging. Before delving into PALM and STORM microscopy, we'll see how it is possible to localize single fluorescence emitters.

### 1.3.1 Single-molecule localization

As discussed in section 1.1, the resolution of a visible light microscope is commonly taken to be about $\lambda/2 \approx 250\, nm$, with any sparse objects smaller than this dimension appearing in the microscope as diffraction-limited spots. Although the details within a spot are not resolvable, the center of the spot, and hence the position of the object, can be determined to a much greater precision. When the image consists of a collection of sparse, punctate objects, it is therefore possible to determine the relative positions of the objects with a precision much better than the wavelength of light, thus overcoming the limitations on the resolution.

As already seen, the three-dimensional diffraction pattern (the PSF) generated by a point-like source on the focal plane of an optical system can be described by an Airy function. However, when imaging a single fluorescent emitter only the central part of the diffraction pattern is detected, because the external rings, surrounded by the
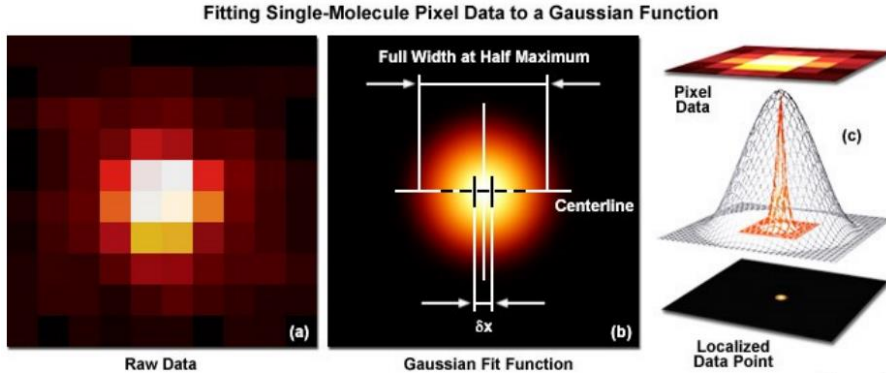
**Figure 1.9:** Schematic illustration of the 2D single-molecule localization process. The image of a single emitter **(a)** is fitted with a two-dimensional Gaussian function and localized with nanometer accuracy ($\delta x$) **(b)**. The entire process is summarized in **(c)**, where the standard deviation of the orange Gaussian is equal to $\delta x$. Image retrieved from [37].

background fluorescent signal, become undetectable over the background. Based on this observation, it has been demonstrated that the intensity profile created on the focal plane of an optical system by a sub-diffraction sized fluorescent probe can be approximated with a two-dimensional Gaussian function [36], [37], [38]. Thus, by fitting the PSF of a single fluorescent emitter with a bidimensional gaussian, it is possible to establish the xy position of the molecule as the coordinates of the centroid of the Gaussian function fitted to the data. Bidimensional single-molecule localization process is reported in **Figure 1.9**.

To extract the position of the molecule from the region of interest (ROI) two different computational fitting algorithm can be used: the *least squares method* (LSM) and the *maximum likelihood estimation* (MLE). Both methods have different performance limits. Given the standard deviation of the gaussian fitted function in nm ($\sigma$), the pixel size in nm ($a$), the number of detected photons for a given molecule ($N$) and the background signal calculated as standard deviation of the residuals between the raw data and the fitted function ($b$), the uncertainty of the lateral position of a molecule can be estimated as:

$$(\Delta xy_{LSM})^2 = \frac{\sigma^2 + a^2/12}{N}\left(\frac{16}{9} + 4\tau\right) \qquad (1.4)$$

16
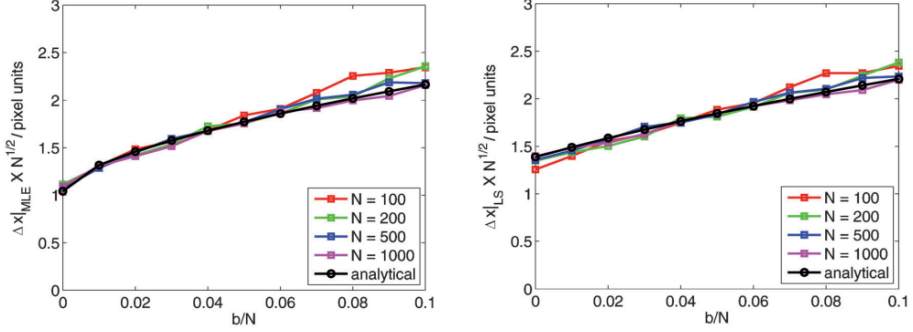
**Figure 1.10:** Simulation results for the localization uncertainty scaled with $\sqrt{N}$ for the MLE (left) and LSM (right) as a function of relative background level b/N for different signal photon counts N. Image retrieved from [41].

$$(\Delta xy_{MLE})^2 = \frac{\sigma^2 + a^2/12}{N}\left(1 + 4\tau + \sqrt{\frac{2\tau}{1+4\tau}}\right) \qquad (1.5)$$

With

$$\tau = \frac{2\pi b(\sigma^2 + a^2/12)}{a^2 N} \qquad (1.6)$$

The uncertainty for least-squares estimate is also known as the Thompson-Larson-Webb formula [39], altered with the correction factor of "16/9" as suggested by Mortensen et al. [40], while the uncertainty for maximum-likelihood was derived by Rieger and Stallinga [41]. Since the performance limit of the MLE method corresponds to the *Cramer–Rao lower bound* (CRLB), i.e. the best possible variance of an unbiased estimator, MLE is always superior to the LSM for low background levels as shown in **Figure 1.10** [41], [42].

In both methods, localization uncertainty depends upon many parameters. From equations (1.4) and (1.5) we get that the position uncertainty can be reduced by either employing optics and wavelengths to produce a smaller PSF ($\sigma$), or by minimizing the fluorescence background noise (*b*) through short band filters and careful illumination design to reduce the excited volume, or by maximizing the number of detected photons (N) by choosing bright fluorophores, high numerical aperture objectives and very sensitive cameras, such as Electron Multiplying CCD (EMCCD) cameras with

single-photon sensitivity. The pixel size ($a$) is either linked to the number of detected photons per pixel and to the precision of the sampling of the PSF profile. Larger pixels detect more photons but with less precise sampling of the PSF, whereas smaller pixels detect fewer photons but with more precise sampling of the PSF. A suitable compromise to ensure sufficient photon detection with precise sampling of the PSF is to have a pixel size of approximately 80-120 nm. Increasing the number of detected photons and minimizing the noise factors it is possible to localize a single molecule with few nanometers' accuracy. Notably, in 2005 the group of Yildiz and Selvin [43] developed a technique called Fluorescence Imaging with One Nanometer Accuracy (FIONA) based on single-molecule localization through Gaussian fitting of the PSF. They demonstrated 1.2 nm localization precision with 500 ms time resolution and applied it to unravel for the first time the walking mechanism of molecular motors myosin V [44], myosin VI [45] and kinesin [46].

Regarding single molecule localization in the three dimensions, as shown in **Figure 1.11**, there are various techniques that enable its implementation on basic Single-Molecule Localization Microscopy (SMLM) setups. Engineered PSF's methods exploit the fact that the shape of the PSF of a single molecule depends on both its lateral (x, y) and axial (z) coordinates. Consequently, by analyzing its 2D imaging pattern the axial position can be estimated too [47]. The most common approach is the *astigmatic* technique [48], [49], [50], [51] in which, by inserting a cylindrical lens into the imaging path, the shape of the PSF in the focal plane of the objective is deformed as an ellipse whose ellipticity depends on the axial position of the emitter with respect to the focal plane. Another technique is the *double helix* [52], [53], [54] in which, using phase masks or deformable mirrors, the PSF is deformed in a spiral shape with two dominant lobes whose angular orientation changes with the axial position of the emitter. Additionally, in setups with two focal planes (*biplane*) or more [55], [56], [57], 3D localization
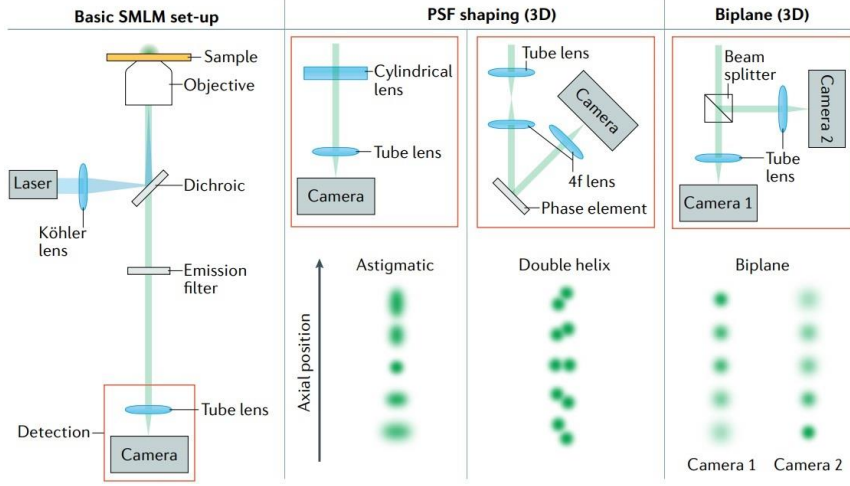
**Figure 1.11:** Three-dimensional single molecule localization microscopy techniques. Image retrieved from [47].

can be performed by analyzing the relative intensities in different images of the same molecule coming from different planes in the sample. Each of these methods require a calibration step to establish the relation between the deformation of the PSF and the axial position of the emitter. Upon calibration, it is possible to find the xyz position of the single emitter by fitting the shape of the PSF in the focal plane of the objective.

The axial uncertainty is calculated same as in (1.5) but with a different $\tau$ parameter due to axial defocus. Depending on the technique used to perform 3D imaging, the axial localization uncertainty can be estimated as [41]:

$$(\Delta z)_{as} = \frac{l^2 + d^2}{2l\sqrt{N}} \sqrt{1 + 8\tau + \sqrt{\frac{9\tau}{1 + 4\tau}}} \qquad (1.7)$$

$$(\Delta z)_{dh} = \frac{l\sqrt{\sigma_0^2(1 + l^2/d^2) + a^2/12}}{\pi h\sqrt{N}} \sqrt{1 + 8\tau + \sqrt{\frac{4\tau}{1 + 8\tau}}} \qquad (1.8)$$

$$(\Delta z)_{bp} = \frac{l^2 + d^2}{2l\sqrt{N}} \sqrt{1 + 8\tau + \sqrt{\frac{8\tau}{1 + 2\tau}}} \qquad (1.9)$$

With

$$\tau = \frac{2\pi b[\sigma_0^2(1 + l^2/d^2) + a^2/12]}{a^2 N} \qquad (1.10)$$

Where $2l$ is the axial range, $d$ the focal depth, $\sigma_0$ the in focus spot size, $h$ is the distance between the two spots and $N$, $a$, $b$ are the same parameters defined for the lateral uncertainty.

Single molecule super-resolution techniques, also called Single Molecule Localization Microscopy (SMLM), reconstruct a high-resolution image from the collection of single molecules localizations retrieved from a multiple frames acquisition. Since the positions of single fluorophores can be determined with high precision if their PSFs don't overlap, the main requirement for a SMLM acquisition is that each frame contains the detection of spatially well-separated emitters [58]. To avoid overlapping between the PSFs of individual molecules, fluorescent emissions of single molecules are separated in time. The most common approach to obtain this temporal separation exploits the property of photoswitching of some chromophores that can switch between an active 'ON' or 'bright' state, where they do emit fluorescence upon excitation, and one or more inactive 'OFF' or 'dark' states in which they do not fluoresce [47]. Different subsets of chromophores labelling the structure of interest are stochastically activated at different time points, thus being imaged without spatial overlapping and localized with high precision. By iterating the activation and imaging process the position of many fluorophores can be determined and a super-resolution image is finally reconstructed as superimposition of all the localizations (**Figure 1.12**). The resolution of the image is no more limited by diffraction but by the precision of each localization and by the number molecule simultaneously activated, which in turn depends on the photoswitching proprieties of the fluorophore. In fact, if too many molecules are activated at the same time, they overlap and it is impossible to perform single-molecule localization. Otherwise, if too few molecules activate at the
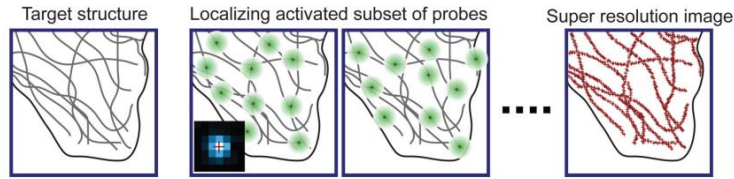
**Figure 1.12:** Imaging process of super-resolution methods based on single-molecule localization microscopy. Image retrieved from [5].

same time, the acquisition time increases as well as the probability to photobleach the sample before enough localizations have been recorded [47]. Further details on critical issues of single molecule localization are reported in section 1.3.4.

## 1.3.2 Photo-Activated Localization Microscopy (PALM)

Photo-Activated Localization Microscopy (PALM) [59] and Fluorescence PhotoActivation Localization Microscopy (fPALM) [59], [60] employ fluorophores that undergo an irreversible transition from an OFF to an ON state upon activation by a specific wavelength, typically UV light (*photoactivable fluorophores*) (**Figure 1.13**). The activation process is a one-time event, and once bleached, these fluorophores can no longer be localized. PALM, taking advantage of the versatility and specificity of genetically encoded fluorescent tags in cells, has quickly become the tool of choice for super-resolution live cell imaging. By tracking the movement of each individual protein, PALM also allows measuring local diffusion properties in living cells on short timescales [61], [62], [63] and cellular structural changes in three dimensions on longer timescales [64], [65]. Moreover, three-dimensional fPALM has been achieved using biplane detection [55] where a beam-splitter splits the fluorescence light into a shorter and longer path to form two detection planes for axial position determination. Two-colour PALM has been implemented too. For example, COS-7 cells tagged with transferrin receptor (TfR)-PAmCherry1 and PA-green fluorescent protein (PAGFP)-Clathrin light chain (CLC) were alternately imaged at 561 nm and 468 nm to excite the red (PAmCherry1) and green (PAGFP) fluorescent labels [66].
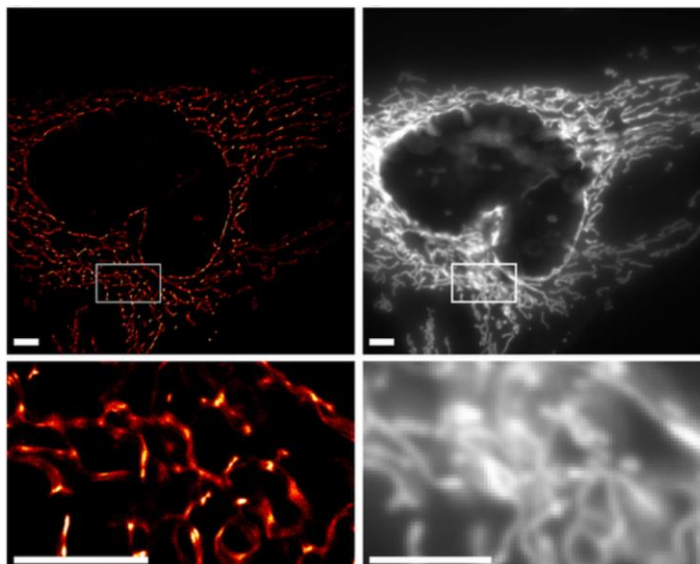
**Figure 1.13:** Distributions of mitochondria in mammalian cells by PALM and confocal. Scalebar: 4 μm. Image retrieved from [65].

## 1.3.3 Stochastic Optical Reconstruction Microscopy (STORM)

Stochastic optical reconstruction microscopy (STORM) [67] and direct STORM (dSTORM) [68] use fluorophores that can reversibly switch from an ON state to an OFF state for many cycles before being permanently turned off (*photoswitchable fluorophores*). Switching between ON and OFF states occurs upon irradiation at appropriate wavelengths and by using a specific buffer containing thiols groups to tune the photoswitching process (see complete composition of the buffer in section 1.3.4). STORM was first demonstrated by using Cy3-Cy5 pairs [67], but was quickly evolved to dSTORM by development of synthetic fluorophores that can directly be stochastically and reversibly switched in the imaging buffers [69], [70]. STORM is particularly powerful for fixed samples applications [49], [71], [72], [73], as shown in **Figure 1.14**. Moreover, three-dimensional STORM has been achieved by introducing astigmatism to the image by means of a cylindrical lens in the detection path [49]. Multicolour STORM has also been demonstrated. Microtubules were imaged alongside
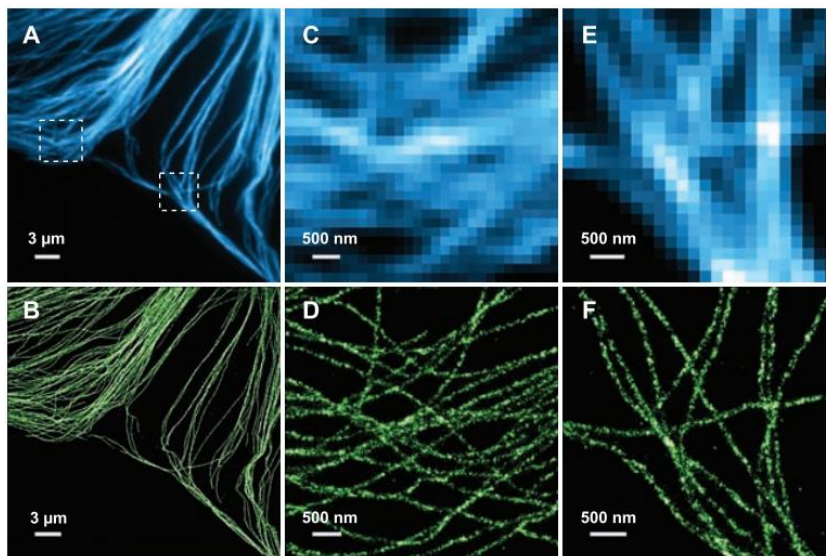
**Figure 1.14:** Two-dimensional image of microtubules in mammalian cells by immunofluorescence **(A, C, E)** and STORM **(B, D, F)**. Image retrieved from [73].

clathrin-coated pits, using Cy2-Alexa Fluor 647 and Cy3-Alexa Fluor 647 to label the microtubules and clathrin, respectively [73]. By exciting the two dye pairs selectively, it was possible to image the microtubules separately from the clathrin-coated pits with ~30-nm spatial resolution. Live-cell imaging could be performed too. For example, through multicolour STORM subcellular structures such as the membrane and mitochondria have been investigated [74], [75], [76]. However, live-cell experiments should be performed with great care due to possible issues with the use of reducing/oxidizing buffers that can affect cell integrity [77].

### 1.3.4 Critical issues of PALM/STORM imaging: choice of fluorescent probe and Nyquist criterion

Single molecule super-resolution techniques use sequential activation and localization of individual fluorophores to achieve high spatial resolution. Essential to this technique is the choice of fluorescent probes; the properties of the probes, including photons per switching event, on-off duty cycle, photostability and number of switching cycles, largely dictate the quality of super-resolution images.

Two properties of switchable probes crucial to super-resolution image quality are (i) the number of photons emitted per switching event, also called the *photon yield*, and (ii) the on-off *duty cycle*, i.e. the fraction of time that a probe spends in the fluorescent "on" state compared to the nonfluorescent "dark" state [78], [79]. Switching events with a high photon yield are desired, since the localization precision is inversely proportional to the square root of the number of detected photons [39], [44]. Hence, the photon number limits the reachable optical resolution. On the other hand, a low duty cycle is generally advantageous because the maximum number of fluorophores that can be localized in a diffraction-limited area is inversely proportional to the duty cycle. A fluorophore with a duty cycle of $1/N$ typically allows less than N molecules to be localized in a diffraction-limited area. This maximum fluorophore density in turn limits the image resolution according to the *Nyquist sampling criterion* [80]- [83], which equates the maximal achievable resolution to twice the average distance between neighboring probes. If the labelling density is insufficient, the resulting image will be undersampled and the finer details will be lost (**Figure 1.15**). Therefore, if an optical system achieves a 20 nm resolution, an equivalent image resolution can only be attained if the labeling density ensures that adjacent fluorophores are separated by 10 nm or less. This would result in extremely high molecular densities of around 10,000 molecules/$\mu m^2$, which means that, at the Nyquist molecular density, around 600 fluorophores are located within the PSF of the system (~250 nm). The presence of so many molecules within a



**Figure 1.15:** Relation between the number of localizations and the resolution. Increasing the number of localizations, increases the number of structures that can be resolved and thus the resolution of the final reconstructed image. Image retrieved from [83].
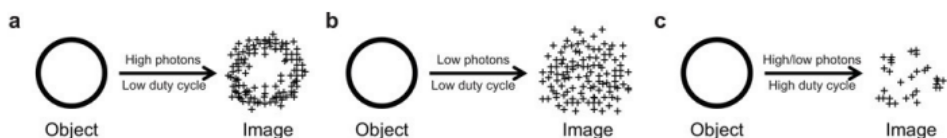
**Figure 1.16:** Effects of different photon yields and duty cycles on the quality of a PALM/STORM image. **(a)** a fluorophore with a high photon yield per switching event and a low duty cycle provides both high localization precision and high localization density, and thus can be used to resolve small structures; **(b)** a fluorophore with a low photon yield can only be localized with low precision and consequently blurs out the hollowness of the ring structure; **(c)** a fluorophore with a high on-off duty cycle limits the density of probes that can be localized in a diffraction-limited area, which also obscures the hollow ring structure owing to an insufficient number of localizations . Image retrieved from [80].

diffraction-limited space can pose significant challenges in performing accurate single-molecule localization imaging. Consequently, it is of crucial importance to finely regulate the density of actively emitting fluorophores to have a maximum of one single active emitter within a PSF area at any given time. **Figure 1.16** shows how different photon yields and duty cycles can affect the quality of a PALM/STORM image.

Moreover, two other important properties are the *survival fraction* and the *number of switching cycles*. The survival fraction corresponds to the ratio of the number of fluorophores in an ensemble still capable of switching over the number of those that are permanently photobleached after a given period of illumination (400 seconds has previously been used as a standard) [80], [84]. The survival fraction is strictly related to the number of switching cycles. Although it is desirable to have a single switching cycle for some applications, such as for counting molecules, in many cases, many switching events is advantageous. Specifically, the detection of multiple switching events from the same fluorophore reduces the stochasticity of the localization error, and in the limit of many cycles, the mean localization positions converge with the true positions of the fluorophores. This effect directly impacts the PALM/STORM image quality. In the case a dye with a low number of switching cycles is used it will result in an image with poorly defined spatial features because of higher localization errors, whereas when dye with many switching cycles is used it will

result in a smoother and more continuous image because of repetitive sampling of the same structure and thus lower noise in the final image. Also, another factor to be considered when using photoswitchable dyes is that they require the presence of a thiol and a low concentration of oxygen to maintain a long-lived "dark" state upon fluorescence emission. Usually, imaging buffers containing an oxygen scavenging system and some form of thiol, such as β-mercaptoethanol (βME) or mercaptoethylamine (MEA), are employed to lower the duty cycle of photoswitchable probes. Since each dye has different photoswitchable properties, a fine tuning of the buffer composition is required to find the one that works the best. **Table 1.1** summarize the properties of many photoswitchable dye in different imaging buffers.

| Dye | Excitation maximum (nm)[a] | Emission maximum (nm)[a] | Extinction (M⁻¹ cm⁻¹)[b] | Quantum yield[c] | Detected photons per switching event | | Equilibrium on-off duty cycle (400–600 s) | | Survival fraction after illumination for 400 s | | Number of switching cycles (mean) | |
|---|---|---|---|---|---|---|---|---|---|---|---|---|
| | | | | | MEA | βME | MEA | βME | MEA | βME | MEA | βME |
| **Blue-absorbing** | | | | | | | | | | | | |
| Atto 488 | 501 | 523 | 90,000 | 0.8 | 1,341 | 1,110 | 0.00065 | 0.0022 | 0.98 | 0.99 | 11 | 49 |
| Alexa Fluor 488 | 495 | 519 | 71,000 | 0.92 | 1,193 | 427 | 0.00055 | 0.0017 | 0.94 | 1 | 16 | 139 |
| Atto 520 | 516 | 538 | 110,000 | 0.9 | 1,231 | 868 | 0.0015 | 0.00061 | 0.92 | 0.86 | 9 | 17 |
| Fluorescein | 494 | 518 | 70,000 | 0.79 | 1,493 | 776 | 0.00032 | 0.00034 | 0.51 | 0.83 | 4 | 15 |
| FITC | 494 | 518 | 70,000 | 0.8 | 639 | 1,086 | 0.00041 | 0.00031 | 0.75 | 0.9 | 17 | 16 |
| Cy2 | 489 | 506 | 150,000 | 0.12 | 6,241 | 4,583 | 0.00012 | 0.00045 | 0.12 | 0.19 | 0.4 | 0.7 |
| **Yellow-absorbing** | | | | | | | | | | | | |
| Cy3B | 559 | 570 | 130,000 | 0.67 | 1,365 | 2,057 | 0.0003 | 0.0004 | 1 | 0.89 | 8 | 5 |
| Alexa Fluor 568 | 578 | 603 | 91,300 | 0.69 | 2,826 | 1,686 | 0.00058 | 0.0027 | 0.58 | 0.99 | 7 | 52 |
| TAMRA | 546 | 575 | 90,430 | 0.2 | 4,884 | 2,025 | 0.0017 | 0.0049 | 0.85 | 0.99 | 10 | 59 |
| Cy3 | 550 | 570 | 150,000 | 0.15 | 11,022 | 8,158 | 0.0001 | 0.0003 | 0.17 | 0.55 | 0.5 | 1.6 |
| Cy3.5 | 581 | 596 | 150,000 | 0.15 | 4,968 | 8,028 | 0.0017 | 0.0005 | 0.89 | 0.61 | 5.7 | 3.3 |
| Atto 565 | 563 | 592 | 120,000 | 0.9 | 19,714 | 13,294 | 0.00058 | 0.00037 | 0.17 | 0.26 | 4 | 5 |
| **Red-absorbing** | | | | | | | | | | | | |
| Alexa Fluor 647 | 650 | 665 | 239,000 | 0.33 | 3,823 | 5,202 | 0.0005 | 0.0012 | 0.83 | 0.73 | 14 | 26 |
| Cy5 | 649 | 670 | 250,000 | 0.28 | 4,254 | 5,873 | 0.0004 | 0.0007 | 0.75 | 0.83 | 10 | 17 |
| Atto 647 | 645 | 669 | 120,000 | 0.2 | 1,526 | 944 | 0.0021 | 0.0016 | 0.46 | 0.84 | 10 | 24 |
| Atto 647N | 644 | 669 | 150,000 | 0.65 | 3,254 | 4,433 | 0.0012 | 0.0035 | 0.24 | 0.65 | 9 | 39 |
| Dyomics 654 | 654 | 675 | 220,000 | – | 3,653 | 3,014 | 0.0011 | 0.0018 | 0.79 | 0.64 | 20 | 19 |
| Atto 655 | 663 | 684 | 125,000 | 0.3 | 1,105 | 657 | 0.0006 | 0.0011 | 0.65 | 0.78 | 17 | 22 |
| Atto 680 | 680 | 700 | 125,000 | 0.3 | 1,656 | 987 | 0.0019 | 0.0024 | 0.65 | 0.91 | 8 | 27 |
| Cy5.5 | 675 | 694 | 250,000 | 0.28 | 5,831 | 6,337 | 0.0069 | 0.0073 | 0.87 | 0.85 | 16 | 25 |
| **NIR-absorbing** | | | | | | | | | | | | |
| DyLight 750 | 752 | 778 | 220,000 | – | 712 | 749 | 0.0006 | 0.0002 | 0.55 | 0.58 | 5 | 6 |
| Cy7 | 747 | 776 | 200,000 | 0.28 | 852 | 997 | 0.0003 | 0.0004 | 0.48 | 0.49 | 5 | 2.6 |
| Alexa Fluor 750 | 749 | 775 | 240,000 | 0.12 | 437 | 703 | 0.00006 | 0.0001 | 0.36 | 0.68 | 1.5 | 6 |
| Atto 740 | 740 | 764 | 120,000 | 0.1 | 779 | 463 | 0.00047 | 0.0014 | 0.31 | 0.96 | 3 | 14 |
| Alexa Fluor 790 | 785 | 810 | 260,000 | – | 591 | 740 | 0.00049 | 0.0014 | 0.54 | 0.62 | 5 | 2.7 |
| IRDye 800 CW | 778 | 794 | 240,000 | – | 2,753 | 2,540 | 0.0018 | 0.038 | 0.6 | 1 | 3 | 127 |

**Table 1.1**: Summary of photoswitching properties of different dyes in presence of a glucose oxidase-based oxygen scavenging buffer (GLOX) and 10 mM MEA as well as GLOX and 140 mM βME. *Excitation and emission maximum* are the peak wavelength from the dye spectra; the *molar extinction coefficient* measures how strongly the fluorophore absorbs light at a specific wavelength; the *quantum yield* measures the efficiency of the fluorescence emission and is defined as the ratio of the number of emitted photons to the number of absorbed photons. Image retrieved from [80].

Finally, in addition to the photoswitchable properties of the selected dye and the composition of the imaging buffer, another crucial factor to consider when performing single molecule imaging is the phenomenon of photobleaching. During prolonged imaging, photoswitchable probes gradually undergo irreversible transformation into a non-fluorescent state, in a process known as *photobleaching*. This results in lowering the probe molecular density over time, which in turn decreases the information content in the individual frames and increases the number of frames required to reconstruct the super-resolution image. To ensure an ideal number of emitting fluorophores per frame, the duty cycle of the probes needs to increase over time. For many molecules, this can be achieved by irradiating the sample with an "activation" laser at a shorter wavelength than the excitation laser, typically in the violet or ultraviolet range [77], [85], [86]. This approach effectively accelerates the transition of molecules from the long-lived "dark" state back to the fluorescent ground state. **Table 1.2** shows the different responses of various dyes to violet photoactivation.

| Dye | | Sensitivity[a] |
|---|---|---|
| Blue-absorbing | Atto 488 | + |
| | Alexa Fluor 488 | + |
| | Atto 520 | + |
| | Fluorescein | – |
| | FITC | – |
| | Cy2 | – |
| Yellow-absorbing | Cy3B | + |
| | Alexa Fluor 568 | + |
| | TAMRA | – |
| | Cy3 | – |
| | Cy3.5 | + |
| | Atto 565 | + |
| Red-absorbing | Alexa Fluor 647 | ++ |
| | Cy5 | ++ |
| | Atto 647 | + |
| | Atto 647N | + |
| | Dyomics 654 | ++ |
| | Atto 655 | + |
| | Atto 680 | + |
| | Cy5.5 | ++ |
| NIR-absorbing | Dylight 750 | ++ |
| | Cy7 | ++ |
| | Alexa Fluor 750 | ++ |
| | Atto 740 | + |
| | Alexa Fluor 790 | ++ |
| | IRDye 800CW | ++ |

**Table 1.2:** Sensitivity to violet-light photoactivation of different dyes. Fluorescent molecules were activated with a 0.25 s ultraviolet (405 nm) pulse. A different sign was assigned to each dye based on the percentage of reactivated molecules: "-" if "<3%", "+" if "3-25%" or "++" if ">25%". Image retrieved from [80].

To summarize, PALM/STORM imaging allows achieving resolutions one order of magnitude higher than conventional fluorescence microscopy. The selection of fluorophore is crucial, but alone, it does not guarantee such resolution. Equally important are the composition of the imaging buffer and the acquisition parameters. Only by carefully considering all these factors it is possible to achieve resolutions on the order of tens of nanometers.

## 1.4  Super-resolution by minimal photon fluxes (MINFLUX)

MINimal emission FLUXes (MINFLUX) is a novel super-resolution technique developed by Balzarotti et al. in 2017 [87] that uses the best of STED microscopy and single molecule localization imaging. As in PALM/STORM imaging, emitters are activated separately so that their images don't overlap and they can be resolved, while the localization is performed with a structured doughnut-shaped beam with zero central intensity. The nearer this zero is to the fluorophore, the weaker the fluorescence emission will be and fluorescence will stop when the position of the zero corresponds with the one of the fluorophore. Hence, in MINFLUX the emitter position is not determined by the presence of fluorescence, but by its absence. MINFLUX achieves nanometers accuracy with a relatively small number of photons, compared to centroid-based localization techniques. This enhanced precision is attained by directing the excitation doughnut's zero to the molecule's position, thus effectively reducing the required number of detected photons for localization. Since the location of the doughnut zero is well known, the remaining fluorescence provides information about the residual distance between the molecule and the zero. As a result, aside from confirming the molecule's presence, the emitted fluorescence contains information about the molecule's position [87]. Fluorescence can be seen as the result of the mismatch between the molecular location and

the zero's position: the tinier is the mismatch, the fewer are the fluorescence photons required for localization. For this reason, in MINFLUX the molecule's position is investigated through scans of the driving beam around the predetermined location of the fluorophore [88], [89]. Then, the number of observed photons is used to determine the location of the molecule. Specifically, since photon emission is a Poissonian process, the acquired photon counts obey to Poissonian statistics and thus the position of the emitter can be estimated performing a maximum likelihood estimation. Unlike camera-based localization techniques, in which the precision is homogeneous throughout the field of view, CRLB in MINFLUX reaches a minimal value of:

$$\sigma_{CRLB}(0) = \frac{L}{4\sqrt{N}} \qquad (1.11)$$

at the center of the probing range, where $L$ is the diameter of the doughnut beam and $N$ the total number of detected photons. It should be noted that two measurements with the zero targeted to coordinates within a distance L = 50 nm localize a molecule with ≤2 nm precision using merely 100 detected photons. Compared with centroid-based localization, MINFLUX attains nanoscale precision with a much smaller number of detected photons and record trajectories with a much higher temporal resolution [87].

**Figure 1.17** shows the principle of 2D MINFLUX. Excitation is performed with a laser beam with zero central intensity. Then, using the predicted zero-intensity position, the well-defined excitation beam shape, and the quantity of photons emitted by the fluorescent molecule at various positions within the excitation beam, through several iterations, the precise localization of the fluorescent molecule can be determined. In each iteration, the doughnut-shaped excitation beam is centered on the localization of the latest fluorophore. The diameter ($L$) of the doughnut's movement is gradually decreased to enhance resolution. Throughout the entire iteration process, the
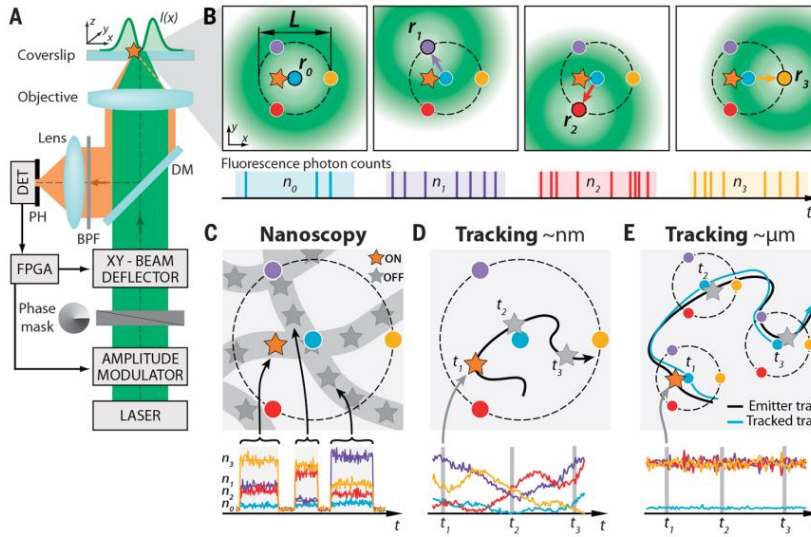
**Figure 1.17:** 2D MINFLUX concept and applications. **(A, B)** Simplified version of a setup. An excitation laser beam (green) is shaped by a vortex-phase mask forming a doughnut intensity spot in the focal plane of the objective lens. The intensity of the beam is modulated and deflected such that its central zero is sequentially placed at the four focal plane positions $\vec{r}_{0,1,2,3}$ indicated by blue, violet, red, and yellow dots, respectively. Photons emitted by the fluorescent molecule (star) are collected by the objective lens and directed toward a fluorescence bandpass filter (BPF) and a confocal pinhole (PH), by using a dichroic mirror (DM). The fluorescence photons $n_{0,1,2,3}$ counted for each doughnut position $\vec{r}_{0,1,2,3}$ by the detector (DET) are used to extract the molecular location. Intensity modulation and deflection, as well as the photon counting, are controlled by a field-programmable gate array (FPGA). Diagrams of the positions of the doughnut in the focal plane and resulting fluorescence photon counts. **(C, D, E)** Basic applications: fluorescence nanoscopy, short-range tracking, long-range tracking. Image and caption retrieved from [87].

location information of each detected fluorescence molecule will be accumulated into the information for the next detection. In contrast, conventional super-resolution methods always detect all photons in the same way, yielding the same limited information as the first photon. Compared with single-molecule localization microscopy (SMLM), MINFLUX can use less than 1,000 photons and a lower laser intensity to achieve localization accuracy at the molecular scale. MINFLUX localization doesn't require to wait for a huge number of fluorescence photons and it maximizes the informational value of each emitted photon. Because MINFLUX localization is no longer constrained by the need for a large quantity of fluorescence photons, it achieves a temporal resolution one order of magnitude higher than PALM/STORM imaging [90].
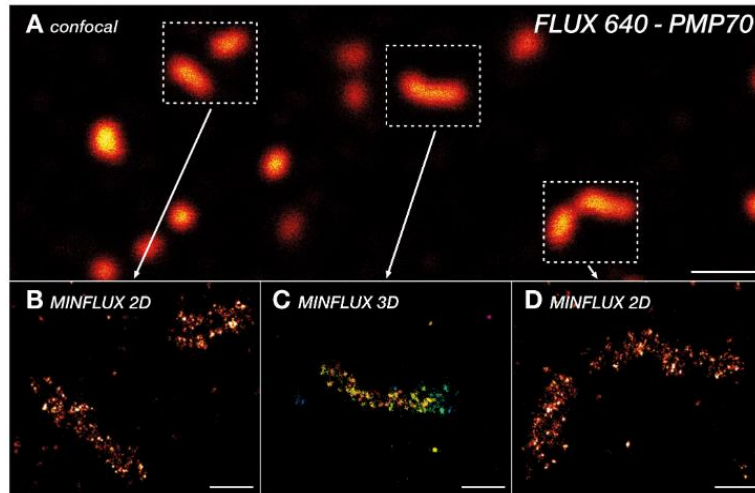
**Figure 1.18:** Multiple recordings of peroxisomal membrane protein PMP70 labeled with FLUX 640 in one area by confocal **(a)**, 2D MINFLUX **(B, D)** and 3D MINFLUX **(C).** Image retrieved from [95] .

Thus far, MINFLUX imaging has been performed on nuclear pore complexes (NPCs) [87], mitochondrial contact site and cristae organizing system (MICOS) proteins in mitochondria [91], axonal bII spectrin in primary hippocampal neurons [92], and several kinds of presynaptic Active Zone [93]. Moreover, 3D simultaneous multicolour MINFLUX have been performed in both fixed and living cells with few nm accuracy in the three dimensions (see **Figure 1.18**) [94], [95], [96].

Although MINFLUX is a novel approach that achieves the highest resolution among the super-resolution techniques its capabilities have several limitations. As in PALM/STORM imaging the choice of the fluorophore is crucial to have a high-resolution image – best ones are those with high contrast ratio and low duty cycle [95] – and post-processing image is required to get the final image. Moreover, currently the maximum size of field of view (FOV) that can be imaged is quite small ($10 \times 10 \ \mu m^2$) [94] and 3D imaging can be performed only within thin samples (<500 nm) [93]. Also, although MINFLUX achieves high temporal resolutions ($\sim$ few ms), since it's a scanning technique, the recording time for the whole FOV is longer and is around tens of minutes (60 minutes for $10 \times 10 \ \mu m^2$) [94]. Finally, as
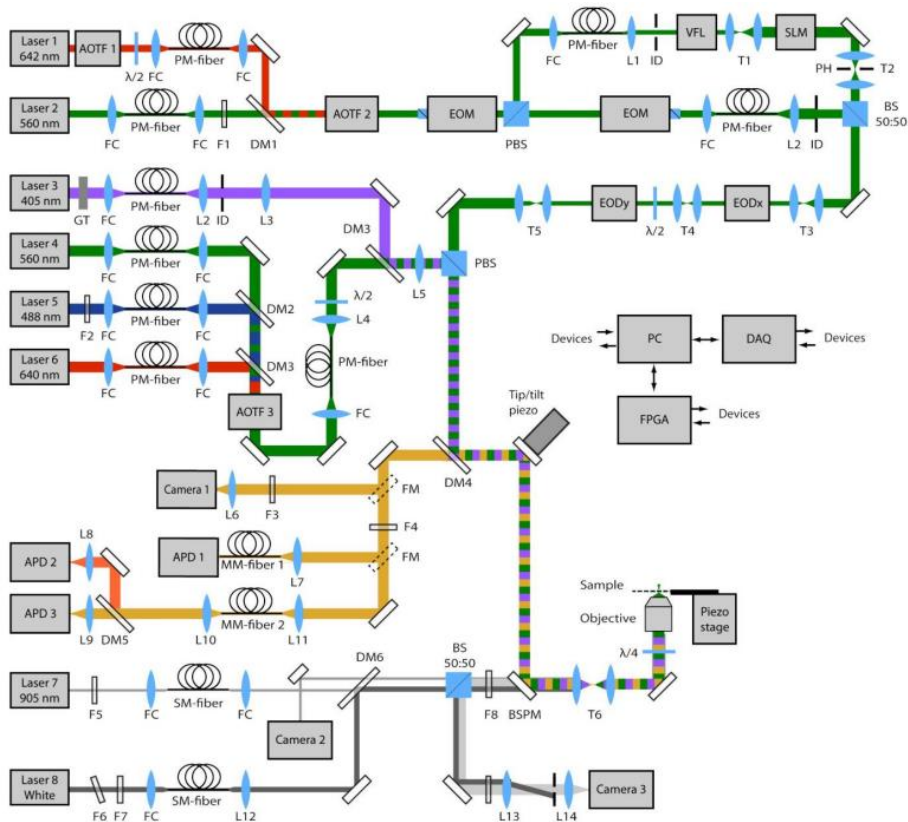
**Figure 1.19:** Schematic drawing of an optical setup used to perform 3D multicolour MINFLUX. Image retrieved from [94].

shown in **Figure 1.19**, the development of setup is quite complex and expensive compared to the other super-resolution techniques.

## 1.5 Comparison between super-resolution techniques

Over the last two decades many super-resolution techniques have been developed to overcome the diffraction limit and provide new insights into subcellular organization. Among the methods discussed in the previous sections, each approach has its own advantages and drawbacks:

- SIM can be used with any fluorophore and is relatively rapid, making it useful for multicolour and live-cell imaging studies, but its resolution is only two times better than conventional fluorescence microscopy. Furthermore, SIM can be difficult to

perform successfully with samples that have fluorophores above and below the plane of focus so it can only image thin samples (~ μm). Moreover, since multiple frames are acquired for each field of view, post-processing image is required. This increases the possibility of introducing artefacts due to the reconstruction algorithms.

- STED is a variant of confocal microscopy and it is therefore subject to some of the benefits and limitations of that technique. STED provides intermediate resolution gains between that of SMLM and SIM and, as confocal microscopy, can be employed for optical sectioning of biological structure and thus image thick samples (~ 20 μm). Also, STED is relatively rapid as only a single image is acquired and no reconstruction is required. However, since it's not compatible with all fluorophores, multicolour imaging can be challenging. Moreover, as the high intensity of the STED beam can cause photobleaching and phototoxicity live-cell imaging can be difficult too.

- SMLM techniques achieve tens of nanometers resolution in the three-dimensions. As widefield microscopies they're compatible with multiple illumination techniques and thus signal to noise ratio (S/N) can be increased with TIRF or HILO illumination (better explained in section 6.3). Moreover, thanks to the availability of many different photoswitchable fluorophores both multicolour and live-cell imaging can be performed. However, although 3D imaging can be easily implemented, it is limited to only few microns in depth. Also, contrary to SIM and STED, the acquisitions are slow because two molecules cannot be turned on within the same PSF at any given time and because to localize a single molecule with nanometer accuracy a high number of photons must be detected. Furthermore, as in SIM, post-processing image is required, thus creating a concern for potential artefacts that cannot easily be discerned.

- MINFLUX has the best spatial and temporal resolution. It can localize single molecules with few nm accuracy in the three dimensions in few ms. Moreover, multicolour and live-cell imaging can be performed too. However, for now MINFLUX imaging can be performed only in small fields of view (< 10x10 µm$^2$), thin samples (<500 nm) and, as for SMLM, the acquisition is slow and image post-processing is required.

**Table 1.3** summarizes the benefits and limitations of different methods.

| Method | STED | SIM | SMLM | MINFLUX |
|---|---|---|---|---|
| Illumination | Laser scanning | Widefield | Widefield | Laser scanning |
| Number of required excitation light wavelengths | 2 | 1 | 1-2 | 1-2 |
| Spatial Resolution<br>Lateral<br>Axial | 20-70 nm<br>40-150 nm | 100-130 nm<br>160-300 nm | 10-30 nm<br>10-75 nm | 2-3 nm<br>3-5 nm |
| Z-stack range | ~ 20 µm | Few µm | 1-2 µm | 500 nm |
| Data size per 1 image | 1 frame | 9-15 frames | $10^3$ - $10^4$ frames | ~500 frames |
| Acquisition speed per 1 image | Fast (ms-s) | Fast (ms-s) | Slow (minutes - tens of minutes) | Slow (~ tens of minutes) |
| Image post-processing | No | Yes (Fourier Transform) | Yes (centroid identification) | Yes (centroid identification) |
| Probes | Any if photostable | Any | Photoswitchable fluorophores | Photoswitchable fluorophores |
| Photodamage | Moderate-High | Moderate | Low-Moderate | Low |
| Photobleaching | Moderate-High | Moderate-High | Low | Low |
| Multicolour imaging | Yes, but limited multicolour choice | Yes | Yes | Yes |
| Live-cell imaging | Yes, but difficult | Yes | Yes | Yes |

**Table 1.3:** Summary of main benefits and limitations of different super-resolution techniques.

Overall, up to date, there isn't a super-resolution technique that can be universally considered "the best". The choice of which super-resolution technique to use depends on the specific biological question, the type of sample being studied, and various practical considerations. Each super-resolution technique has its advantages and limitations, making them more suitable for certain applications than others. The choice often comes down to a trade-off between resolution, speed, ease of use, and the compatibility of the technique with the sample and the experimental requirements.

To study the organization and dynamics of single molecules in the subcellular environment the most suitable technique should be able to perform three-dimensional multicolour imaging with nanometer resolution. Both MINFLUX and SMLM partially meet these requirements. MINFLUX has the highest spatial and temporal resolution, but it's limited to small fields of view and thin samples. On the other hand, SMLM can image bigger volumes, but its resolution is one order of magnitude worse than MINFLUX. During my PhD I developed a super-resolution setup based on SMLM that, thanks to a fine correction of aberrations and mechanical/thermal drifts, performs 3D multicolour imaging with nanometers resolution in volumes 16 times bigger than MINFLUX's paving the way for the study of many more biological structures.

# Chapter 2

# Development of an optical system for three-dimensional multicolour super-resolution microscopy

Single-molecule super-resolution microscopy techniques have become increasingly relevant in biology over the past few decades. Since their first introduction at the beginning of 21st century, SMLM techniques have been rapidly developing and thanks, to their technical capabilities and wide range of applications. However, there is still much room for improvement. Currently, performing multicolour super-resolution imaging is not trivial. In fact, despite the availability of several commercial setups for multicolour super-resolution microscopy, achieving reliable results requires fine correction of all potential aberrations and artifacts that could significantly impact the outcomes. Performing multicolour super-resolution imaging is even more challenging in small volume samples, such as bacteria, because it requires a correction of all the aberrations and artifacts at the nanoscale level.

In this chapter I will describe the SMLM set-up I developed and I will demonstrate that, through a nanometer stabilization of the microscope and a fine correction of optical aberrations, it is feasible to perform three-dimensional multicolour super-resolution imaging with nanometer accuracy. I will begin by introducing different approaches to perform multicolour imaging, then I will examine technical difficulties that limit the spatial resolution in single-molecule

multicolour imaging and, finally, I will illustrate the methods we developed to overcome these limitations and reach nanometer accuracy.

## 2.1   Multicolour approaches

Multicolour imaging is an essential tool in biophysics to better characterize and understand biological processes, but it demands careful planning and consideration of fluorophore characteristics and choice of the imaging approach. To achieve accurate and reliable multicolour imaging, several critical considerations must be taken into account. When choosing fluorophores, it's crucial to ensure that their excitation and emission spectra are compatible with the characteristics of the imaging system's light source and filter sets, but also that they're spectrally separated to avoid signal crosstalk (see section 2.2.2). This choice becomes even more complex when performing multicolour SMLM, because fluorophores must be, not only spectrally separated, but also have similar photoswitching properties. Failure to meet these requirements can lead to issues in the PALM/STORM imaging process. Another important choice concerns the imaging approach, whether sequential or simultaneous, because each approach corresponds to a different optical system configuration and has its own set of advantages and limitations.

### 2.1.1  Sequential imaging

One approach to perform multicolour super-resolution microscopy is through sequential imaging. Sequential imaging involves the consecutive excitation and detection of individual fluorophores, as illustrated in **Figure 2.1**. To explain this concept, let's consider the scenario where we have two fluorophores with well-separated excitation and emission spectra. For example, one fluorophore ($F_1$) is excited in the blue part of the visible spectrum and emits in the green, while another fluorophore ($F_2$) is excited in the green and emits in the

red. Sequential acquisition process consists of many cycles in which the fluorophores are excited and detected consecutively. In each cycle, first, we activate the excitation laser for one fluorophore (for example, the blue one if we want to excite $F_1$). This laser excites the fluorophore, which starts to emit fluorescence and its emission signal is detected. After recording a certain number of frames, we turn off the laser for this fluorophore and then we turn on the laser for the other fluorophore (in this case the green one for $F_2$). Just as before, the laser excites the fluorophore, leading to fluorescence emission, which is recorded for the same number of frames as in the previous step.

This sequential imaging process, involving the sequential activation and deactivation of lasers for each target fluorophore, is repeated until
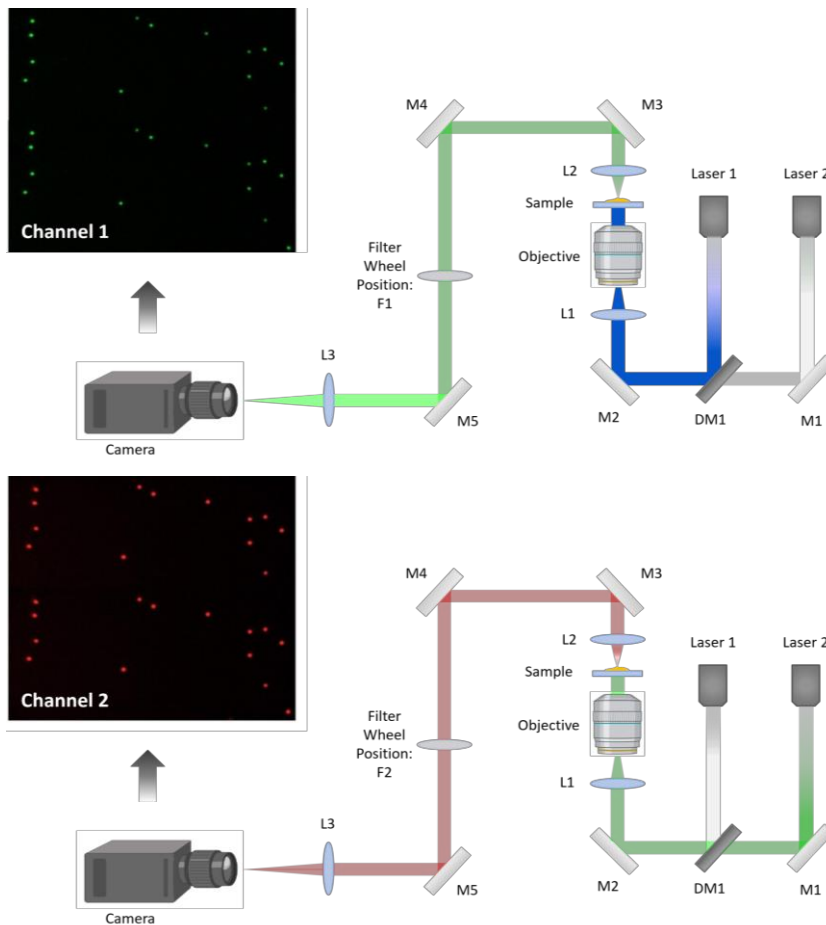
**Figure 2.1:** Scheme of an optical system for sequential super-resolution multicolour imaging.

enough localizations of the region of interest are recorded. These localizations are then used to construct the multicolour image.

### 2.1.2 Simultaneous imaging

Another approach to perform multicolour super-resolution microscopy is through simultaneous imaging, where multiple fluorophores are excited and detected at the same time, as illustrated in **Figure 2.2**. Let's consider the same fluorophores mentioned in the previous section. The simultaneous acquisition process is more straightforward compared to the alternating method and involves only two steps: i) dual view system alignment check and ii) imaging of the fluorophores. In simultaneous imaging, both fluorophores are detected at the same time, but the fluorophore emitted is splitted on the two halves of the camera (**Figure 2.2**). Therefore, it's crucial to ensure that the detection path is correctly aligned so that the same field of view is visible in both halves of the camera. Even minor optical drifts can result in significant shifts in the final image, potentially compromising the experiment. Once the alignment is carefully checked, the acquisition starts. Both excitation lasers are switched on simultaneously, causing both fluorophores to emit fluorescence. Two
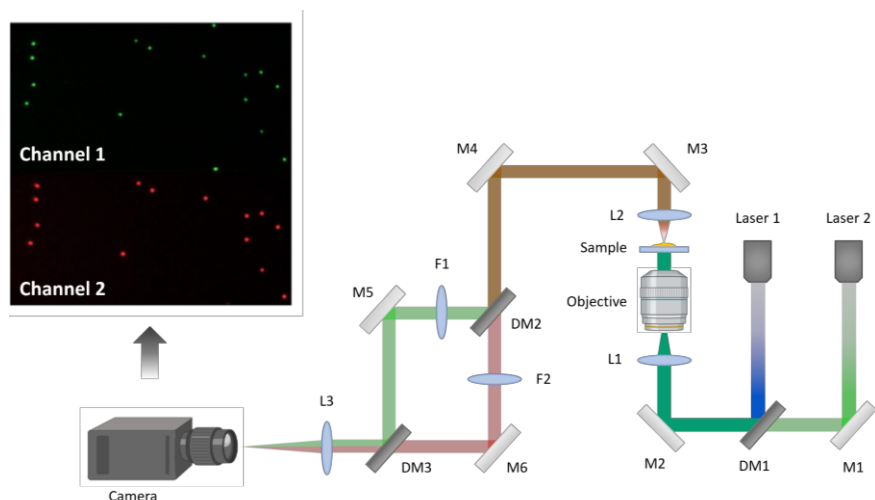
**Figure 2.2:** Scheme of an optical system for simultaneous super-resolution multicolour imaging.

dichroic mirrors (DM2 and DM3) and two short band pass fluorescence filters (F1 and F2) in the detection path are used to separate the emissions from the two fluorophores and direct them towards the corresponding half of the camera (**Figure 2.2**). The emission of each fluorophore is recorded in only one half of the camera.

Simultaneous imaging simplifies the process by allowing the concurrent detection of two fluorophores, making it a valuable approach in multicolour super-resolution microscopy. However, precise alignment is crucial to ensure accurate results.

### 2.1.3  Benefits and limitations of each configuration

Sequential acquisition offers the advantage of a larger field of view, thus enabling the imaging of bigger samples. Additionally, by carefully selecting spectrally separated fluorophores and employing short band fluorescence filters, it is possible to effectively eliminate crosstalk between the fluorophores. Moreover, because fluorophores are activated sequentially, it allows for the use of the most suitable acquisition parameters for each fluorophore, thus optimizing the data quality. However, it's important to note that the sequential activation of fluorophores comes with some trade-offs. The main drawbacks include longer acquisition times and a potential loss of localizations. Even though both fluorophores are activated simultaneously, they are detected one by one, which can result in a slower data acquisition process compared to simultaneous imaging methods. Additionally, some localizations may be lost due to the sequential nature of the acquisition, especially when using photoactivatable fluorophores photoconverted from the same wavelength. This is because, simultaneous activation of both fluorophores, recording one results in the loss of localizations from the other.

Simultaneous acquisition offers the advantage of being faster and avoids the loss of localizations, making it particularly suitable for live imaging compared to sequential imaging methods. However, there are some trade-offs too. Since both fluorophores are excited and detected at the same time, there is a higher probability of crosstalk between them, even when using spectrally separated fluorophores and short band pass filters. Some signal crossover may occur, which can affect data accuracy. Additionally, in setups with only one camera, simultaneous imaging typically results in a smaller field of view compared to sequential methods. This limitation may impact the ability to capture larger sample areas in a single frame. Moreover, in simultaneous imaging certain acquisition parameters, such as exposure time, camera gain, and laser activation power, must be the same for both fluorophores[1]. These parameters are closely related to the photoswitching properties of the fluorophores. Consequently, careful selection of fluorophores with similar photoswitching properties is essential to ensure reliable and accurate imaging. If the photoswitching properties of the chosen fluorophores are significantly different, the imaging process may not work effectively, then leading to unreliable results.

Sequential and simultaneous imaging approaches in super-resolution microscopy both offer unique advantages and come with their specific limitations. Just like in the choice of super-resolution methods, there is no one-size-fits-all approach when it comes to selecting between these imaging methods. The suitability of one over the other often depends on the specific requirements and objectives of the experiment. The better approach is typically the one that aligns most closely with the needs of the experiment. The selection depends on

---

[1] Setups with two cameras allow for different exposure time and camera gain even during sequential imaging. However, if the fluorophores are photoconverted by the same wavelength, the power and duration of the activation laser will be the same and thus they will require careful selection to get reliable imaging.

factors such as the sample size, the presence of crosstalk, the availability of suitable fluorophores with compatible photoswitching properties, the desired imaging speed, and the technical capabilities of their equipment. Ultimately, the choice between sequential and simultaneous imaging should be made thoughtfully to ensure that the selected method aligns with the research goals. Since we wanted to develop a system to perform 3D multicolour super-resolution of both fixed and living cells, we opted for the simultaneous imaging approach because it fitted better our needs. Implementation and alignment of the Dual View are reported in section 6.1.

## 2.2 Limiting factors of single-molecule multicolour imaging

In 2005 Yildiz et al. [43] demonstrated that, by increasing the number of detected photons and minimizing the background noise, it is possible to localize a single molecule with one nanometer accuracy. Through the years many microscopic techniques based on single-molecule localization have been developed, but none of them got to reach that accuracy. Although SMLM can theoretically achieve a resolution equal to the size of a single fluorophore, in practice their resolution is one order of magnitude worse than the expected. The loss of resolution is mainly caused by mechanical and thermal drifts that affect both sample and instrumentation causing artifacts in the reconstructed image. Moreover, multicolour imaging also suffers from crosstalk and chromatic aberrations that can give false negatives or positives, thus making the experimental results less reliable.

### 2.2.1 Mechanical and thermal drifts

As we have seen in the previous chapter, localization based super-resolution technique, as PALM and STORM, create a super-resolution image as superimposition of the subpixel localizations of single fluorophores. The higher is the number of localized molecules, the

better will be the resolution of the final image. However, since only few fluorophores per field of view must be activated at the same time to be resolved, each acquisition lasts thousands of frames. These experiments require nanometer or subnanometer stability to work properly. However, long time measurements can be affected by sample or instrument drift due to temperature variations or mechanical relaxation effects. Drift can extend to several hundred nanometers within just a few minutes. While this is already problematic in conventional imaging, it becomes unacceptable for super-resolution imaging where even minimal drift, as low as 10 nm, can significantly distort the images. Neglecting small drifts can lead to blurring in the reconstructed image or the generation of artifacts, such as shadowed microtubules [50] (**Figure 2.3** left). Lateral drift can be quantified by monitoring fiducial markers, such as fluorescent beads or gold particles and by subtracting the estimated drift. (**Figure 2.3** right) in post processing. Alternatively, lateral drifts can be assessed using speckle patterns formed by backscattered light [97]. For highly redundant structures like microtubules, drift estimation can be derived directly from single-molecule localizations through image cross-correlation [98], [99]. Although there are many techniques to efficiently correct for lateral drift, they're not as good with axial drift. Axial drift is worse than lateral one because it deteriorates 2D SMLM
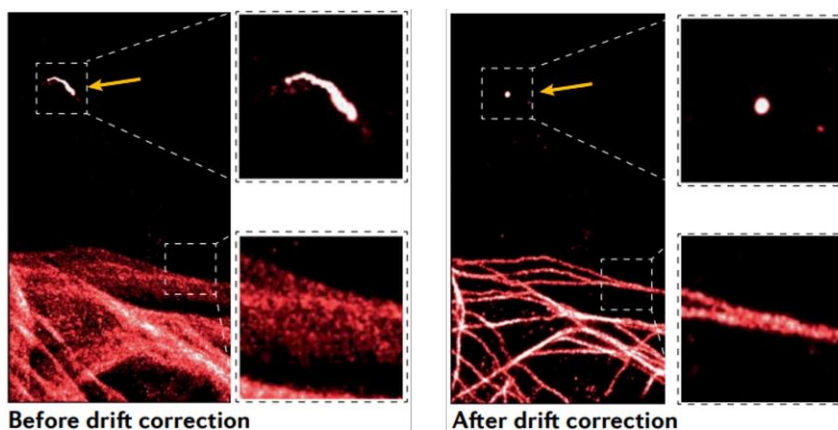


**Figure 2.3:** 2D SMLM image of microtubules before and after drift correction. Arrows show a fluorescent bead used to estimate and correct the drift. Image retrieved from [47].

images. As we said in the previous chapter, the resolution of a PALM/STORM image is strictly related to the precision of each localization. Lateral drifts cause the translation of the field of view within the xy plane. However, since the focusing plane remains unchanged, the single molecules can still be localized with high precision and, through post processing algorithms, such as cross-correlation, lateral drifts can be corrected. In contrast, axial drifts shift the field of view in the z-direction, thus altering the focusing plane and leading to less precise localization of single molecules. Axial drifts post-processing algorithms [51], [97], [100] are less effective than their lateral drift counterparts due to the reduced precision in localizing single emitters.

Additionally, high-frequency vibrations can also impact localization precision by causing blurring at the individual level. Similar to axial drift, these vibrations cannot be corrected through computational methods. Hence, it is crucial to isolate the microscope from vibration sources.

The most effective strategy for minimizing residual vibrations and drift artifacts is to use a real-time adjustment of the stage position [99], [101], [102]. While technically more demanding than computational drift correction, these methods can reduce the drifts to just a few nanometers or less [103], [104], [105], [106].

## 2.2.2 Optical crosstalk

Optical crosstalk, also known as bleed-through or crossover, is a phenomenon observed in multi-channel microscopy where the signal from one fluorescent dye is detected as if it were coming from another dye. In other words, the signal appears to originate from one dye, but it arises from a different one [107]. This happens when the excitation and emission spectra of two or more fluorescent dyes partially overlap. Therefore, the signal is contaminated and it makes experimental results less reliable since it can give false negatives or
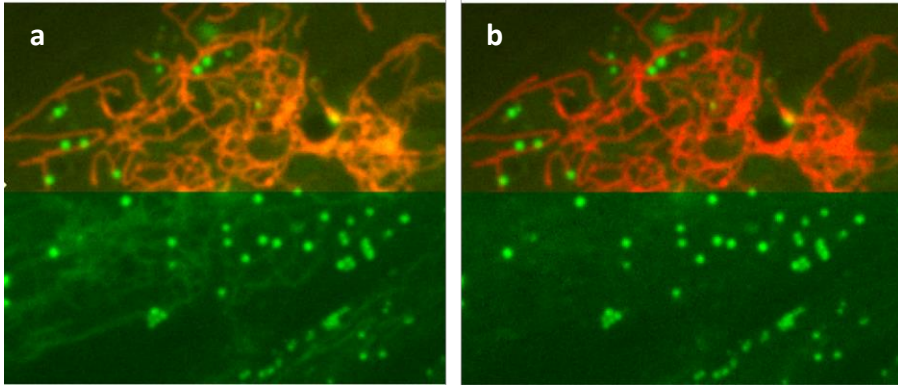
**Figure 2.4:** Two-colour image of mitochondrial (red) and lipid droplets (green) with **(a)** and without crosstalk **(b)**. Image retrieved from [107].

positives (see **Figure 2.4**). Crosstalk becomes problematic when conducting multi-channel analyses, such as colocalization or object-based analysis. To prevent this problem in multicolour imaging, it's advisable to select dyes with substantial separation between their excitation and emission spectra. When using dyes that may potentially overlap, incorporating multiple controls (such as negative controls and single-dye controls) can help in compensating for the issue during data analysis. Another approach to compensation involves using narrower bandpass filters, which can help purify the signals but may reduce the overall signal intensity.

By carefully choosing dyes, optimizing the instrumentation, and implementing experimental controls, it's possible to minimize the impact of fluorescence crosstalk.

### 2.2.3  Chromatic aberrations

In optics, chromatic aberration (CA), also known as chromatic distortion, refers to the inability of a lens to focus all colours to the same point [108]. This occurs due to a phenomenon called dispersion, where the refractive index of the lens elements changes with the wavelength of light. In most transparent materials, the refractive index decreases as the wavelength of light increases [109]. Since the focal length of a lens depends on the refractive index, this variation in
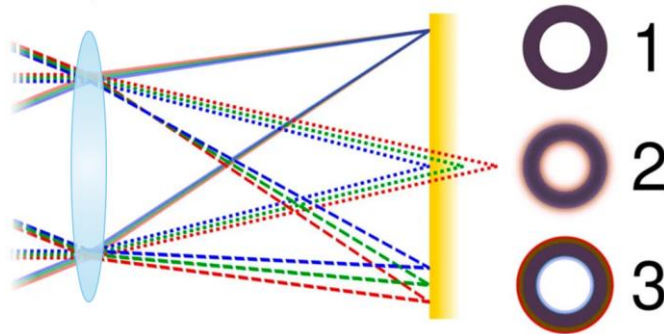
**Figure 2.5:** Comparison of an ideal image of a ring (1) and ones with only axial (2) and only transverse (3) chromatic aberration.

refractive index can impact the focusing process [110]. Chromatic aberrations become noticeable as "fringes" of colour along the boundaries that separate dark and bright regions within the image. There are two types of chromatic aberration: lateral (transverse) and axial (longitudinal) as shown in **Figure 2.5**. Lateral aberration occurs when different wavelengths are focused at different positions in the focal plane, because the magnification and/or distortion of the lens also varies with wavelength. Lateral aberration is typical at short focal length and increases going from the center of the image towards the edges. Axial aberration occurs when different wavelengths of light are focused on different distances from the lens (focus shift). Longitudinal aberration is typical at long focal lengths and occurs throughout the image [109].

Chromatic aberrations can be reduced by employing achromatic lenses, which are constructed by combining materials with different dispersive properties to create a compound lens. The most used type is the achromatic doublet, consisting of elements made of crown and flint glass (see **Figure 2.6b**). This approach reduces the level of chromatic aberration over a specific range of wavelengths, although it does not achieve complete correction. Another method for minimizing chromatic aberrations involves utilizing diffractive optical elements with negative dispersion, which complements the positive Abbe numbers of optical glasses and plastics (see **Figure 2.6c**).
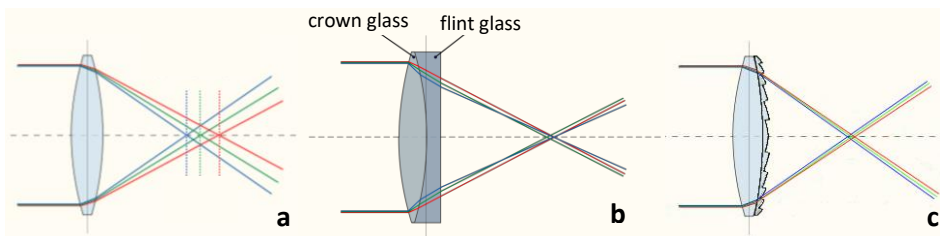
**Figure 2.6: (a)** Chromatic aberration of a single lens caused different wavelengths to have a different focus point; **(b)** achromatic doublet minimize chromatic aberration so that visible wavelengths have approximately the same focal length; **(c)** diffractive optical element with complementary dispersion properties to that of glass.

Although both achromatic doublets and diffractive elements can help reduce chromatic aberrations, they may not provide the level of correction needed for super-resolution microscopy where further and finer corrections are required.

## 2.3 Nanometer stabilization of a microscope with local gradients

Single-molecule localization microscopy relies on accurate subpixel localization of fluorophores. However, due to the high power of the excitation beam and the long acquisition times required, these setups usually suffer from thermal and mechanical drifts. To preserve the nanometer accuracy throughout the entire SMLM acquisition, it's crucial to find a way to minimize it. As we discussed in the previous section, many algorithms have been developed to correct for this displacement after image acquisition. However, they may not always be applicable, as the drift might be too large to be compensated in postprocessing. Consequently, a real-time adjustment is required to properly correct for drifts.

This section reports the active stabilization system we developed to control the position of the objective or sample chamber, estimate the drift and rapidly compensate for it in real time ("Particle localization using local gradients and its application to nanometer stabilization of a microscope"; Kashchuk A. V., Perederiy O., *Caldini C*., Gardini L., Pavone F. S., Negriyko A. M. & Capitanio M. (2022), ACS nano, 17(2),

1344-1354) [111]. As in other methods we use a fluorescent marker attached to a coverslip as a reference to estimate and correct the displacement, but the localization of the particle is performed using local gradients. Although the most common way to find the position of a single particle involves applying a threshold to select the brightest pixels in the image and then calculating an intensity-weighted centroid, this approach has shown poor performance and presents several practical issues [36]. In contrast, gradient-based methods estimate the difference between adjacent pixels to identify the direction and magnitude of the intensity gradients within the image and, since particles are often imaged with radial symmetry, their location can be determined through the intersection of gradient lines [112], [113]. This approach is invariant to illumination variation, independent of background level and can also be applied for 3D localization [114]. For example, a gradient fitting algorithm has been employed in 3D localization of single particles in astigmatism-based microscopy [115]. For these reasons gradient-based methods are experimentally convenient with respect to conventional centroid intensity-based ones.

Let's now describe our local gradient algorithm (LoG) workflow. First, we define a local gradient in each point as the intensity weighted centroid of all the pixels within a radius r from that point (see **Figure 2.7a**). By calculating local gradients for each pixel, we obtain horizontal and vertical gradient matrices ($G_x$ and $G_y$ in **Figure 2.7a**) of the original image. Gradient matrices form a vector field that contains a gradient vector for each pixel (blue arrows in **Figure 2.7d**). The center of a radially symmetrical particle can be determined as the intersection of all the gradient lines. However, it could happen that, due to noise or uneven illumination in the background of the image, gradient vectors with random or incorrect orientation are created. Since these artifacts could potentially disrupt the center estimation process, to minimize their effects on the localization, we estimate the magnitude (Euclidean

48
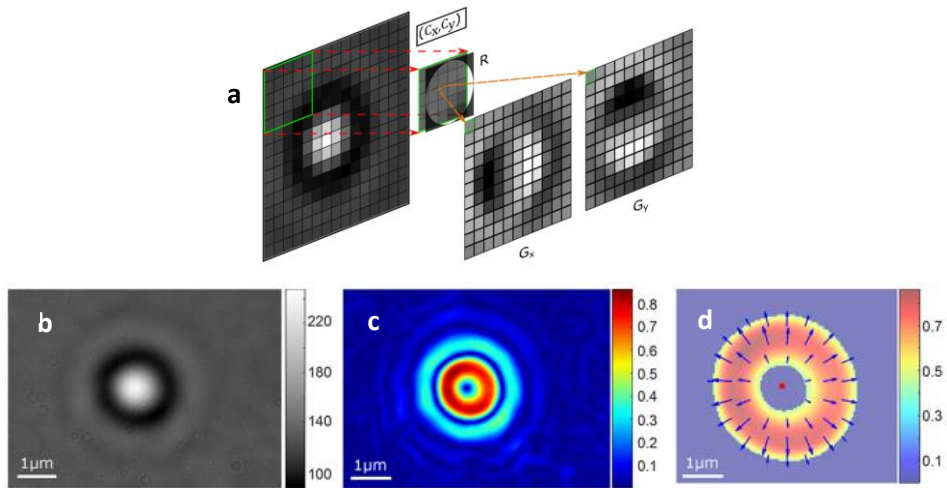
**Figure 2.7:** Localization of a single molecule through local gradients. **(a)** Visualization of local gradients; **(b)** Brightfield image of a 0.9 μm silica bead; **(c)** Magnitude of local gradients; **(d)** Magnitude of local gradients after thresholding where arrow show the direction of gradients from high to low. Image retrieved from [111].

norm) of gradient vectors and exclude low-magnitude values (**Figure 2.7c, d**). Finally, the center of the particle is calculated by using the least-squares method applied to gradient lines with the highest magnitude of gradient vector.

Regarding 3D localization, as discussed in section 1.3.1, different techniques can be used to determine the axial position. The easiest one, is to use a cylindrical lens to produce a slight astigmatism of the PSF of the system. The PSF becomes an ellipse whose ellipticity depends on the axial position of the emitter with respect to the focal plane. When the emitter is in the focal plane the PSF is round, when it is whether above or under the focal plane it becomes elliptical (see **Figure 2.8d**). By calibrating the system, i.e. by finding the relation between the shape of the PSF and the axial position of the emitter, it is possible to use this method to perform 3D localization of a single molecule. In the LoG algorithm, it is possible to transform the local gradient image of the fluorescent particle with introduced astigmatism into an ellipse by adjusting the window size r. (**Figure 2.8b**). The calculation procedure is shown in **Figure 2.8b,c**. First, the image is
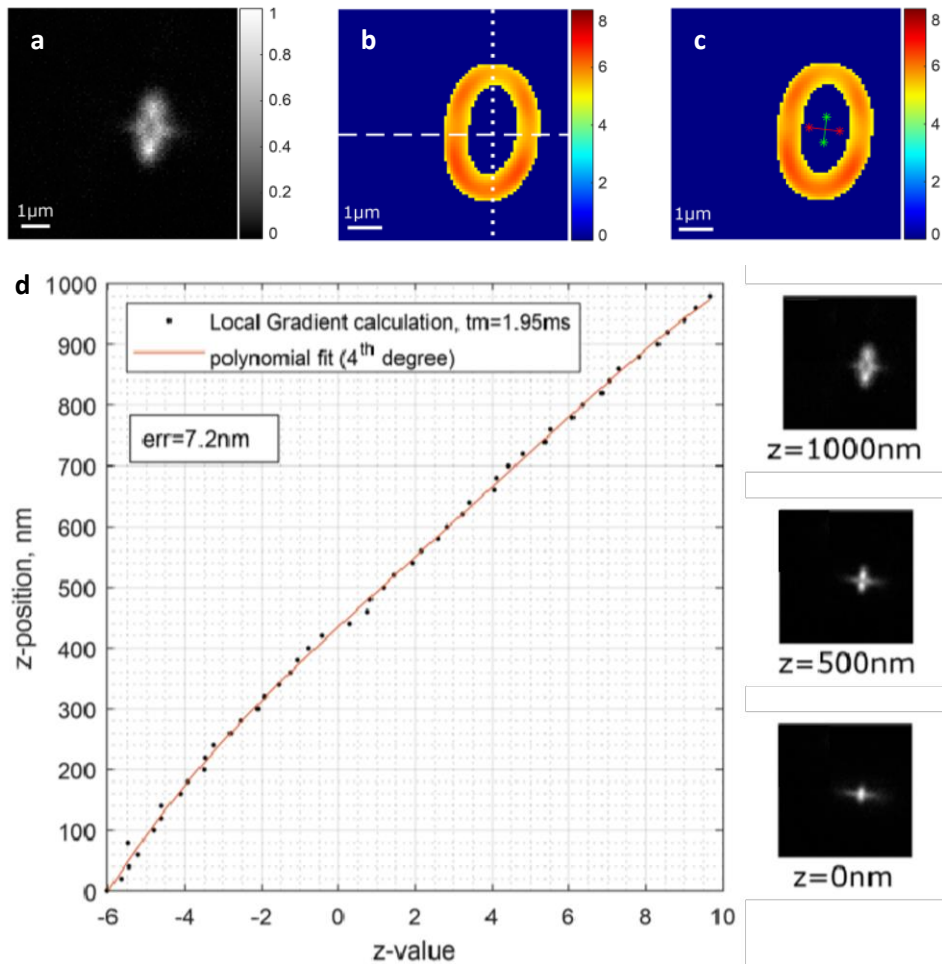
**Figure 2.8: (a)** Image of a single fluorescent particle (0.51 μm diameter) attached to a coverslip. Astigmatism is introduced by a cylindrical lens and the imaging plane is ≈500 nm above the surface. **(b)** Magnitude of local gradients. Dashed and dotted lines are showing the top/ bottom and left/right split of the local gradient images for z-value estimation, correspondingly. **(c)** Two axes (green and red lines) are built from the centers of split gradient lines. **(d)** z-Value calibration curve in astigmatism-based microscopy. The average error for predicting a z-position of the particle is 7.2 nm. Image and caption retrieved from [111].

thresholded based on the magnitude of the gradient. After determining the xy-position as explained before, the image is divided into top/bottom or left/right sections relative to the particle's center. For each section, a least-squares intersection of gradient lines is computed, yielding four points that define two axes. The length of the major axes is used to determine the z-value. As in centroid intensity-based methods, also in LoG algorithm a calibration prior to imaging is
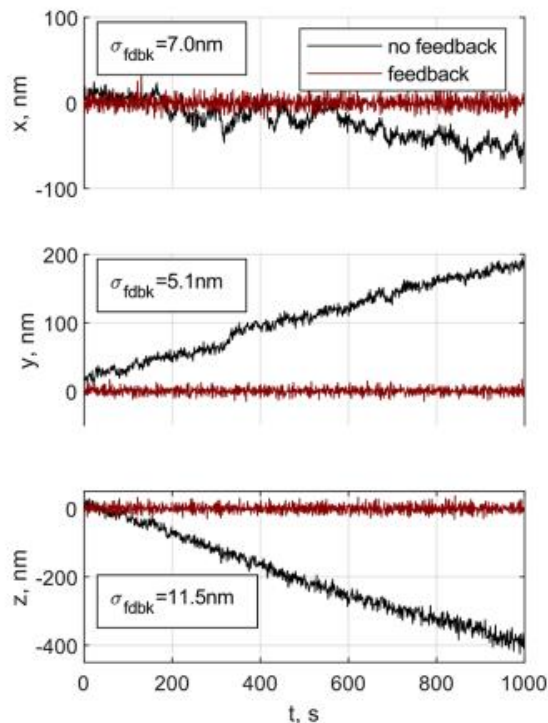
**Figure 2.9:** 3D tracking of a fluorescent bead (0.51 μm diameter) attached to the coverslip with feedback system on (red) and off (black). 3D localization was performed using astigmatism as described in the text. Inset indicates the standard deviation of the signal with feedback on. Image retrieved from [111].

required. In this case, instead of finding the relation between the PSF's shape and the z-position, we find the one between the z-value and the z-position (**Figure 2.8d**).

To test the performance of the feedback system using the LoG algorithm, we tracked a single particle of 0.51 μm diameter in 3D for 1000 s. The calibration curve for the z-value was recorded on the same bead before the acquisition. The results for both feedbacks controlled and free-running cases are shown in **Figure 2.9**. We successfully achieved stable positioning of the sample, with a standard deviation of the position ranging from 5-7 nm for x,y-localization and 11.5 nm for z-localization. Next, we applied the feedback system to record a 3D-STORM image of the actin cytoskeleton of a mammalian cell using a fluorescent bead as a fiducial marker. For comparison, we also
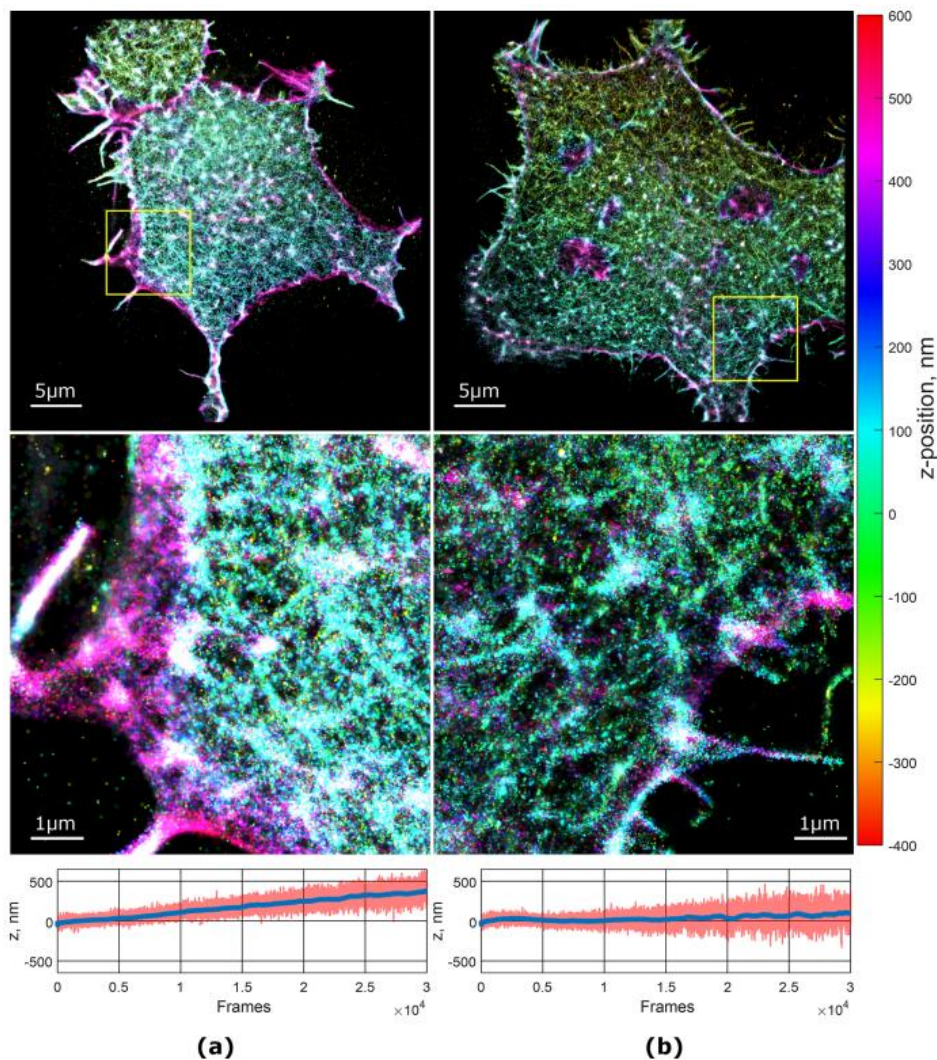
**Figure 2.10:** Reconstructed 3D STORM images of cells without feedback correction **(a)** and with feedback **(b).** Plots under the images show the change in the average z-position (red line) of all detected fluorophores (blue line represents moving average of 1000 points). Image and caption retrieved from [111].

recorded a 3D-STORM image of the actin cytoskeleton in a different cell from the same sample without employing the feedback system (**Figure 2.10a**). Additionally, we assessed the axial drift by calculating the average position of all detected fluorophores for each frame (lower panels in **Figure 2.10a,b**). The actin cytoskeleton shows an irregular distribution within the cell's volume, characterized by a dense,

branching cortex that extends around 200-300 nm from the cell membrane and a less dense network that reaches towards the cell nucleus. When there is axial drift in the viewing plane, the average z-position of all fluorophores in a frame will drift as well. The axial drift is clearly visible in the images acquired in the absence of feedback, in contrast to the observations made with the feedback (plots in **Figure 2.10**). Therefore, the image acquired with the feedback (**Figure 2.10b**) appears sharper and reveals finer details compared to the one acquired without feedback.

## 2.4    Experimental setup

In this section it is reported the optical system that we developed to perform three-dimensional simultaneous multicolour super-resolution microscopy. As shown in **Figure 2.11a**, in the setup there are three diode lasers with wavelengths of 552 (Coherent, OBIS LS 552 nm 100 mW), 488 (Coherent, OBIS LS 488 nm 100 mW) and 405 (TOPTICA, iBeam smart PT 405 60 mW), respectively.  The excitation beam from the laser is either reflected by a mirror (M1 for 552 nm) or a dichroic mirror (DM1/DM2 for 488/405 nm) and directed towards the telescope L1 (f = 50 mm) – L2 (f = 500 mm), which magnify it by a
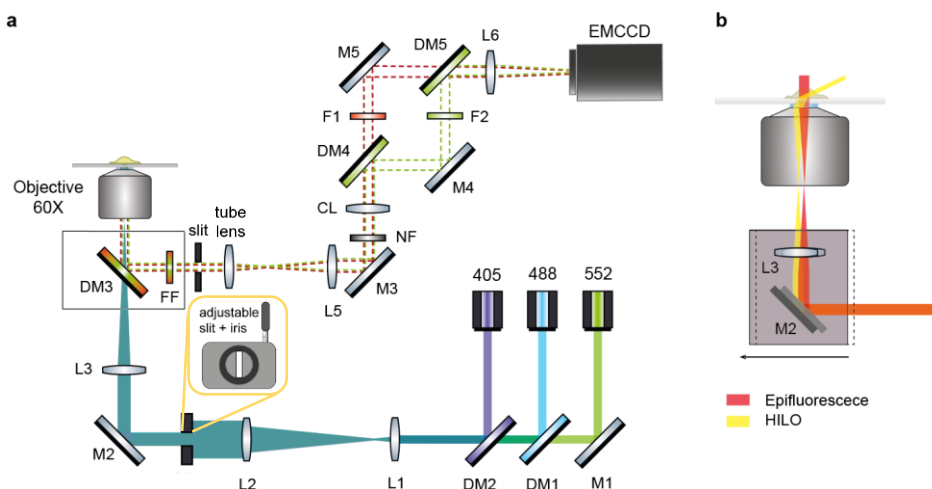


**Figure 2.11:** Scheme of the experimental setup. Panel **(a)** depicts the complete setup, whereas **(b)** outlines the available excitation methods, which include epifluorescence and HILO.

factor of 10. After the telescope, a circular iris is placed in a plane conjugated with the image plane and it is used to adjust the size of the excitation beam to ensure uniform illumination across the entire field of view. Subsequently, the beam is reflected by mirror M2 and focused through lens L3 (f = 500 mm) into the back focal plane of a TIRF Objective (Nikon 60x oil-immersion objective, 1.49 NA). Both the mirror M2 and the lens L3 are mounted on linear motorized translators (Phyisk Instumente, M-014.D01 and M-126.CG) that enables adjusting the angle of incidence of the excitation light, thus determining the type of illumination (epifluorescence widefield, HILO or TIRF) as shown in **Figure 2.11b**. The objective is mounted in an inverted configuration, and the excitation is separated from the emission through the dichroic mirror DM3 (Chroma, ZT488/561rpc-uf2), which directs the latter towards the detection path. Here, the produced image is first filtered through emission filter FF (Semrock, FF01-515/588/700-25) so that only the fluorescence emission is allowed to pass and to be focused by the tube lens (f = 200 mm). Finally, lenses L5 (f = 50 mm) and L6 (f = 150 mm) form a telescope that magnify the image by a factor of 3 before focusing it onto the detector to meet the pixel dimension of about 82 nm needed for optimal fitting of the PSF in single molecule localization method. To achieve simultaneous imaging of two colours, first we use a rectangular slit to select half of the imaged field of view, then, thanks to the identical dichroic mirrors DM4 and DM5 (Semrock, LM01-552-25.0x35.6), the short band fluorescence filters F1 (Semrock, FF01-595/31-25) and F2 (Semrock, FF01-511/20-25) and the mirrors M4 and M5, we separate the emissions of the two fluorophores and we direct them to the detector, an EMCCD camera (Andor iXon X3). The final field of view for each wavelength is about 21 x 42 $\mu m^2$.

The objective is mounted on a piezoelectric translator (Phyisk Instumente, P-721.C PIFOC) to allow adjustment of image focal plane (z-axis). Additionally, the sample is also mounted on a piezoelectric

stage (Phyisk Instumente, P-527.2CL) that enables independent movements along the x and y axes. Between L5 and L6, a weakly cylindrical lens with a focal length of 1 m is placed, which allows encoding the z-position through astigmatism and performing 3D measurements of biological samples. Since the cylindrical lens is mounted on a movable support, it can be easily removed, allowing for the use of the setup for both 2D and 3D measurements. According to what found in literature [49], [116] we positioned the weakly cylindrical lens (CL) on the Fourier plane (approximately 5 cm from first lens L5 and 15 cm from lens L6). In this position, the beam is collimated, so the introduction of a cylindrical lens with a long focal length induces the astigmatism effect, but without altering the beam or significantly degrading the lateral resolution of the system. In the detection path, a notch filter F2 (Semrock, NF03-405/488/561/635E-25) is placed, which attenuates the laser wavelengths by approximately 7 orders of magnitude. This filter is crucial to ensure that only fluorescence emission reaches the detector, as in this type of measurements, where the goal is to detect the fluorescence emitted by single molecules, it is essential to minimize any other contribution to the signal.

All the instruments (lasers, camera, translators...etc.) are interfaced and controlled with a homemade LabVIEW program. The software for active nanometer stabilization of the microscope we developed – previously described in section 2.3 – ensures that mechanical and thermal drifts are minimized and it is possible to perform long time 3D single molecule experiments without compromising the lateral resolution of the system.

I reported more details on how I implemented the Dual View optical system and optimized its alignment in section 6.1, while astigmatism calibration procedure is described in sections 6.2. Moreover, further information about HILO illumination can be found in section 6.3.

## 2.4.1 Chromatic aberrations correction

As discussed in section 2.2.3, chromatic aberrations affect multicolour imaging causing different wavelengths to travel different optical paths and thus to be focused on different focal planes. Although there are special optics, such as achromatic doublets, that can be used to minimize the aberrations, further and finer correction is required when performing multicolour super-resolution imaging when a precision in the order of the nanometer is required. Before the advent of single molecule techniques, it was thought that chromatic aberrations could be corrected by means of a simple geometrical rigid transformation. As researchers start measuring distances with a precision of a few nanometers, it became clear that such an approach was not precise enough. In Single-Molecule High-Resolution Colocalization (SHREC) [117] the different paths undertaken by the wavelengths due to chromatic aberration cause images originating from different wavelengths not to map onto each other through a rigid geometric transformation. As a consequence, a more complex non-rigid transformation function is needed to map all points from one channel to another. This procedure requires a calibration measurement (see section 6.5.1) which should be performed prior to every imaging experiment. The calibration measurement consists in the acquisition of the signal from fiducial markers emitting fluorescence in both channels to obtain the mapping function. To do this we used Tetraspeck™ microspheres (ThermoFisher, T7279, 0.1 μm, blue/green/orange/dark red) whose size – 100 nm diameter – is below the resolution limit and thus their images will correspond to the PSF of the optical system. These beads are stained with four different fluorescent dyes, with the result of having beads that display four different well-separated excitation/emission peaks: 360/430 nm (blue), 505/515 nm (green), 560/580 nm (orange), 660/680 nm (dark red). Given the excitation wavelengths, dichroic mirrors, and filters in our setup, these beads prove to be the most appropriate fiducial

markers. To calibrate the system, we prepared a sample with Tetraspeck™ beads (as described in section 6.4.1) and with the piezoelectric stage we scanned the field of view to create a grid of corresponding points in both channels. Once the grid of points coordinates is obtained from the fitting of the intensity profile of the single beads, we run a custom *Matlab* algorithm which I have developed, that use this grid to get the non-rigid transformation function used to correct the localizations.

The algorithm uses a function called *fitgeotform2d* to fit a local weighted mean transformation to the control point pairs [118]. It should be noted that, given two sets of 3D points $(x_i, y_i, X_i)$ and $(x_i, y_i, Y_i)$, two functions are required to fit them. For this reason, our algorithm calculates two functions, $f(x, y)$ and $g(x, y)$, one per each coordinate. Since the interpolation method is the same for both, I only explain how to obtain the transformation function for the x-coordinates.

First, the algorithm selects a control point $(x_i, y_i)$ and the corresponding control point in the other channel $(X_i, Y_i)$. Then it measures the distance between the control point and the 8 nearest adjacent points (**Figure 2.12a**): the longer distance is selected as the
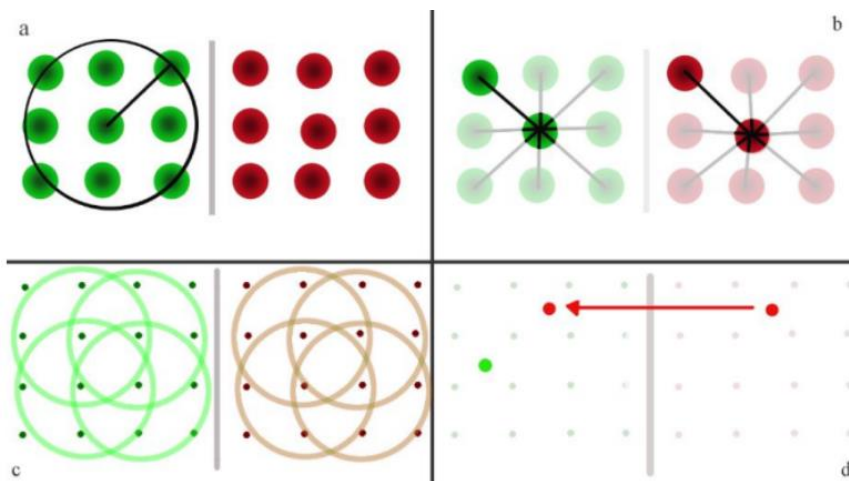


**Figure 2.12**: Main steps of the algorithm I developed to correct for chromatic aberrations.

radius of influence of the transformation function $(R_n)$ that will be calculated for that point and, therefore, for that area (**Figure 2.12b**). After this, the algorithm infers a polynomial at each control point using neighboring control points. This results in a local transformation function and an associated radius of influence for it. By repeating the same series of calculations for each control point, we end up with a series of polynomial transformation functions and their associated radii of influence (**Figure 2.12c**). The global transformation function at an arbitrary point $(x, y)$ is calculated as weighted sum of polynomials having a nonzero weight over that point:

$$f(x,y) = \frac{\sum_{i=1}^{N} W_i(R) \cdot P_i(x,y)}{\sum_{i=1}^{N} W_i(R)} \tag{2.1}$$

Where $P_i(x, y)$ is the polynomial passing through the measurement $(x_i, y_i, X_i)$ and its 8 nearest adjacent points, while $W_i(R)$ is the weight function assigned to the $P_i(x, y)$ defined as:

$$\begin{cases} W_i(R) = 1 - 3R^2 + 2R^3 & 0 \leq R \leq 1 \\ W_i(R) = 0 & R > 1 \end{cases} \tag{2.2}$$

With $R = \sqrt{(x - x_i)^2 + (y - y_i)^2}/R_n$. For how the weight function is defined, it guarantees that the associated polynomial will have no influence on points whose distance from the control point is larger than $R_n$ (radius of influence). Moreover, since the first derivative of the weight function is null for $R = 0$ and $R = 1$, the weighted sum of the polynomials is continuous and smooth at all values of $(x, y)$, including points where the effect of the polynomials ceases to exist [118].

Thanks to the transformation functions, we can map each point of the field of view to the corresponding coordinate in the other channel. Once an object in the red channel is localized, its position relative to the control points is used to calculate the corresponding position in the green channel (**Figure 2.12d**). **Figure 2.13** reports an acquisition
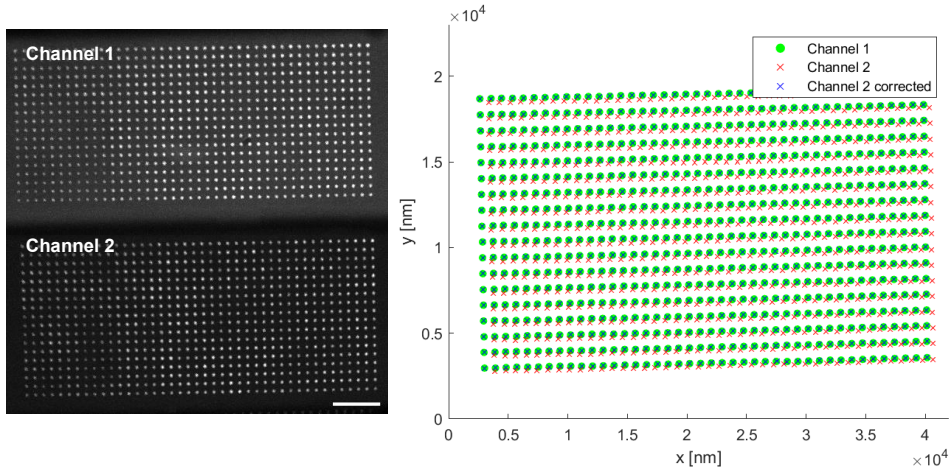
**Figure 2.13:** Example of an acquisition (left) where localizations in channel 2 are mapped in channel 1 using the non-rigid transformation function obtained with my algorithm (right). For this calibration measurement the scanning step size was 900 nm. Scalebar: 5 µm.

where the points of the grids in the two channels have been localized and corrected using my algorithm.

To estimate the registration accuracy of the transformation function we calculate the *fiducial registration error* (FRE), which is the distance between pairs of corresponding control points after the transformation [119], [120]. Given N control points, the FRE between control points in channel one ($x_{(i,1)}$ with $i = 1, \ldots, N$) and corresponding control points in channel two obtained through the transformation function ($f_{LWM}(x_{(i,2)})$ with $i = 1, \ldots, N$) is:

$$FRE_x = \sqrt{\frac{1}{N} \sum_{i=1}^{N} [x_{(i,1)} - f_{LWM}(x_{(i,2)})]^2} \qquad (2.3)$$

This is the FRE along the x axis. In the same way can be calculated the FRE along the y axis ($FRE_y$). The total FRE is then obtained as quadratic sum of $FRE_x$ and $FRE_y$.

To find the best scanning step size, that is the one with the lowest FRE, I performed the calibration with different scanning step size, from 200
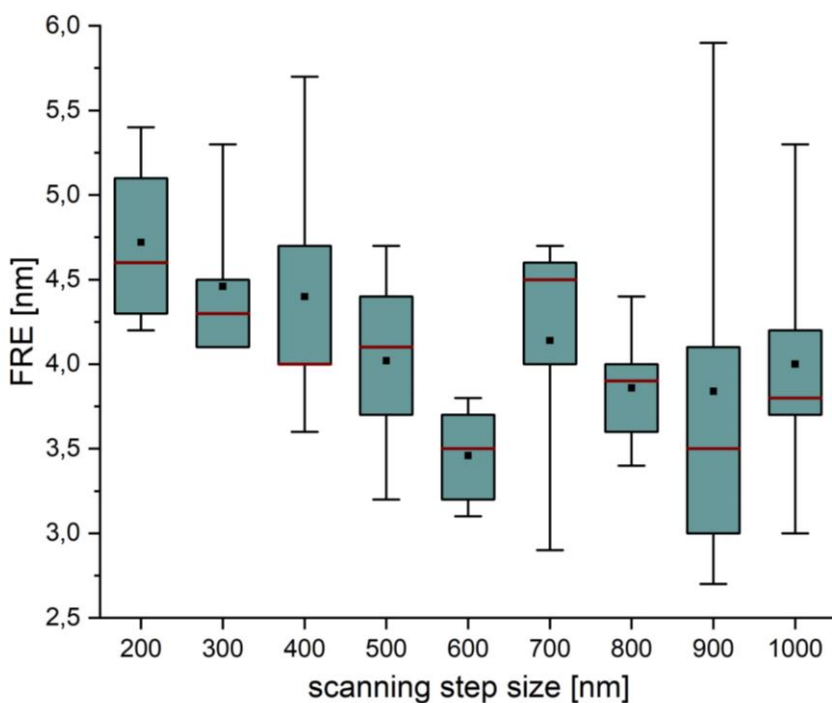
**Figure 2.14:** Comparison of FRE between different scanning step sizes. The red line and the black square in each box are respectively the median and mean value.

nm to 1000 nm. All the measurements were performed as described in section 6.5.1. The grid should cover most of the field of view because once the measurements are performed, only the localizations of molecules whose image falls within grid area can be corrected through the transformation function. Although fluorescent beads are quite stable in terms of emission intensity, imaging the same bead for a long time causes it to photobleach and becoming less bright over time. Lower intensity worsens the precision of localization of the single molecule and, consequently, decreases the precision of the transformation function. Thus, it's necessary to find a compromise between covering most of the field of view and having a high precision transformation function. To understand which is the best scanning step size I performed five acquisitions per step and, after having localized single molecules and applied the transformation function, I estimate the FRE for each of the five acquisitions. **Figure 2.14** compares

the registration errors of different acquisitions and, as we can see, the ones with the lowest median values correspond to 600 nm and 900 nm step sizes. However, 900 nm shows a higher FRE variability (i.e. higher standard deviation) compared to 600 nm, so we decided to use 600 nm as optical scanning step size. The FRE associated to this scanning step size is 3.5 nm.

## 2.4.2 Crosstalk correction

After correcting for chromatic aberrations, the second issue to take care of in a multicolour acquisition is the crosstalk between the two colour channels. Since the signal crossover affects the localization accuracy, it is of crucial importance to correct for it to minimize its impact on the image resolution. For this purpose, I have developed an algorithm that corrects the crosstalk in every pixel of each frame of the acquisition. The algorithm compares the gray values of corresponding pixels of the two channels to estimate the signal crossover and remove it.

First, it estimates the non-rigid transformation function to correct the images for chromatic aberrations. This transformation function is slightly different from the previous one because is estimated starting from the pixel coordinates of corresponding points of the grid, instead of their sub-pixel positions as crosstalk correction must be performed before localizing single molecules. Thanks to the transformation function all the pixels can be mapped from one channel to the other. Then for each pixel it estimates the *crosstalk factor* (CF), that is the fraction of signal recorded into the other channel. Given a fluorescent dye whose emission should be recorded only in channel 1 ($I_{Ch1}$), but due to crosstalk is also recorded in channel 2 ($I_{Ch2\ crosstalk}$), the crosstalk factor for each pixel can be calculated as:

$$CF = \frac{I_{Ch2\ crosstalk}}{I_{Ch1}} \qquad (2.4)$$

The CF allows us to estimate the crosstalk signal for every pixel of each frame. The right gray values can be obtained from the measured ones as:

$$I_{Ch2\ real} = I_{Ch2\ measured} - CF \cdot I_{Ch1} \qquad (2.5)$$

Where $I_{Ch2\ real}$ is the signal of channel 2 without crosstalk, $I_{Ch2\ measured}$ is the recorded value which includes real signal and crosstalk. This correction is applied to all the pixels of channel 2 whose gray value is higher than the mean background value.

### 2.4.3 Localization error

To estimate the localization error, I prepared a sample with fluorescent beads attached to the glass coverslip (as described in section 6.4.1) and acquired 10 frames for over 15 different fields of view, with the same acquisition parameters used for astigmatism calibration (see section 6.2). After imaging, I first localized single
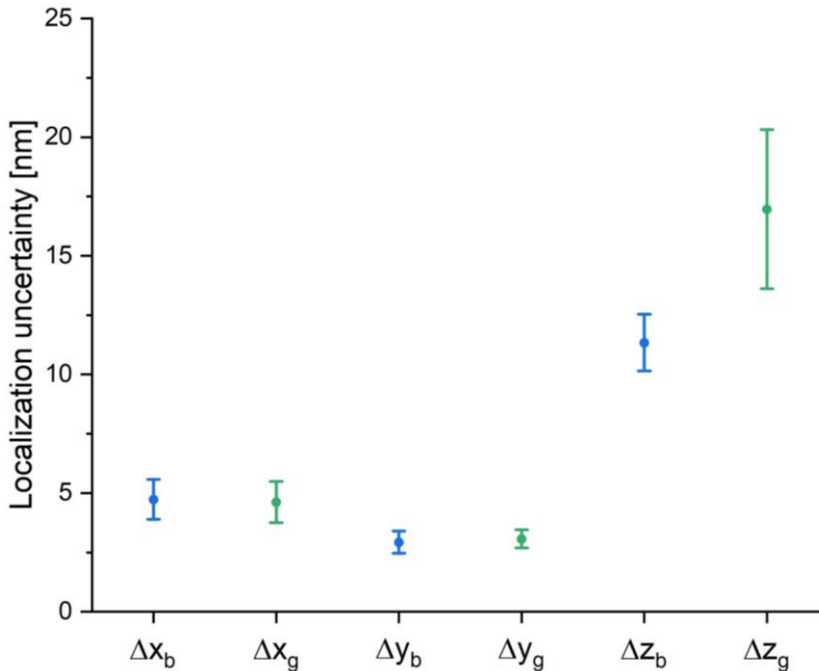


**Figure 2.15:** Localization error estimated for the x, y, z coordinates of the two channels. The dots represent the mean values, while the bars are the standard deviations calculated considering the localization errors of each fluorophore.

molecules and then I estimated the localization error of individual fluorophores as the standard deviation of multiple localizations of the same molecule. Considering all the fluorophores acquired in the different fields view ($N = 85$), I obtained an average value of $\Delta x_b = (4.7 \pm 0.8)$ nm, $\Delta y_b = (2.9 \pm 0.5)$ nm and $\Delta z_b = (11.3 \pm 1.2)$ nm for the blue channel and $\Delta x_g = (4.6 \pm 0.9)$ nm, $\Delta y_g = (3.1 \pm 0.4)$ nm and $\Delta z_g = (17.0 \pm 3.4)$ nm for the green channel (**Figure 2.15**).

## 2.5 Results

In this chapter I demonstrated that through relatively simple algorithms it is possible to implement a SMLM setup to perform three-dimensional multicolour super-resolution imaging with few nanometers accuracy in both colour channels.

First, we used an active nanometer stabilization of the microscope to minimize mechanical and thermal drifts. This ensures that even performing long time 3D single molecule experiments, such as 3D STORM acquisitions, the resolution is not compromised due to drifts.

Then, I developed an algorithm to finely correct for chromatic aberrations. My algorithm requires a calibration prior to imaging where the field of view is scanned to create a grid of control points. I demonstrated that the best way to perform this calibration is using a scanning step size of 600 nm, because it corresponds to the lowest FRE (around 3.5 nm).

Finally, I developed an algorithm to finely correct for possible crosstalk. My algorithm corrects each pixel of every frame of the acquisition, thus ensuring that colocalization or object-based measurements are performed without having false positives due to crosstalk.

# Chapter 3

# Studying molecular compartmentalization in bacteria through single molecule co-localization

Cellular compartmentalization is the separation of the intracellular volume into distinct compartments with specific local conditions and materials that enable the simultaneous execution of different metabolic reactions in the most efficient way. Compartmentalization is crucial for regulating cell's functions because, by providing specialized compartments, it increases the cell efficiency by reducing the loss of intermediate products. Yet, while the compartmentalization of eukaryotic cells is thoroughly understood, very little is known about prokaryotic one. For a long time, it was thought that prokaryotic cells, such as bacteria, completely lacked any kind of subcellular organization and that all biochemical reactions occurred in a disorganized manner. However, in recent years, several studies on metabolic pathways have raised the evidence for a certain degree of intracellular organization within bacteria too (see section 3.1). Molecular biology provides different techniques to study molecular interactions, such as the *two-hybrid systems* [121], [122] (see **Figure 3.1**), but an imaging approach is needed to obtain spatial information about those interactions. Studying spatial localization at the molecular level requires super-resolution techniques that can reach the nanometer scale. Simultaneous multicolour SMLM is perfectly suitable for this purpose because it enables the localization of different types of single
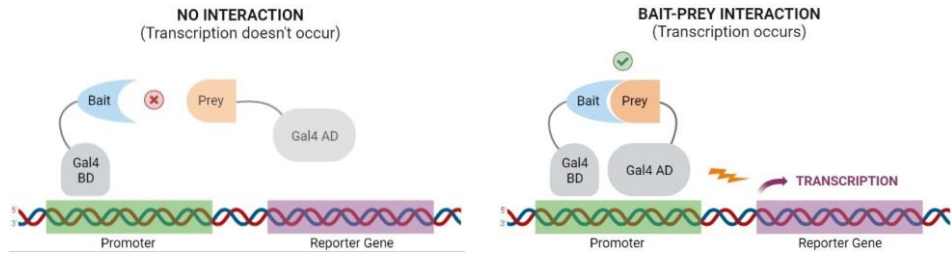
**Figure 3.1:** The *Yeast Two-Hybrid System* is a molecular biology technique that relies on the activation of the transcription of a gene reporter by the binding of a transcription factor (*Gal4*) onto an activating sequence (*Promoter*). The transcription factor is split into two domains, activating domain (*AD*) and binding domain (*BD*), whose interacting enable the transcription. Since each protein of interest (*Bait* and *Prey*) is fused to a domain, only interacting proteins can bring the two halves of the transcription factor together and activate the transcription of the reporter gene.

molecules at the same time with tens of nanometers accuracy in the three dimensions in both fixed and living cells. In this chapter I show how I applied the setup I developed to study molecular compartmentalization. After introducing the biological problem and the samples of choice, I show how to use single molecule co-localization to unveil the subcellular organization in bacteria.

## 3.1 Introduction to the biological problem: hypothesis on the subcellular organization of bacteria

The cellular environment is densely populated with macromolecules, constituting 20-30% of cellular interiors at a protein concentration of 200-300 mg/ml. This high protein density forms a gel-like structure, thus impacting the diffusion processes of enzymes and metabolic intermediates, and leading to the loss of time and energy required for their interaction [123], [124], [125]. Molecular crowding and hindered diffusion prompt the necessity for compartmentalized metabolic pathways, a well-established phenomenon in eukaryotic cells but less obvious in prokaryotes [126]. However, contrary to the historical perception of bacterial cells as disorganized "bags of enzymes", recent research revealed that the cytoplasm of prokaryotes contains various highly ordered structures, such as multienzyme complexes and metabolons [127], [128], [129]. Multienzyme complexes exhibit

variable structural organization, potentially representing the initial stage of higher protein organization [126], while metabolons, defined as sequential enzymes complexes, involve transient interactions of proteins catalyzing sequential reactions of a metabolic pathway [130]. However, since these interactions are weak, they tend to disrupt during purification procedures and only a limited number of enzymes were identified as parts of metabolons [126]. Multienzyme complexes and metabolons are crucial for channeling metabolic pathways, thus enabling the preferential transfer of an intermediate from one enzyme to a physically adjacent one, and restricting diffusion into the surrounding environment. This process offers protection for unstable or scarce metabolites by keeping them in a protein-bound state, and provides a metabolic advantage through the maintenance of concentration gradients, thus yielding kinetic advantages [124].

Among the different metabolic pathway, the study of the histidine biosynthetic pathway, begun over 50 years ago [131], has been pivotal in unraveling fundamental biology mechanisms, and it represents a cornerstone in modern cell biology concepts [132]. Examination of histidine biosynthetic enzymes reveals that at least seven *his* genes (*hisD, hisN, hisB, hisH, hisF, hisI and hisE*) undergo different fusion events, thus promoting the channeling of intermediates [133], [134], [135]. Moreover, it has also been suggested that proteins encoded by the four genes *hisBHAF*, recognized as the "core" of histidine biosynthesis, could potentially interact to create a metabolon [133]. The significant level of sequence conservation observed in the *his* core genes supports the idea that interacting proteins have more functional constraints than stand-alone ones [136]. This idea agrees with the notion that genes encoding proteins that must interact to form an active complex are very often clustered in conserved operons [137], [138]. In the past years, several different models have been proposed to explain the origin and evolution of operons [139], however, an additional hypothesis can be formulated: the organization of genes in

operons within the same metabolic pathway may be influenced by the physicochemical characteristics of the cell's crowded cytoplasm, where restricted diffusion of metabolic enzymes and solutes occurs. While the idea that physical interaction between encoded proteins contributes to the evolutionary conservation of gene order is longstanding [140], recent observations challenge the notion that operon organization is solely driven by the need for protein colocalization and interaction [138]. Despite the diverse structures and organizations of genes within the same metabolic pathway in different taxonomic groups, the structural organization of the bacterial chromosome may provide insight. DNA is folded to fit inside the cell [141]; however, despite being highly compacted, the nucleoid remains accessible for cellular processes such as transcription and replication [142]. One possible hypothesis suggests that the folding of DNA might bring distant genes into physical proximity, leading to the co-localization of the encoded proteins. To validate this hypothesis, a direct observation of the spatial distributions of genes and proteins is required and, since molecular biology techniques cannot provide it, an imaging technique must be applied.

## 3.2 E. Coli PHPF and PHPaaC plasmid inserts

As discussed in the previous section, the study of the histidine metabolic pathway has been fundamental to understanding many biological processes. In the last years, several research on the *his* genes fusions in different phylogenetic have suggested a compartmentalization of the biosynthetic enzymes [136], [137], [138]. However, since those studies were carried out using molecular biology techniques, no evidence of the spatial distributions of histidine biosynthetic enzymes has been proven yet. To demonstrate the molecular compartmentalization of histidine biosynthetic enzymes, it is necessary to use an imaging approach. Since our setup can perform dual-colour SMLM we decided to investigate the molecular
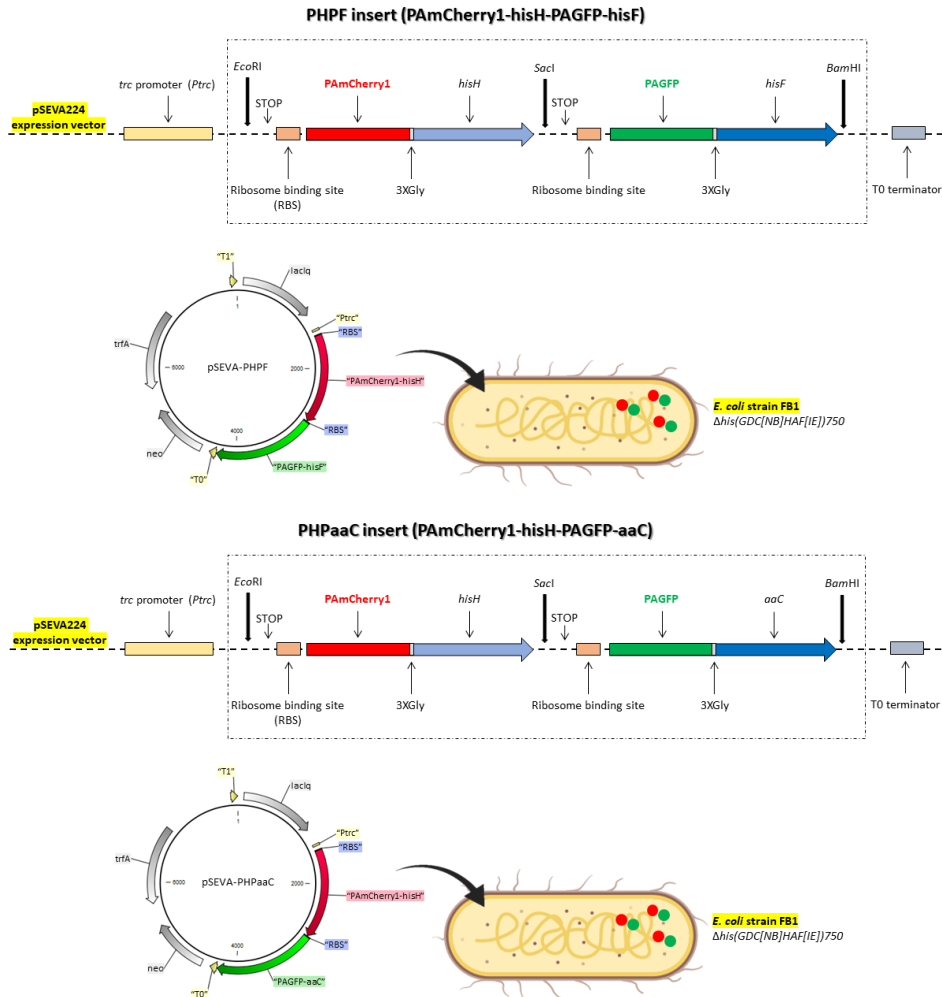
**Figure 3.2:** Plasmid inserts *pSEVA-PHPF* (above) and *pSEVA-PHPaaC* (below) used to transform E. Coli bacteria.

compartmentalization by imaging two proteins at a time. Specifically, by taking advantage of a collaboration with the group of Microbiology of Prof. Fani at the University of Florence, we decided to study the spatial distribution of the proteins *HisH-HisF* of the histidine metabolic pathway of *Escherichia Coli* (*E. Coli*) bacteria, whose interaction has already been demonstrated in 2020 through the *Bacterial Adenylate Cyclase Two-Hybrid* (BACTH) *system* [122]. To do that, we took the bacterial strain FB1 of *E. Coli* and, by inserting a plasmid, we transformed the bacteria so that each protein of interest was tagged

with a photoactivable fluorescent protein (*PAmCherry1-HisH*, *PAGFP-HisF*) and thus could be imaged and localized with nanometers accuracy. We chose the photoactivable fluorescent proteins PAmCherry1 and PAGFP for three main reasons: i) their photoswitching proprieties are similar enough to perform simultaneous dual colour imaging, ii) their absorption spectra are compatible with the excitation lasers of our setup and iii) their emission peak wavelengths are far enough to be separated and distinguished using short band fluorescence filters.

Moreover, since our hypothesis is that interacting proteins co-localize while non-interacting proteins don't, to validate it we also prepared a sample with two non-interacting proteins to see if there was a difference (as expected) between the spatial distributions of proteins in the two samples. Specifically, for the negative control sample we chose the proteins *HisH* and *aaC* and transformed bacteria with a plasmid named *pSEVA224-PHPaaC* similar to the previous one, but with PAGFP tagged with *aaC* instead of *HisF*. In **Figure 3.2** are reported the plasmid inserts used to transform E. Coli bacteria.

## 3.3  Development and optimization of the acquisition protocol for simultaneous multicolour imaging

As discussed in the previous chapter (section 2.1.3), simultaneous multicolour imaging provides faster acquisitions and avoids loss of localizations, making it more suitable for live imaging compared to sequential methods. However, it comes with some limitations. These include a smaller field of view (in setups with only one camera), a higher risk of crosstalk between fluorophores and the necessity for identical acquisition parameters[2] for both fluorophores. These limits must be considered when chromophores must be chosen among those

---

[2] With *identical acquisition parameters* we are referring to the exposure time and the gain of the EMCCD camera, as well as the power of the activation laser (405 in our case). Excitation lasers' powers can be different since each lasers excites only a specific fluorophore.
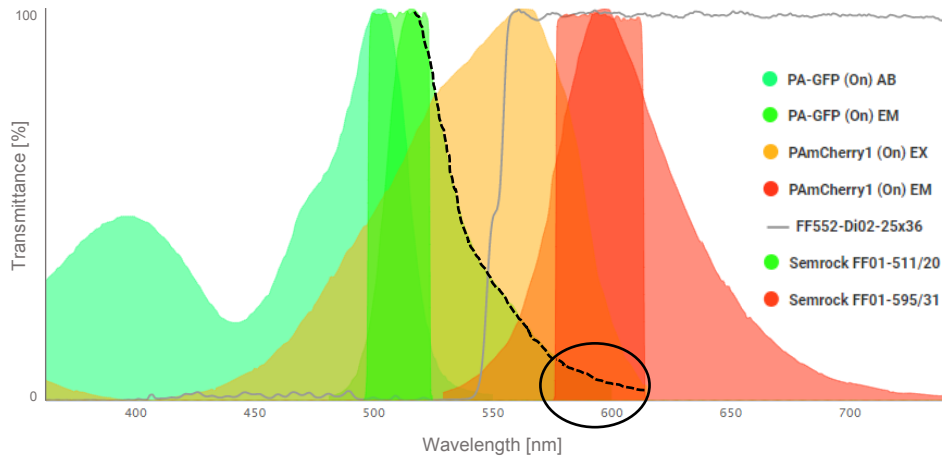
**Figure 3.3:** Transmittance as a function of wavelength of fluorescent proteins (PAGFP and PAmCherry1) and detection optical elements (dichroic mirrors and fluorescent filters) of our setup. The dashed line delimits the right part of the emission spectrum of PAGFP while the black circle highlights the crosstalk signal of PAGFP in the PAmCherry1 channel.

available. In fact, if, for example, whether the duty cycle differs significantly between the two chromophores or the activation of the fluorophores occurs at very different laser powers, simultaneous imaging may not be feasible due to an excess or deficiency of localizations of one protein with respect to the other.

In our study we perform simultaneous multicolour imaging of E. Coli bacteria. Since their dimensions are those of cylinders 1.0-2.0 micrometers long, with a diameter of about 0.5 micrometers, using only half of field of view (around 21 x 42 μm²) is good enough as there is still lots of space to image several bacteria at the same time.

Regarding the selection of chromophores, our first choice was the pair of photoactivable fluorescent proteins SkylanS (instead of PAGFP) and PAmCherry1 due to their spectral separation and shared characteristics of high brightness and photostability. However, when we tested it in our bacterial strain, we observed a significant difference in both activation laser power and photoswitching rates (of around one order of magnitude), thus making them unsuitable for simultaneous imaging. Consequently, we opted for PAGFP and PAmCherry1, as they not only exhibit good spectral separation but also have similar

photoswitching properties. However, as it can be seen in **Figure 3.3**, despite using short band fluorescent filters to separate the emissions, there's some crosstalk of the PAGFP in the PAmCherry1 channel that make it necessary to estimate and correct for the crosstalk as described in details in section 2.4.2.

Finally, to find the optimal acquisition parameters, we first found the best settings for each individual fluorophore, and then, based on these, derived the optimal settings for simultaneous imaging.

## 3.4   Measure

To perform multicolour simultaneous PALM, I prepared a sample with fixed bacteria embedded in an agarose gel as described in section 6.4.2. Since the fine correction of chromatic aberration is crucial for obtaining reliable results in super-resolution co-localization, before each set of acquisitions I also prepared a sample with fluorescent beads and scanned the field of view (as described in section 6.5.1) using a scanning step size of the piezo-electric stage of 600 nm which corresponds to the lowest registration error (as demonstrated in section 2.4.1). The detailed imaging protocol for simultaneous multicolour PALM of E. Coli with all the acquisition parameters can be found in section 6.5.2. Briefly, first I use brightfield to select the region of interest of the sample. Then, the halogen lamp is turned off and the super-resolution acquisition starts. At the beginning of each measure, the 488 laser is turned on and 10-20 frames are acquired with only PAGFP activated[3], that will be used to estimate and correct the crosstalk. Then, I activate also PAmCherry1 (by turning on 405 and 552 lasers) and perform the simultaneous acquisition. Each measure lasts around 2000 frames.

---

[3] PAGFP can be photoactivated from a dark state into bright green fluorescence upon 405-nm or 488-nm light illumination [166]. This property is very useful as it enables the selective activation of only PAGFP while acquiring frames to correct crosstalk and avoids loss of localizations of PAmCherry1 that would occur with 405-nm light activation.

## 3.5   Analysis

The analysis of multicolour imaging data consists of five main steps: 1) crosstalk correction, 2) localization of single molecules, 3) chromatic aberrations correction, 4) merging of reappearing molecules and 5) co-localization analysis. Below is reported the complete protocol that was used for each acquisition:

1)  *Crosstalk correction.* Crosstalk correction was performed using the algorithm described in section 2.4.2. As previously explained, our algorithm compares the grey values of corresponding pixels of the two channels to calculate and remove the crosstalk signal. Initially, from the acquisition with fluorescent beads, I estimate a non-rigid transformation function to correct the images for chromatic aberrations. For this purpose, I use *ThunderSTORM* [4], an open-source plugin for the image analysis program *ImageJ*, to localize single molecules and reconstruct the images of the grid in the two channels. Then, from the rendered images of the grid, through an algorithm similar to the one used to finely correct for chromatic aberration (described in section 2.4.1), I estimate a non-rigid transformation function from the pixel coordinates of corresponding points of the grid. This transformation function allows me to compare the grey values of corresponding pixels in the acquisition of bacteria and calculate the crosstalk factor as:

$$CF = \frac{(I_{PAGFP})_{Channel\ PAmCherry1}}{(I_{PAGFP})_{Channel\ PAGFP}}$$

Thus, representing the fraction of PAGFP signal recorded in the PAmCherry1 channel. The CF allows me to estimate the

---

[4] ThunderSTORM is a software developed to process and visualize images acquired with PALM/STORM imaging. See section 6.2 for further details on its data analysis process.
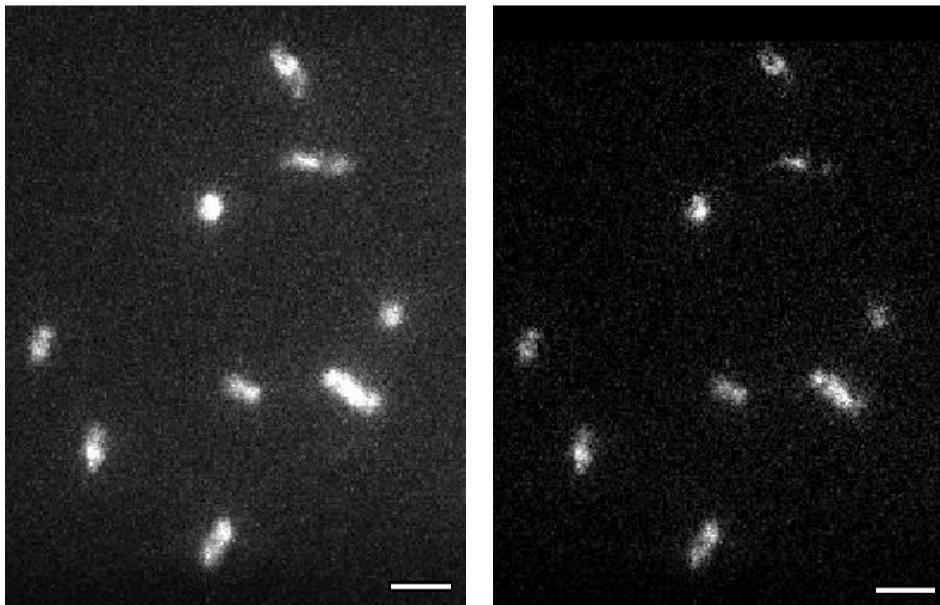
**Figure 3.4:** Example of a frame in the channel of PAmCherry1 before (left) and after (right) crosstalk correction. Scalebar: 2 μm.

crosstalk signal of PAGFP for every pixel of each frame and then subtract it to every frame of PAmCherry1 as shown in equation (2.5). A representative example of the result of my crosstalk correction method is shown in **Figure 3.4**.

2) *Localization of single molecules*. After correcting for the crosstalk signal, I performed single molecule localization of PAGFP and PAmCherry1 with ThunderSTORM using the parameters reported in **Figure 3.5**.

3) *Chromatic aberrations correction*. Chromatic aberrations correction was performed using the algorithm described in section 2.4.1. First, I used the acquisition of fluorescent beads and, then from the sub-pixel localizations of the points of the grid, I estimated a non-rigid transformation function. This transformation function differs from the previous one as it allows mapping single molecule localizations, instead of single pixels, from one channel to the other. Then, I applied the transformation to the points of the PAGFP channel to correct
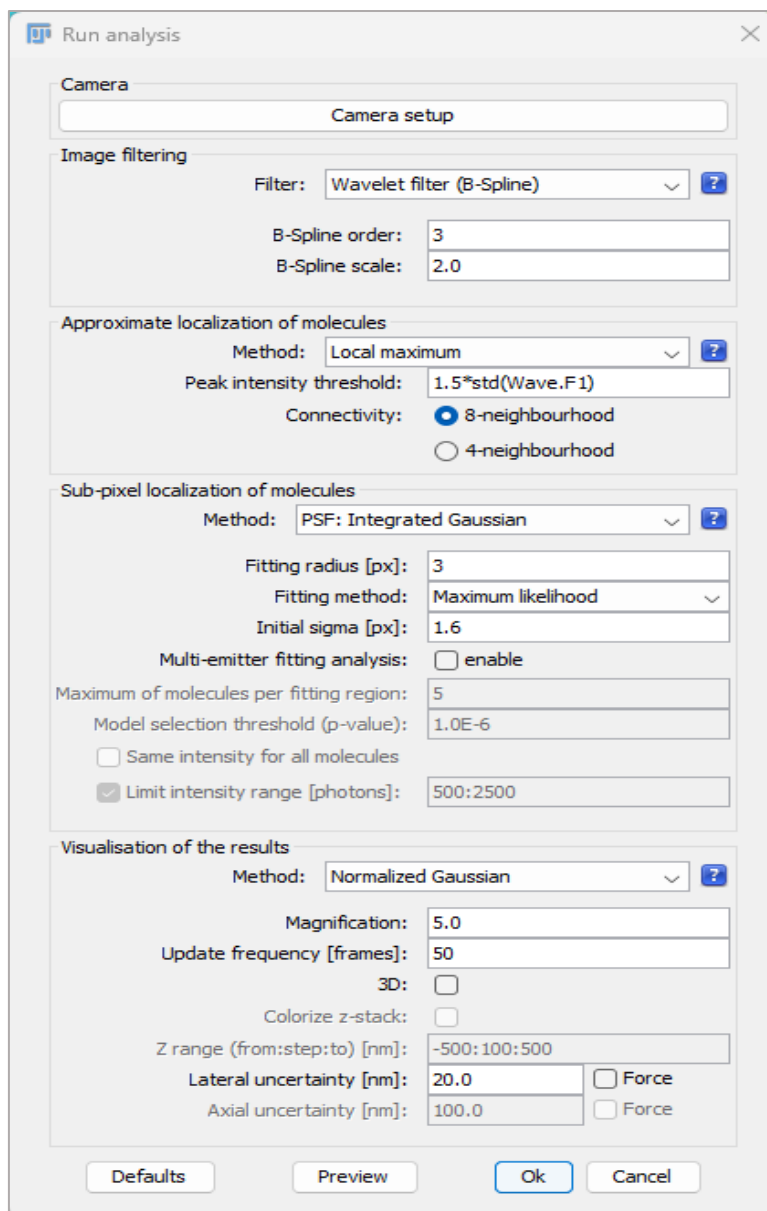
**Figure 3.5:** ThunderSTORM user interface showing the parameters used to find the sub-pixel positions of single molecules of PAGFP and PAmCherry1 in bacteria.

the chromatic aberrations. In this step I removed all the molecules that were localized out of the edges of the transformation function as the correction couldn't be performed over there. In **Figure 3.6** it is reported an example of chromatic aberrations correction using our algorithm.
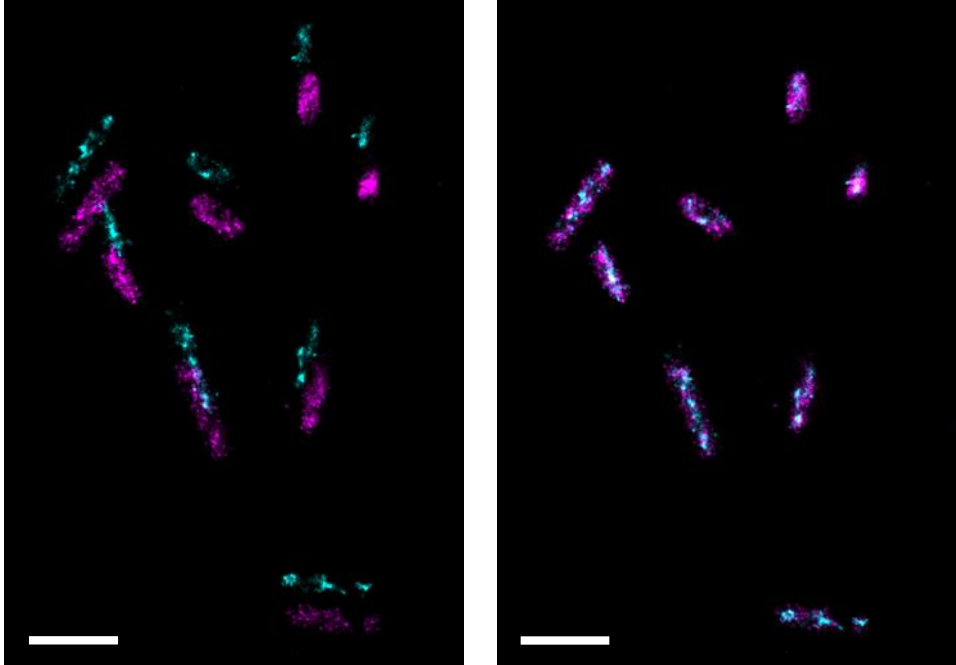
**Figure 3.6:** Example of an acquisition before (left) and after (right) chromatic aberrations correction. Cyan points are localizations of PAGFP while magenta points are localizations of PAmCherry1. Scalebar: 2 μm.

4) *Merging of reappearing molecules*. During a SMLM experiment it can happen that the same photoactivated molecule appears for several frames (consecutive or not) before permanently photobleaching. To avoid considering the same molecule twice I have developed an algorithm that removes duplicates by merging reappearing molecules. The algorithm performs a nearest neighbor search and categorizes as duplicate all the localizations closer than the mean value of the Thompson's uncertainty of the acquisition (usually around 20 nm) and separated by less than 10 frames from the initial appearance. Once duplicates are identified, they're combined into a new molecule whose position $(x_m, y_m)$ is calculated from the coordinates of the individual duplicates as intensity-weighted average as follows [143]:

$$x_m = \frac{\sum_{i=1}^{N\ duplicates} x_i I_i}{\sum_{i=0}^{N\ duplicates} I_i} , \ y_m = \frac{\sum_{i=1}^{N\ duplicates} y_i I_i}{\sum_{i=0}^{N\ duplicates} I_i} \qquad (3.1)$$

Where $x_i$ , $y_i$ and $I_i$ represent the x,y coordinates and the intensity of each duplicate, respectively. Regarding the localization uncertainty, I compute the standard deviation of duplicate positions along both axis and then select the maximum value between them.

5) *Co-localization analysis.* Once the data are corrected for aberrations and duplicates are removed, they're ready for the co-localization analysis. In conventional fluorescence microscopy co-localization is quantified by the degree of overlap of pixel intensities across the entire image or region of interest using Pearson's correlation coefficient [144] or Manders' overlap coefficients [145]. In SMLM, quantifying the co-localization is less straightforward, as generally different molecules won't occupy the exact same position. Therefore, single molecule co-localization is often defined as a metric for intermolecular distance or spatial association. During the years several methods have been developed that directly analyze point patterns by extending spatial analysis procedures [146], [147], [148] or combining cluster detection with co-localization analysis [149], [150], [151]. Our analysis exploits the local density-based co-localization index developed by Willems et al. [152]. To better understand how this index works, let's suppose to have an acquisition with two channels $A$ and $B$ (as shown in **Figure 3.7**). The co-localization index for the $i$th localization in channel A is defined as:

$$CI_i^A = \frac{N_{Ai}^B(d_B)}{\overline{LD}_B} \qquad (3.2a)$$

where $N_{Ai}^B$ is the number of localizations in channel $B$ within the distance $d$ around the $i$th localization in channel $A$ and $\overline{LD}_B$ is the mean local density of the localization in channel $B$.
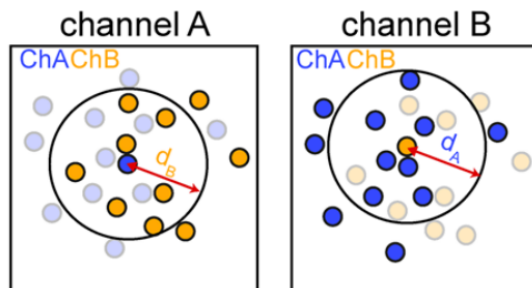
**Figure 3.7:** Concept of local density-based co-localization index. Image retrieved from [152].

Similarly, the co-localization index for each localization of channel $B$ can be calculated as:

$$CI_i^B = \frac{N_{Bi}^A(d_A)}{\overline{LD}_A} \qquad (3.2b)$$

Thus, the co-localization index of any given localization is a measure of the local density of nearby molecules in the other channel [152].

This co-localization index is a measure of similarity of spatial distributions. Since our experiment aims to demonstrate that interacting proteins (such as PHPF) co-localize while non-interacting (such as PHPaaC) don't, we decided to use this parameter to see if there was a difference in the mean values of the co-localization indexes in the two samples.

Moreover, we also used the co-localization index to identify co-localizing pairs of molecules. This was done by calculating the $CI$ for all the localizations of the two channels and then discarding those with $CI = 0$. A co-localization index equal to zero means that there's no particle around, while, if it's greater than zero, it means that there's at least one particle nearby. By excluding localizations with $CI = 0$, we retain only those with at least one particle nearby and, by performing a nearest neighbor search, we can find the closest one and measure the distance between them.

## 3.6 Results

My analysis procedure was applied to both simulated and real data. Simulations were performed using the *MATLAB* software *Single-Molecule Imaging Simulator* (SMIS) [153]. SMIS is a software specifically developed for simulating SMLM experiments with fluorophores exhibiting different spectral and photophysical proprieties. For my study, I performed the simulations considering two photoactivable fluorescent proteins with the same spectra of PAGFP and PAmCherry1 and similar photoswitching properties. As positive control sample (interacting proteins as PHPF) I simulated co-localizing proteins with a mean distance of $(10 \pm 5)$ nm, while as negative control (non-interacting proteins as PHPaaC) I simulated randomly distributed proteins. Moreover, to make the simulations
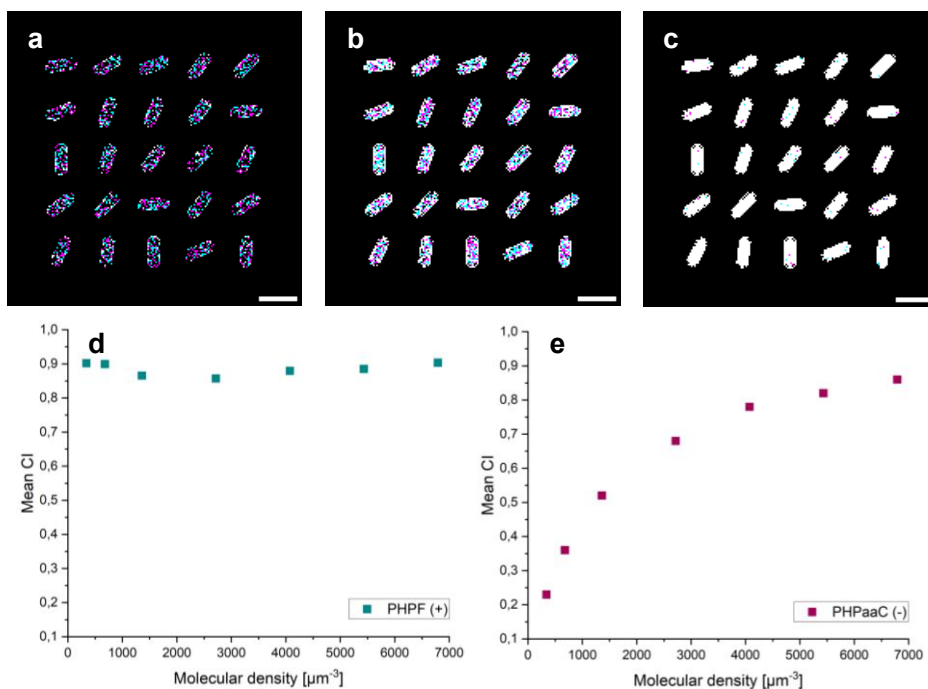


**Figure 3.8:** Relation between molecular density of fluorophores and co-localization analysis. **(a, b, c)** Simulations of randomly distributed PAGFP (cyan) and PAmCherry1 (magenta) in E. Coli bacteria with increasing molecular density (from 340 to 6800 molecules/μm³); **(d, e)** Mean CIs with respect to the average molecular density for co-localizing (cyan, left) and randomly distributed (magenta, right) fluorescent proteins. The higher is the molecular density of the fluorophores, the harder it becomes to distinguish the random distributions from the co-localizing ones. Scalebar: 2 μm.

more reliable, I also took into account the average number of localizations per bacterium (about 2000), corresponding to a molecular density of about 6800 molecules/$\mu$m$^3$. This is because a higher molecular density increases the probability of having false positives, meaning co-localizations that are not real but are merely due to spatial constraints within the bacterium. In fact, since co-localization occurs for molecules within a specific distance from the selected one, the higher is the molecular density, the closer will be the molecule inside the bacteria and thus co-localization will occur even for molecules randomly distributed. This is clearly shown in **Figure 3.8**, as for low molecular densities (such as 340 molecules/$\mu$m$^3$) the mean CIs for co-localizing molecules and randomly distributed proteins are very different, while for high molecular densities (such as 6800 molecules/$\mu$m$^3$) this difference is much smaller.

### 3.6.1 Simulated data

Through my analysis procedure I extracted from each measurement the following values: the mean co-localization index, the percentage of co-localizing molecules (i.e. molecules with CI > 0) and the distance between them. As seen in the previous section, the CI can be defined for each channel of the acquisition. However, for the sake of clarity, only the CI of the PAGFP channel is reported here.

**Figure 3.9** reports the mean CIs of PAGFP obtained from the analysis of 20 simulations of positive (PHPF, N=10) and negative (PHPaaC, N=10) control samples. Since the CIs were normally distributed, I performed a two-sample t-test and found that negative control CIs were significantly lower than positive control ones (p<0.0001). This is consistent with what is expected as the CI measures the similarity of spatial distributions and thus this parameter can distinguish between molecules randomly and non-randomly distributed even for high molecular densities.
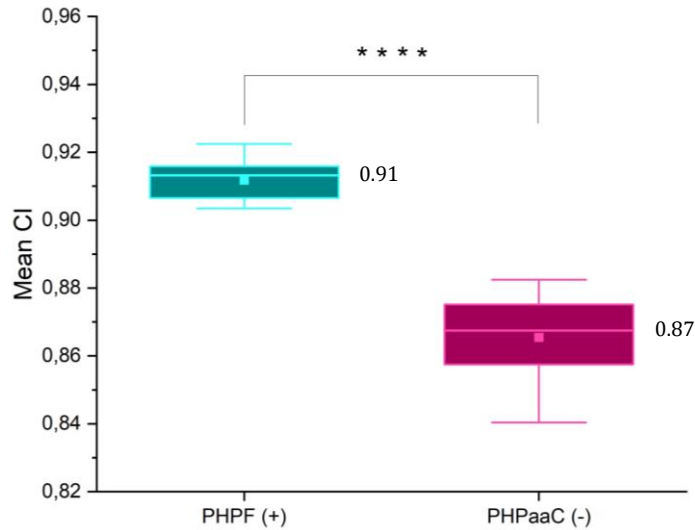
**Figure 3.9:** Box plots displaying the mean CIs of PAGFP derived from the analysis of 20 simulations of positive (PHPF, N=10, cyan box plot) and negative (PHPaaC, N=10, magenta box plot) control samples. The line and the square in each box are respectively the median and mean value. For the median is also reported its numerical value. ****: p<0.0001 two-sample t-test.

In **Figure 3.10** are reported the percentages of co-localizing molecules obtained from the 20 simulations. In this case, since the distributions of the negative control wasn't gaussian, I couldn't perform the two-sample t-test. However, by observing the plot, we can see that the positive control has only a slightly higher percentage of co-localizing molecules (about 1%). This is also consistent with what expected as the high molecular density of the fluorophores leads to many false positive co-localizations to occur and, as a consequence, the percentage of co-localizing molecules ends up being almost the same in both samples.

Finally, I also studied the mean distance between co-localizing pairs of molecules. To do that, for the localizations with $CI > 0$ I performed a nearest-neighbor search to find the closest molecule and then measure the distance between them. From the analysis of each simulation, I estimated the mean distance and its error. The error for each distance ($\Delta d$) was calculated with the propagation of error as:
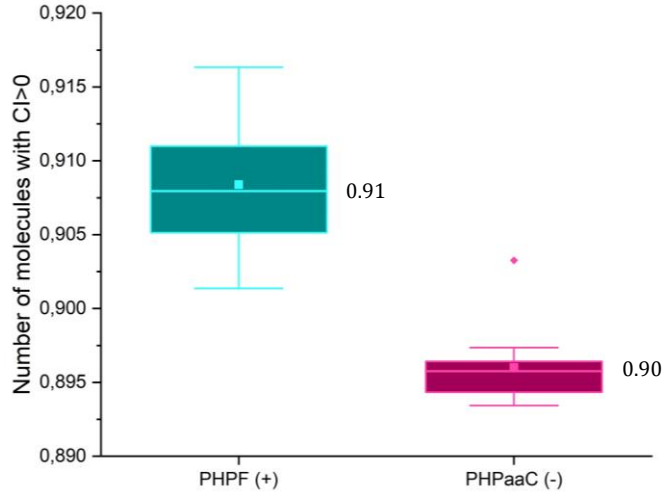
**Figure 3.10:** Box plots displaying the percentage of co-localizing molecules of PAGFP derived from the analysis of 20 simulations of positive (PHPF, N=10, cyan box plot) and negative (PHPaaC, N=10, magenta box plot) control samples. The line and the square in each box are respectively the median and the mean value while the point outside of the box is an outlier. For the median is also reported its numerical value.

$$\Delta d = \frac{|x_b - x_g| \cdot (\Delta x_b' + \Delta x_g) + |y_b - y_g| \cdot (\Delta y_b' + \Delta y_g)}{\sqrt{(x_b - x_g)^2 + (y_b - y_g)^2}} \quad (3.3)$$

With

$$\Delta x_b' = \sqrt{\Delta x_b{}^2 + FRE_x{}^2} \, , \Delta y_b' = \sqrt{\Delta y_b{}^2 + FRE_y{}^2} \quad (3.4)$$

Where $x_b, y_b, x_g, y_g$ are the coordinates of the pairs of co-localizing molecules and $\Delta x_b, \Delta y_b, \Delta x_g, \Delta y_g$ are the localization errors reported in section 2.4.3 taking also into account the FRE for mapping the blue channel into the green one to correct for chromatic aberrations.

In **Figure 3.11** are reported the mean distances obtained from the 20 simulations. The values of the negative control are slightly higher than the positive ones (only 0.3 nm), meaning that molecules randomly distributed are a bit more distant than co-localizing ones. However, considering that the error associated to the distance, calculated as the mean value of the errors obtained from each simulation, is about 10.7 nm, it can be concluded that there is no significant difference. This is

**Figure 3.11**: Box plots displaying the mean distance between the co-localizing pairs of molecules derived from the analysis of 20 simulations of positive (PHPF, N=10, cyan box plot) and negative (PHPaaC, N=10, magenta box plot) control samples. The line and the square in each box are respectively the median and the mean value while the point outside of the box is an outlier. For the median is also reported its numerical value.
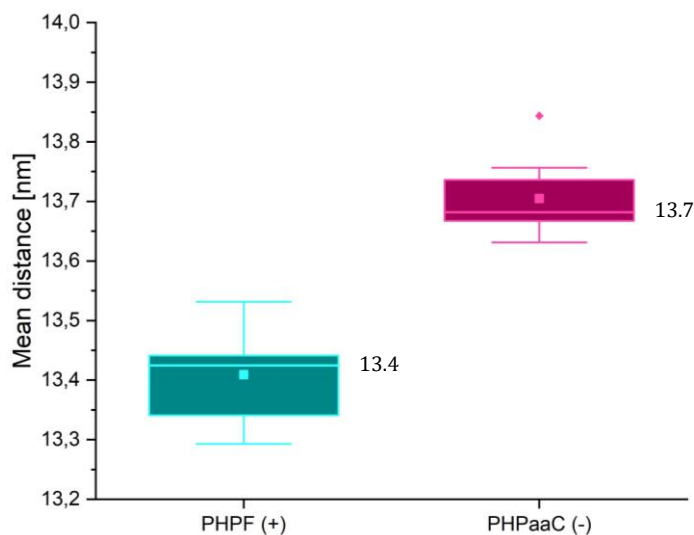
reasonable as in my simulations co-localizing pairs of molecules are identified by performing a nearest-neighbor search within 20 nanometers. In the negative control, molecules are randomly distributed, but, due to the high molecular density, many false positive occur (as demonstrated from the percentage of co-localizing molecules) and for co-localization to occur molecules must be closer than 20 nm.

The results of the parameters (CI and percentage of co-localizing molecules) obtained from the co-localization analysis on simulated data are reported in **Table 3.1**.

|  | Co-localization Index (CI) | Percentage of molecules with CI>0 |
|---|---|---|
| **PHPF (+)** | $0.913 \pm 0.006$ | $0.908 \pm 0.004$ |
| **PHPaaC (-)** | $0.867 \pm 0.013$ | $0.896 \pm 0.003$ |

**Table 3.1:** Results of the co-localization analysis of simulated data. For each parameter is reported the median and the standard deviation.

## 3.6.2 Real data
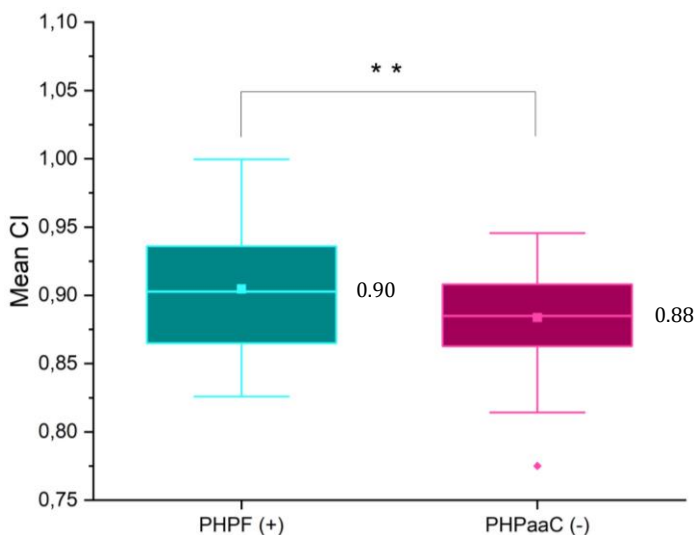


**Figure 3.12:** Box plots displaying the mean CIs of PAGFP derived from the analysis of 120 acquisitions of positive (PHPF, N=60, cyan box plot) and negative (PHPaaC, N=60, magenta box plot) control samples. The line and the square in each box are the median and mean value respectively, while the points outside of the box are the outliers. For the median is also reported its numerical value. **: p<0.01 two-sample t-test.

**Figure 3.12** reports the mean CIs obtained from the analysis of 120 acquisitions of positive (PHPF, N=60) and negative (PHPaaC, N=60) control samples. By comparing positive and negative control results, consistently with simulated data, negative control CIs are significantly lower than positive ones (p<0.01 two-sample t-test)[5]. However, with respect to simulated data, real data show a higher variability (i.e. higher standard deviation). This increased variability could be attributed to the number of activated molecules. In a real acquisition, not all molecules are activated. In fact, although I optimized the acquisition parameters to obtain sufficient localizations for both proteins, these parameters still represent a compromise between the requirements of each protein. The necessity to select an intermediate value for the activation laser power and the exposure time leads to the activation of a different number of fluorophores and the loss of some

---

[5] Due to the high molecular density of our sample (of about 6800 molecules/$\mu m^3$), as shown in **Figure 3.8**, consistently with the simulations, the difference between the mean CIs couldn't be greater than 0.02-0.03.
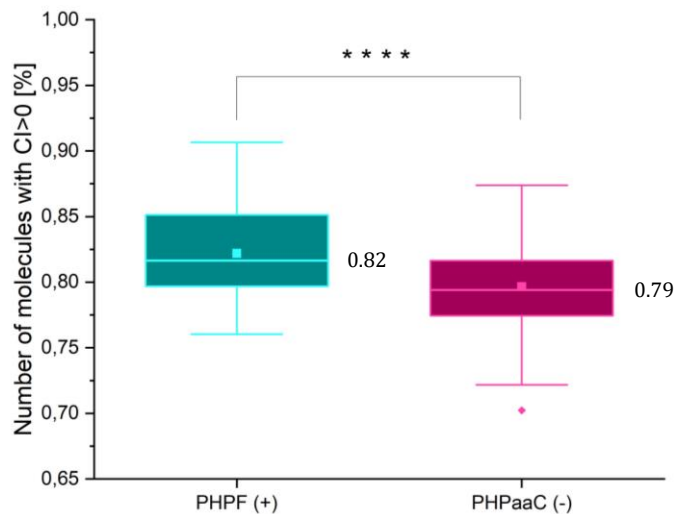
**Figure 3.13:** Box plots displaying the percentage of co-localizing molecules of PAGFP derived from the analysis of 120 acquisitions of positive (PHPF, N=60, cyan box plot) and negative (PHPaaC, N=60, magenta box plot) control samples. The line and the square in each box are the median and mean value respectively, while the point outside of the box is an outlier. For the median is also reported its numerical value. ****: p<0.0001 two-sample t-test.

localizations. If the lost localizations belong to both proteins of the same pair of interacting proteins, this loss won't significantly impact the co-localization analysis. However, if the loss of localizations occurs for only one protein of the pair, it will lead to a non-colocalization event, thus decreasing the overall CI of the acquisition. Since photoactivation is a stochastic process, the loss of localizations will affect each acquisition differently, depending on the molecules activated during that acquisition, thus introducing a variability in the results.

As for simulated data, I also studied the percentage of co-localizing molecules (**Figure 3.13**). In agreement with simulations results, the percentage of co-localizing molecules is higher in the positive control compared to the negative one. In this case, I could also perform the two-sample t-test and I found a significant difference (p<0.0001) between positive and negative control. Moreover, as for the CI analysis, there's a higher variability (i.e. a higher standard deviation) of the real data compared to the simulated ones and, as for the CIs,
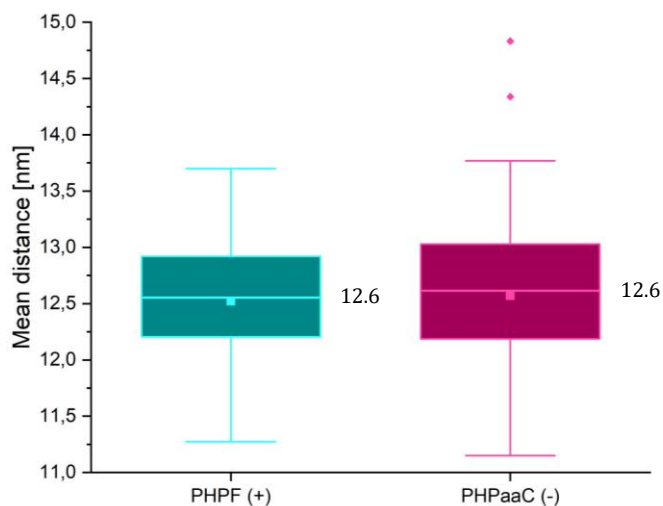
**Figure 3.14:** Box plots displaying the mean distance between the co-localizing pairs of molecules derived from the analysis of 120 acquisitions of positive (PHPF, N=60, cyan box plot) and negative (PHPaaC, N=60, magenta box plot) control samples. The line and the square in each box are the median and mean value respectively, while the points outside of the box are the outliers. For the median is also reported its numerical value.

this could be related to the number of activated/non-activated molecules in each acquisition.

Finally, in **Figure 3.14** are reported the mean distances obtained from the analysis of the 120 acquisitions of real data. The estimated distance $(12.6 \pm 10.7)$ nm is consistent both with the simulations and with that of an intermolecular distance. Moreover, as for simulated data, as expected, there is no significant difference between the two samples.

The results of the parameters (CI and percentage of co-localizing molecules) obtained from the co-localization analysis on real data are reported in **Table 3.2**.

|  | Co-localization Index (CI) | Percentage of molecules with CI>0 |
|---|---|---|
| **PHPF (+)** | $0.90 \pm 0.04$ | $0.82 \pm 0.04$ |
| **PHPaaC (-)** | $0.88 \pm 0.03$ | $0.79 \pm 0.03$ |

**Table 3.2:** Results of the co-localization analysis of real data. For each parameter is reported the median and the standard deviation.

## 3.7 Limitations of the technique

I developed an acquisition and an analysis procedure to study the subcellular organization of biological samples and get quantitative results. By comparing simulated and real data results I assessed the reliability of my analysis, by verifying that the method can quantify a significant difference between co-localizing and non-colocalizing distributions of molecules.

However, to obtain more insights on bacterial subcellular organization it is necessary to further increase the resolution of the system. In fact, although the analysis can distinguish between two-dimensional random and non-random distributions even for samples with high molecular densities, it cannot measure distances below 10 nm. This limit is set by the localization errors along the xy axis and by the registration error (FRE) due to the chromatic aberrations' correction. Moreover, the high molecular density of the sample prevents three-dimensional imaging as the PSFs of the emitters overlap and they become undistinguishable.

One possibility to overcome these limitations could be to combine single-molecule imaging with a technique known as *Expansion Microscopy* (ExM). ExM enables the physical isotropic expansion of the sample by of a factor of about 4-4.5 [154] leading to an increase of the resolution of the system by the same amount. As a consequence, by expanding the samples, we could achieve the resolution required to measure distance below 10 nm and, since the molecular density would decrease by a factor of about 64, we could also perform three-dimensional imaging.

# Chapter 4

# Expansion-PALM microscopy (Ex-PALM)

Super-resolution techniques have revolutionized microscopy, enabling researchers to overcome the diffraction limit and achieve resolutions beyond what was previously thought possible. The development of these techniques has significantly advanced the understanding of several biological structures at the nanoscale level. In the first chapter of this thesis, we have seen how most super-resolution techniques break the diffraction limit which is by either temporally or spatially modulating the excitation/activation of light. However, in recent years, another technique has been developed that surpasses the diffraction limit with a completely different approach. This technique, known as *Expansion Microscopy* (ExM), exploits a chemical treatment to produce a physical isotropic expansion of the sample (by about 4-4.5 times), thus leading to an increase of the resolution of the system by the same amount of the expansion factor. Therefore, ExM achieves super-resolution imaging, with diffraction-limited microscopes, such as traditional confocal microscopes.

In the previous chapter I showed how I used multicolour PALM to study the subcellular organization of bacteria, and how to the high molecular density of fluorophores in the small volume of bacteria didn't allow to achieve nanometer resolution three-dimensional imaging and measure distances below 10 nm. One solution to decrease the molecular density, thus recovering the possibility to localize molecules through fitting of the astigmatic PSF, could be the combination of PALM imaging with the ExM treatment of the sample.

In this chapter, after a brief introduction on the principle of ExM, I will show how I optimized the expansion treatment for my samples and then how to perform and analyze Expansion-PALM (Ex-PALM) microscopy acquisitions. Finally, I will compare Ex-PALM results with the previous ones to check consistencies and differences.

## 4.1 Expansion Microscopy (ExM)

Microscopy has played a crucial role in discovering and understanding several biological processes by optically magnifying images of structures in fixed cells and tissues. However, in 2015, Chen et al. demonstrated that a physical magnification of the sample, with negligible distortion, was possible as well. By embedding the sample in a polyelectrolyte gel, they obtained a 4.5-fold isotropic expansion of the sample thus enabling 70 nm resolution imaging with a standard confocal microscope [154].

Expansion original protocol consisted of the four steps reported in **Figure 4.1a**. First the biomolecules of interest were stained with polymer-linkable probes (see **Figure 4.1b**) consisting of antibodies
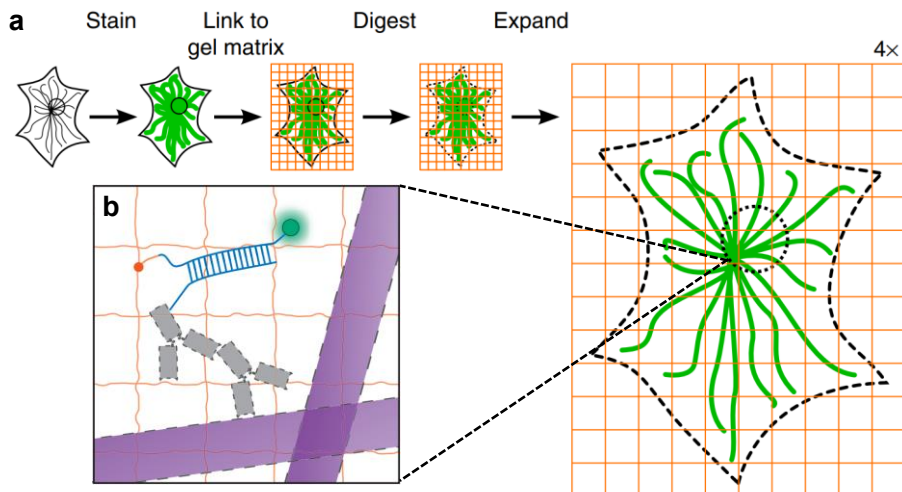


**Figure 4.1: (a)** Main steps of the original ExM protocol: 1) *staining* of the specimen with gel-anchorable fluorophores, 2) growth of a swellable polymer within the specimen that links to the probes (*gelation*), 3) protease *digestion* to homogenize its mechanical properties and 4) *expansion* through dialysis in water; **(b)** Custom-made polymer linkable probes consisting of DNA-labeled antibodies. Images retrieved from [154], [155].

labeled with doubly modified DNA oligonucleotides that contained a fluorophore and a methacryloyl group and were designed to covalently attach to the polymer. Then, a swellable polyelectrolyte gel was synthesized in the sample to incorporate the labels. After that, the sample was treated with a nonspecific protease to homogenize its mechanical properties and, finally, dialysis in water mediated the uniform physical expansion of the polymer-specimen composite.

This was a novel approach as it enabled super-resolution imaging with diffraction-limited microscopes, but the use of custom-made probes initially limited accessibility to this technique for many researchers. However, during the years, many alternative ExM protocols have been developed using conventional antibodies and fluorescent proteins as probes [155], [156], thus making it more accessible to a broader group of researchers. Among these, *protein-retention Expansion Microscopy* (proExM) anchors proteins to the swellable gel, enabling the use of conventional fluorescently labeled antibodies and streptavidin, and fluorescent proteins.

## 4.2 Optimization of the expansion protocol for E. Coli bacteria

To find the best protocol for expanding bacteria I started by trying to perform expansion with already existing protocols. I found two protocols [157], [158], based on proExM, where bacteria were expanded. Unfortunately, none of these protocols worked for my sample, so I had to develop my own, which required many months of try and fail to finally find the one working best for our experimental conditions. The final protocol I developed and thoroughly validated is reported in section 6.4.3. Crucial steps in the optimization of the protocol were:

1) Finding the right concentration of mutanolysin which is used to digest the cell wall of bacteria. A complete digestion of the cell wall is crucial to obtain uniform expansion.

2) Determining the optimal concentration of Methacrylic Acid N-HydroxySuccinimide ester (MA-NHS) which is used to anchor proteins to the gel. If its concentration is too low, only few proteins will be retained in the gel and this will result in poor imaging; while if the concentration is too high the gel will be more rigid and expand less and unevenly.

3) Optimizing the digestion duration. In fact, the digestion timing is strictly related to the number of proteins which remain attached to the gel. Since I had to increase the concentration of MA-NHS, I also had to adjust the digestion duration in order to achieve a uniform expansion of the sample. The sample must be completely digested to achieve an isotropic expansion and avoid the rupture of bacteria and the dispersion of chromophores in the gel that will introduce unwanted background signal during the measurement.

The success of the expansion treatment is strictly related not only to the biological sample itself (whether it is a tissue, a single eucaryotic cell or a single procaryotic cell), but also to the type of fluorescent probes used to label the proteins of interest. When using fluorescent proteins, each of them responds differently to the treatments and this is why protocols must be adjusted according to each specific experimental condition. By adjusting all the parameters described above, I could finally perform expansion on E. Coli bacteria for dual color imaging with PAGFP and PAmCherry1.
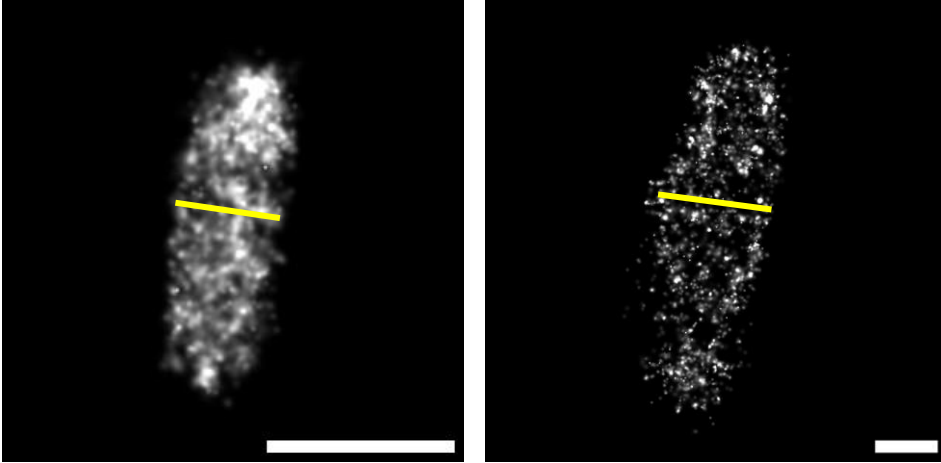
## 4.3  Measure

To perform Ex-PALM imaging, I prepared a sample with fixed expanded bacteria embedded in a polyelectrolyte gel as described in section 6.4.3. As already explained, since the fine correction of chromatic aberrations is crucial for obtaining reliable results, as I did for multicolour PALM imaging, before each set of acquisitions I also

prepared a sample with fluorescent beads and scanned the field of view (as described in section 6.5.1) using a scanning step size of the piezo-electric stage of 600 nm which corresponds to the lowest registration error (as demonstrated in section 2.4.1). The detailed imaging protocol for Ex-PALM of E. Coli with all the acquisition parameters can be found in section 6.5.3. Briefly, first, I partially closed the slit placed in the excitation path after the circular iris (see **Figure 2.11**) to reduce the thickness of the HILO beam up to about 4 µm thickness and increase the signal to noise ratio [159]. In fact, by reducing the beam thickness a thinner slice of the sample is excited, thus leading to a decrease in background signal from out-of-focus light and, consequently, an increase in the signal to noise ratio. Then, since the expanded bacteria are transparent (as the expanded material is >99% water), brightfield microscopy couldn't be used to select the region of interest, as was done in multicolour PALM, so I had to turn on all the lasers simultaneously to find the plane where bacteria were placed. In most cases bacteria lied at about 3-4 µm from the coverslip surface. For this reason, our custom inclined illumination geometry, with highly confined excitation volume, revealed to be fundamental to achieve single molecule sensitivity. Once the plane was identified, the illuminated field of view was changed, as most fluorophores in the current view were already bleached, and the acquisition was started with the same parameters used for "standard" multicolor PALM. It should be noticed that, since expansion treatment reduces the intensity and the number of fluorophores, Ex-PALM acquisitions are shorter compared to PALM acquisitions and PAGFP crosstalk is no longer detectable.

## 4.4   Analysis

Analysis of Ex-PALM acquisitions mainly consists of two steps: estimating the expansion factor and performing multicolour analysis (without crosstalk correction), as described in section 3.5.

**Figure 4.2:** Measure of the average width of unexpanded (left) and expanded (right) bacteria. Scalebar: 1 µm.

The expansion factor (EF) was calculated (as shown in **Figure 4.2**) by measuring the average width of bacteria pre and post expansion. The width can be measured precisely regardless the cellular orientation in three dimensions [157], [160]. From the measure of 30 bacteria ($N_{unexp} = 10$, $N_{expPHPF} = 10$, $N_{expPHPaaC} = 10$) I obtained an average expansion factor of 3.97 $\pm$ 0.57 for PHPF and of 3.86 $\pm$ 0.57 for PHPaaC.

For 2D acquisitions the multicolour analysis was performed exactly as described in section 3.5, but without the crosstalk correction because, due to expansion treatment, the intensity of PAGFP decreased and crosstalk was no longer detectable. For 3D acquisitions, the analysis was performed as it follows:

1) Localization of single molecules with ThunderSTORM using the parameters reported in **Figure 4.3** and the cubic calibration curves reported in section 6.2. In this step I also corrected for the axial shift between focal planes due to axial chromatic aberration as explained in section 6.2.

2) Correction of lateral chromatic aberration using the algorithm explained in section 2.4.1 as for 2D acquisitions.
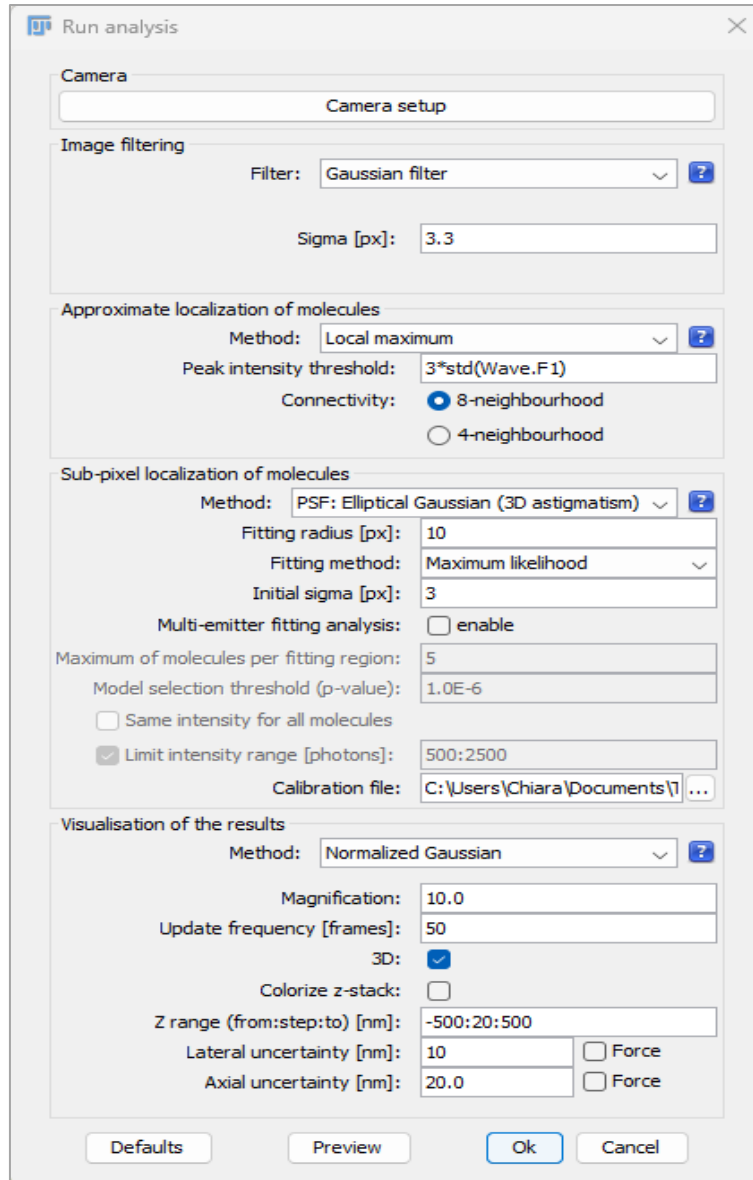
**Figure 4.3:** ThunderSTORM user interface showing the parameters used to find the xyz sub-pixel positions of single molecules of PAGFP and PAmCherry1 in bacteria.

3) Merging of the reappearing molecules as for 2D acquisitions but in this case the nearest neighbor search to identify molecules as duplicates was performed in a wider range (about 40 nm for PAmCherry1 localizations, about 50 nm for PAGFP

localizations[6]) as the mean localization uncertainties are higher. Once duplicates were identified, as in the 2D case, they were combined into a new molecule whose position $(x_m, y_m, z_m)$ was calculated from the coordinates of the individual duplicates as intensity-weighted average as follows [143]:

$$x_m = \frac{\sum_{i=1}^{N\,duplicates} x_i I_i}{\sum_{i=0}^{N\,duplicates} I_i} \tag{4.1a}$$

$$y_m = \frac{\sum_{i=1}^{N\,duplicates} y_i I_i}{\sum_{i=0}^{N\,duplicates} I_i} \tag{4.1b}$$

$$z_m = \frac{\sum_{i=1}^{N\,duplicates} z_i I_i}{\sum_{i=0}^{N\,duplicates} I_i} \tag{4.1c}$$

Where $x_i$, $y_i$, $z_i$ and $I_i$ represent the x,y,z coordinates and the intensity of each duplicate, respectively. Regarding the localization uncertainty, I computed the standard deviation of duplicate positions along the three axis and then selected the maximum value between them.

4) Co-localization analysis with a similar algorithm used for the 2D acquisitions but with a wider range to identify the co-localizing pairs of molecules (about 40 nm for PAmCherry1 localizations, about 50 nm for PAGFP localizations).

## 4.5 Results

In this section are reported the results of co-localization analysis of 2D and 3D Ex-PALM acquisitions. As for PALM imaging, from the analysis of each acquisition I retrieved: the mean co-localization index,

---

[6] The localization uncertainty is higher for PAGFP with respect to PAmCherry1 because PAGFP intensity was affected more from the expansion treatment than PAmCherry1 and this causes the localization uncertainty to increase.

the percentage of co-localizing molecules (i.e. molecules with CI > 0) and the distance between them.

### 4.5.1 2D Ex-PALM

In **Figure 4.4** is reported the reconstructed image obtained from a 2D Ex-PALM acquisition. As it can be seen from the image, PAGFP was more affected by the expansion treatment, and this resulted in a lower number of localizations compared to PAmCherry1.
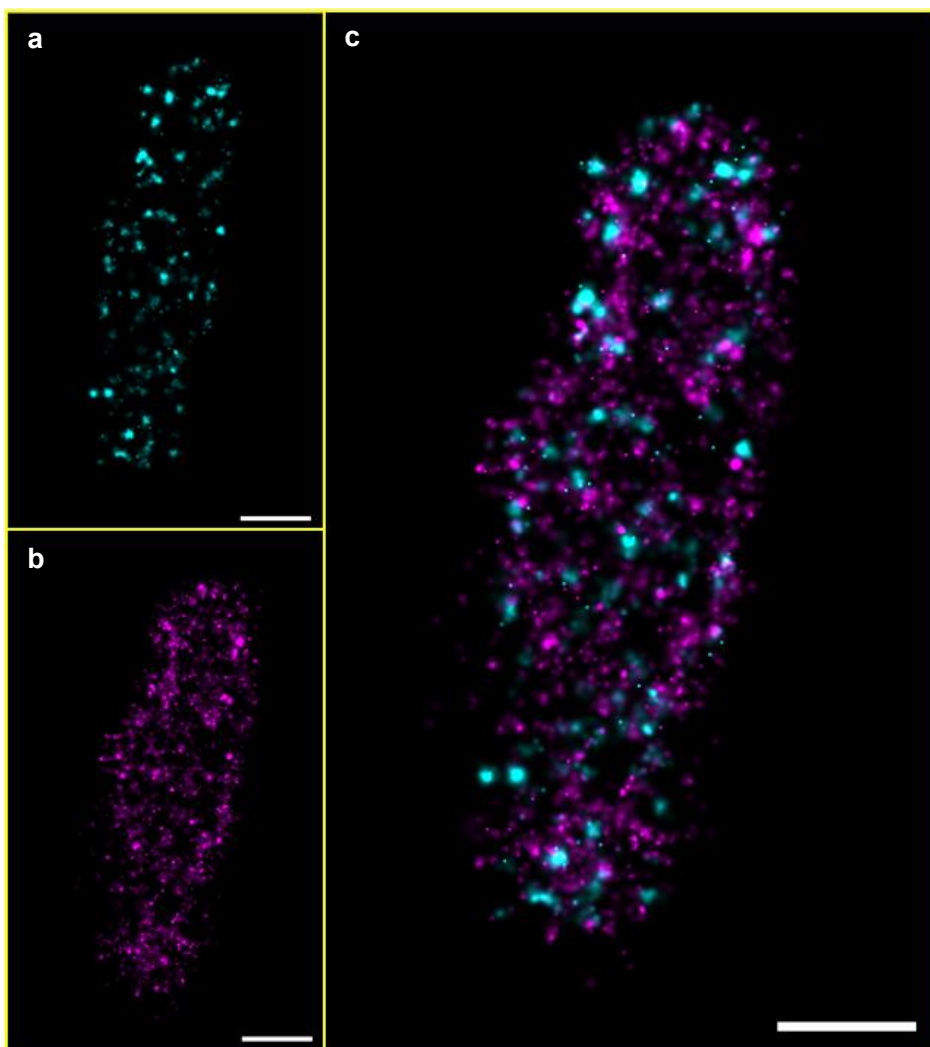


**Figure 4.4:** Image of an expanded E. Coli bacteria (PHPF) reconstructed from a 2D Ex-PALM acquisition. **(a)** Cyan channel, PAGFP localizations; **(b)** Magenta channel, PAmCherry1 localizations; **(c)** Merging of the channels. Scalebar: 1 μm.
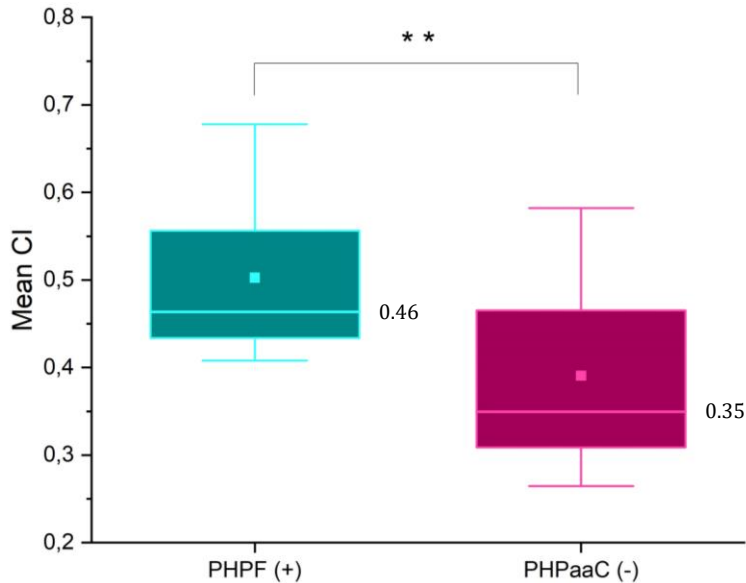
**Figure 4.5:** Box plots displaying the mean CIs of PAGFP derived from the analysis of 20 acquisitions of positive (PHPF, N=10, cyan box plot) and negative (PHPaaC, N=10, magenta box plot) control samples. The line and the square in each box are the median and mean value respectively. For the median is also reported its numerical value. **: p<0.01 two-sample t-test.

**Figure 4.5** reports the mean CIs of PAGFP obtained from the analysis of 20 acquisitions of positive (PHPF, N=10) and negative (PHPaaC, N=10) control samples of expanded bacteria. Since the CIs were normally distributed, I performed a two-sample t-test and found that negative control CIs were significantly lower than positive control ones (p<0.01). This is consistent with previous results. However, with respect to PALM acquisitions, the average values of the CI are lower. These lower values are probably related to the number of fluorophores that survived to the expansion treatment. In my acquisitions I found that PAGFP was more affected by the expansion treatment compared to PAmCherry1.

Then, as for PALM acquisitions, I also studied the percentage of co-localizing molecules (**Figure 4.6**). As for the CIs, the average number of co-localizing molecules is lower compared to PALM acquisitions values because of the loss of proteins due to the expansion treatment. However, in agreement with previous results, the percentage of co-
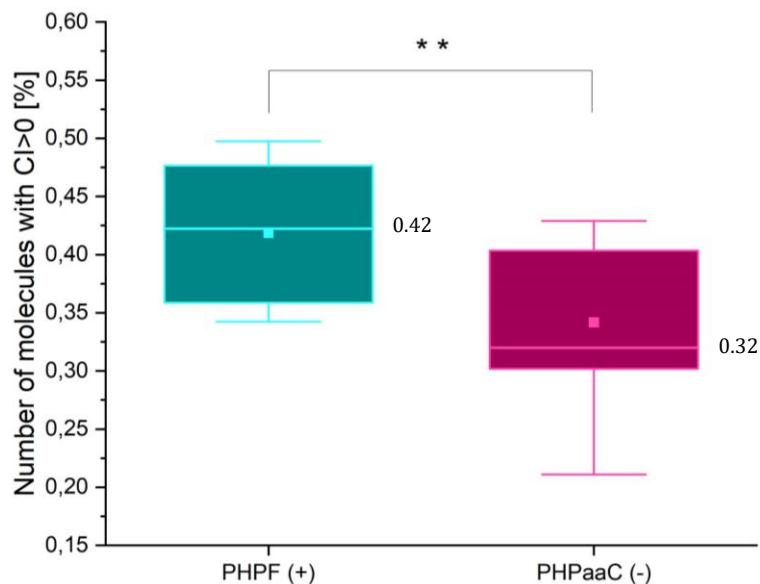
**Figure 4.6:** Box plots displaying the percentage of co-localizing molecules of PAGFP derived from the analysis of 20 acquisitions of positive (PHPF, N=10, cyan box plot) and negative (PHPaaC, N=10, magenta box plot) control samples. The line and the square in each box are the median and mean value respectively. For the median is also reported its numerical value. **: p<0.01 two-sample t-test.

localizing molecules is significantly higher (p<0.01) in the positive control compared to the negative one.

Finally, in **Figure 4.7** are reported the mean distances obtained from the analysis of the 20 acquisitions of expanded bacteria. For each sample the average distance was calculated by dividing the distance retrieved from the co-localization analysis by the respective expansion factor (3.97 for PHPF, 3.86 for PHPaaC). For PHPF I found an average distance of (6.8 ± 2.7) nm, while for PHPaaC I found an average distance of (9.2 ± 2.8) nm. These values are consistent with the previous results and, as expected, by combining ExM treatment with PALM imaging process I achieved a higher resolution that allowed me to measure distances below 10 nm. This time the error $\Delta d$ on the distance was estimated as it follows. First, as for PALM acquisitions, I propagated the error to find the error on the distance of each pair of co-localizing molecules (equation 3.3, section 3.6.1). From each acquisition I extracted the mean value and, by considering all the
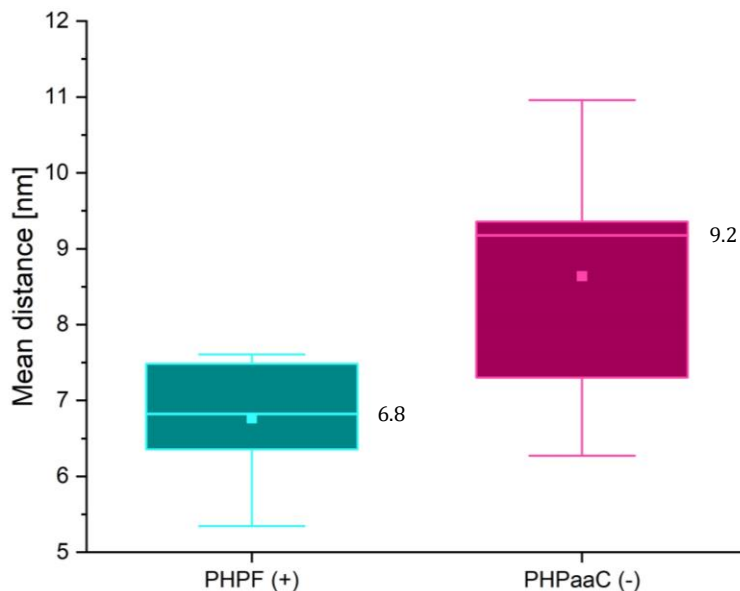
**Figure 4.7:** Box plots displaying the mean distance between the co-localizing pairs of molecules derived from the analysis of 20 acquisitions of positive (PHPF, N=10, cyan box plot) and negative (PHPaaC, N=10, magenta box plot) control samples. The line and the square in each box are the median and mean value respectively. For the median is also reported its numerical value.

acquisitions, I obtained an error of about 10.8 nm for both samples. Then, since the expansion factors were 3.97 for PHPF and 3.86 for PHPaaC, I divided the error for the expansion factors and obtained a final error of 2.7 nm for PHPF and 2.8 nm for PHPaaC.

The results of the parameters (CI and percentage of co-localizing molecules) obtained from the co-localization analysis of 2D Ex-PALM are reported in **Table 4.1.**

|  | Co-localization Index (CI) | Percentage of molecules with CI>0 |
|---|---|---|
| **PHPF (+)** | 0.46 ± 0.08 | 0.42 ± 0.06 |
| **PHPaaC (-)** | 0.35 ± 0.12 | 0.32 ± 0.07 |

**Table 4.1:** Results of the co-localization analysis of 2D expanded bacteria. For each parameter is reported the median and the standard deviation.

## 4.5.2 3D Ex-PALM

As demonstrated in section 4.4, the ExM treatment produced an isotropic expansion of the bacteria of about 4 times in each dimension, leading to a significant increase in volume, approximately 64 times larger than that of unexpanded bacteria. As a consequence, the molecular density decreased by the same amount, and this enabled us to perform three-dimensional imaging with nanometers accuracy. In **Figure 4.8** is reported the reconstructed image of an expanded bacteria acquired with 3D Ex-PALM.

In **Figure 4.9** are reported the mean CIs of PAGFP obtained from the analysis of 20 acquisitions of positive (PHPF, N=10) and negative (PHPaaC, N=10) control samples of expanded bacteria. In agreement
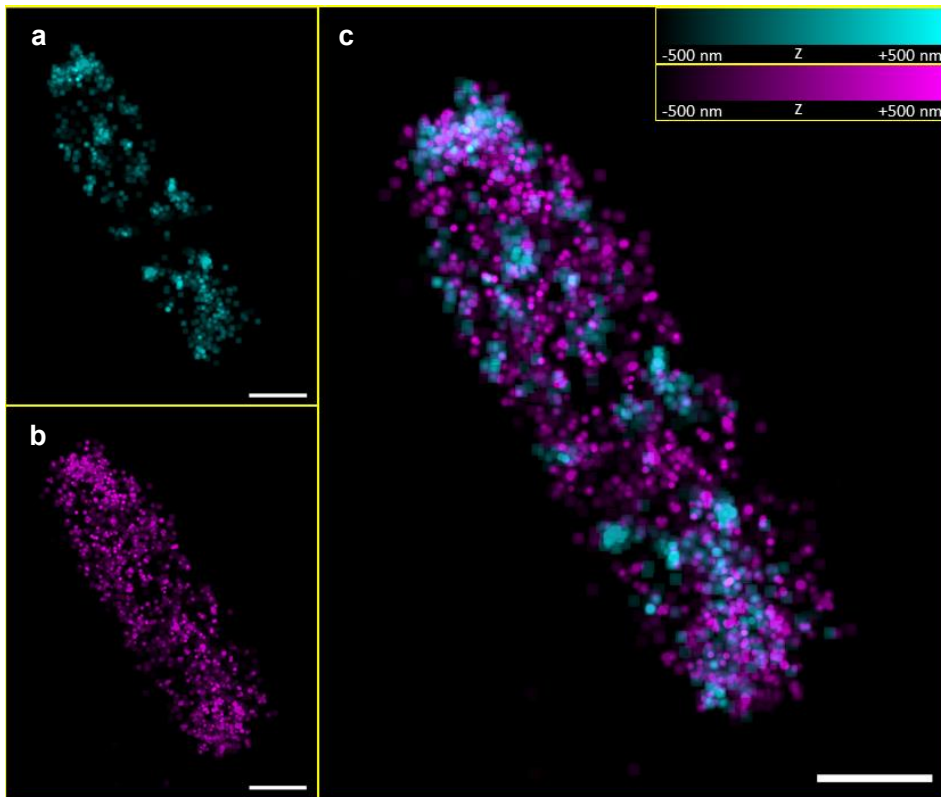


**Figure 4.8:** Image of an expanded E. Coli bacteria (PHPF) reconstructed from a 3D Ex-PALM acquisition. **(a)** Cyan channel, PAGFP localizations; **(b)** Magenta channel, PAmCherry1 localizations; **(c)** Merging of the channels. Scalebar: 1 μm.
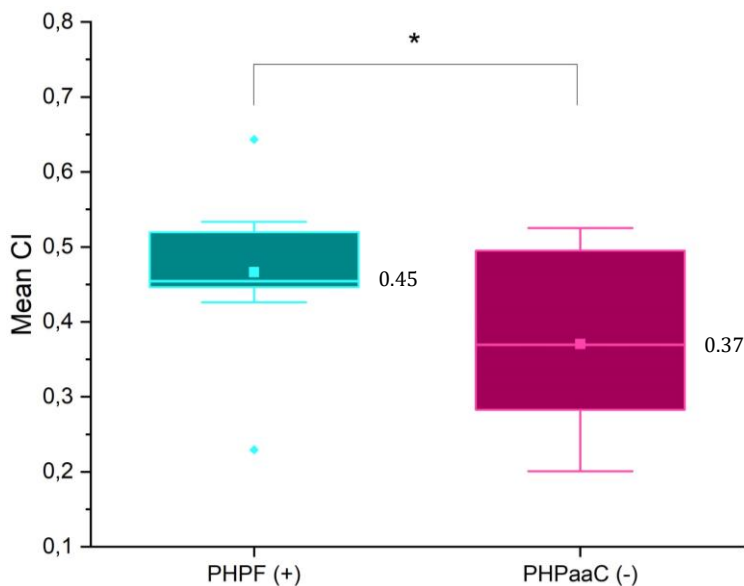
**Figure 4.9:** Box plots displaying the mean CIs of PAGFP derived from the analysis of 20 acquisitions of positive (PHPF, N=10, cyan box plot) and negative (PHPaaC, N=10, magenta box plot) control samples. The line and the square in each box are the median and mean value respectively, while the points outside of the box are the outliers. For the median is also reported its numerical value. *: $p < 0.05$ two-sample t-test.

with the previous results, CIs values of the positive control were significantly higher than those of the negative control ($p < 0.05$ two-sample t-test). Moreover, CI values retrieved from the analysis of 3D Ex-PALM acquisitions were consistent with those obtained from the analysis of 2D Ex-PALM acquisitions.

Then, as for previous measurements, I analyzed the percentage of co-localizing molecules (**Figure 4.10**). Even in this case, the number of co-localizing molecules was higher for the positive control with respect to negative one. Moreover, as for the CI values, the results were also consistent with those of 2D Ex-PALM acquisitions.

Finally, in **Figure 4.11**, I reported the 3D mean distances of co-localizing pairs of molecules in expanded bacteria. As for the 2D acquisitions, the average distance for each sample was calculated by dividing the distance retrieved from the co-localization analysis by the respective expansion factor. For PHPF I found an average distance of
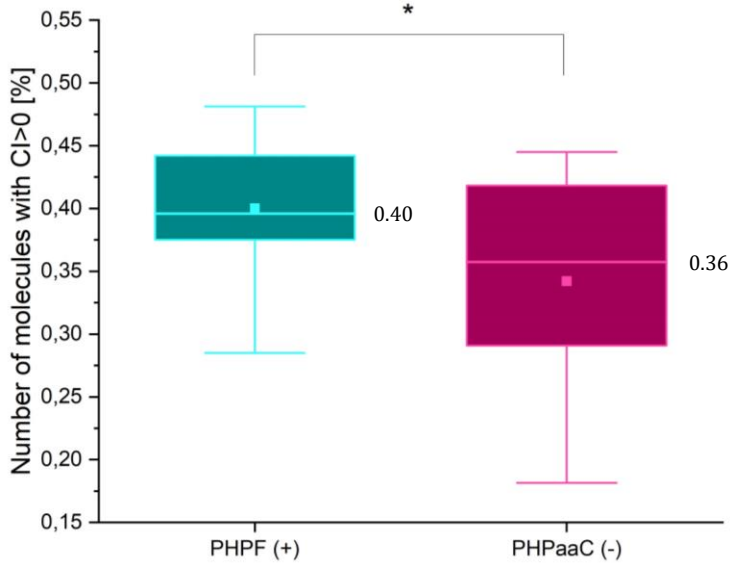
**Figure 4.10:** Box plots displaying the percentage of co-localizing molecules of PAGFP derived from the analysis of 20 acquisitions of positive (PHPF, N=10, cyan box plot) and negative (PHPaaC, N=10, magenta box plot) control samples. The line and the square in each box are the median and mean value respectively. For the median is also reported its numerical value. *: p<0.05 two-sample t-test.

$(19.3 \pm 5.6)$ nm, while for PHPaaC I found an average distance of $(19.6 \pm 5.8)$ nm. For the 3D acquisitions, the error on the distance was calculated as it follows. First, I estimated the error for each distance $(\Delta d)$ with the propagation of uncertainty as:

$$\Delta d = \frac{|x_b - x_g| \cdot (\Delta x_b' + \Delta x_g) + |y_b - y_g| \cdot (\Delta y_b' + \Delta y_g) + |z_b - z_g| \cdot (\Delta z_b + \Delta z_g)}{\sqrt{(x_b - x_g)^2 + (y_b - y_g)^2 + (z_b - z_g)^2}} \quad (4.2)$$

With

$$\Delta x_b' = \sqrt{\Delta x_b^2 + FRE_x^2} \,, \Delta y_b' = \sqrt{\Delta y_b^2 + FRE_y^2} \quad (4.3)$$

Where $x_b, y_b, x_g, y_g, z_b, z_g$ are the coordinates of the pairs of co-localizing molecules and $\Delta x_b, \Delta y_b, \Delta z_b, \Delta x_g, \Delta y_g, \Delta z_g$ are the localization errors reported in section 2.4.3 taking also into account the FRE for mapping the blue channel into the green one to correct for chromatic aberrations. Then, as for the 2D case, from each acquisition I retrieved a mean value of the error and, by considering all the acquisitions, I obtained an average error of 22.2 nm for both
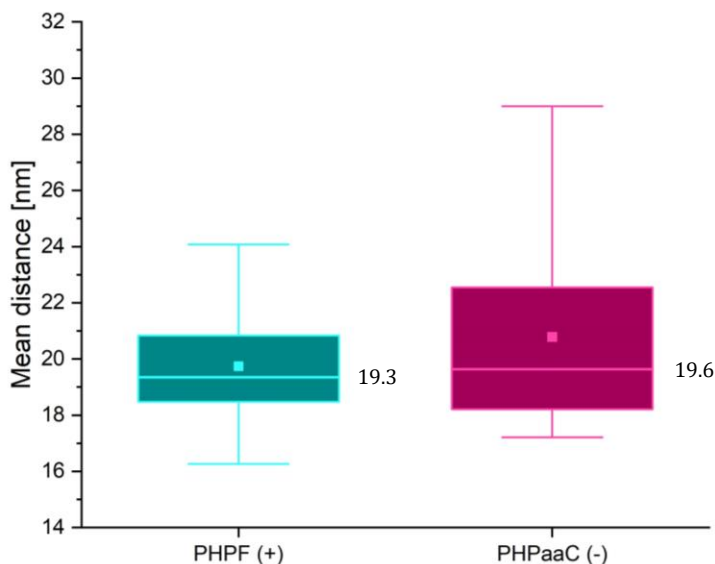
**Figure 4.11:** Box plots displaying the mean distance between the co-localizing pairs of molecules derived from the analysis of 20 acquisitions of positive (PHPF, N=10, cyan box plot) and negative (PHPaaC, N=10, magenta box plot) control samples. The line and the square in each box are the median and mean value respectively. For the median is also reported its numerical value.

PHPF and PHPaaC. Each value was divided by the respective expansion factor and, finally, I obtained a final error of 5.6 nm and 5.8 nm for PHPF and PHPaaC respectively. By comparing the average distances obtained in the 3D acquisitions with those obtained from the 2D acquisitions, it can be observed that the 3D distances are greater. This is reasonable, considering that bidimensional distances are projections of three-dimensional distances.

The results of the parameters (CI and percentage of co-localizing molecules) obtained from the co-localization analysis of 3D Ex-PALM are reported in **Table 4.2.**

|  | Co-localization Index (CI) | Percentage of molecules with CI>0 |
|---|---|---|
| **PHPF (+)** | $0.45 \pm 0.11$ | $0.40 \pm 0.05$ |
| **PHPaaC (-)** | $0.37 \pm 0.12$ | $0.36 \pm 0.09$ |

**Table 4.2:** Results of the co-localization analysis of 3D expanded bacteria. For each parameter is reported the median and the standard deviation.

## 4.6 Conclusions and future perspectives

I developed a biological protocol to isotropically expand E. Coli bacteria by a factor of about 4. By combining the expansion of bacteria with PALM imaging, I successfully performed 3D Ex-PALM microscopy and I succeeded in measuring distances below 10 nm with an error of few nm (about 2.8 nm in the 2D, about 5.8 nm in the 3D). The study successfully validated the method's capability to quantify differences in CIs and distances between positive and negative control samples using PALM, 2D, and 3D Ex-PALM.

Although the ExM protocol combined with PALM consistently reduced the minimum measurable distance, further optimization is needed to minimize protein loss. This could be achieved for example by adding more IPTG (inducer of gene transcription) in the culture medium to increase the transcription or by raising the concentration of MA-NHS to anchor a higher number of proteins to the gel. However, the latter option would also imply a longer digestion time, so to avoid lengthen the biological protocol too much a good compromise between the anchoring and the digestion should be found.

With our method robustly validated, the next steps will involve studying the spatial organization of native proteins to see if there's molecular compartmentalization inside bacteria as well as studying the distribution of genes to gain further understanding of the epigenetics of operons. For these purposes, an implementation of the analysis procedure will be required to achieve a better and more accurate comprehension of genes and proteins spatial distribution. With the new analysis we will be able, not only to measure the distance between pairs of molecule but also to perform a 3D mapping and, by introducing correlation functions, to identify clusters and analyze them. Moreover, these analyses will be performed at different times of the cell cycle to see if and how the subcellular organization of proteins and genes changes with the cell cycle.

To this end we are continuing our collaboration with the Microbiology group at the Biology Department of the University of Florence that will engineer the bacterial strains.

# Chapter 5

# Discussion

Super-resolution techniques have completely revolutionized the field of optical microscopy, enabling researchers to overcome the diffraction limit and achieve resolutions far beyond what was previously thought possible. With their technical capabilities and wide range of applications, these techniques have been pivotal in addressing several biological questions, including cell signaling, molecular dynamics and subcellular structures. Super-resolution techniques have become an indispensable tool in modern biological research, by providing insights that were once unattainable with traditional microscopy techniques. However, there are still some challenges to be faced. Currently, performing multicolour super-resolution imaging is not trivial. In fact, despite the availability of several commercial setups for multicolour super-resolution microscopy, achieving reliable results requires fine correction of all potential aberrations and artifacts that could significantly impact the outcomes. Performing multicolour super-resolution imaging is even more challenging in small volumes, such as bacteria, as the correction of the all the aberrations and artifacts must be at the nanoscale level.

In this thesis I described how I developed an optical system to perform three-dimensional multicolour super-resolution microscopy and then how I applied it to the study of molecular compartmentalization.

In the first part, after introducing the main technical difficulties of single-molecule multicolour imaging (i.e. mechanical and thermal drifts, chromatic aberrations and crosstalk), I demonstrated that through relatively simple algorithms it is possible to implement a SMLM setup to perform three-dimensional multicolour super-

resolution imaging with nanometers accuracy. Specifically, first, to minimize mechanical and thermal drifts, we developed an active stabilization system to control the position of the sample, estimate the drift and rapidly compensate for it in real time. Thanks to this feedback system we successfully achieved stable positioning of the sample, with a standard deviation of the position ranging from 5-7 nm for x,y-localization and 11.5 nm for z-localization. This ensures that even performing long time 3D single molecule experiments, such as 3D STORM acquisitions, the resolution is not compromised due to drifts. Then, to correct for chromatic aberrations, I developed an algorithm that, by using a non-rigid transformation function, maps all the points from one channel of the acquisition to the other with a registration error of only 3.5 nm. A fine correction of chromatic aberrations is crucial to obtain reliable results when measuring molecular distances. Finally, to reduce crosstalk, I developed an algorithm to estimate the crosstalk signal for every pixel of each frame of the acquisition and correct for it. This ensures that colocalization or object-based measurements are performed without having false positives due to crosstalk.

In the second part of the thesis, I showed how I applied the setup to the study of bacterial subcellular organization. In fact, despite bacteria apparently lack any kind of subcellular organization, recent studies on metabolic pathways suggested a compartmentalization between enzymes of the same metabolic pathway. To be able to study molecular compartmentalization I first validated my method by applying it to a positive control and a negative control sample. As positive control, bacteria were transfected with a plasmid to obtain PAmCherry1-HisH and PAGFP-HisF, being HisF, HisH two proteins of the histidine metabolic pathway, which have been shown to interact through indirect methods. As negative control, bacteria were transfected with a plasmid to obtain PAmCherry1-HisH, PAGFP-aaC, being HisH, aaC a couple of non-interacting proteins. I developed an

acquisition and an analysis procedure to study the mutual subcellular organization of biological samples and get quantitative results. My analysis procedure, after correcting for crosstalk and chromatic aberrations, combines a local density-based co-localization index and a nearest neighbor search to identify co-localizing pairs of molecules and measure the distance between them. The consistency of the results obtained from the analysis of simulations and acquisitions demonstrated that my method enables single molecule co-localization analysis and that it can be used to assess the degree of co-localization between two populations. Specifically, in interacting proteins I found both a higher co-localization index (CI, i.e. a measure of the similarity of spatial distributions) and a higher percentage of co-localizing proteins with respect to the non-interacting ones. However, from multicolour PALM imaging, due to the limited resolution of the system, I couldn't measure distances below 10 nm. This limit was set by the localization errors along the xy axis and by the registration error due to the chromatic aberrations' correction. Moreover, the high molecular density of fluorophores in the small bacterial volume prevented three-dimensional imaging as the PSFs of the emitters overlapped and they became undistinguishable. As a consequence, to further increase the resolution of the system we decided to combine ExM treatment of the biological sample with PALM imaging process. By combining these techniques, I found an average co-localization distance of $6.8 \pm 2.7$ nm for the 2D and of $19.3 \pm 5.6$ nm for the 3D. The consistency between the results of PALM, 2D and 3D Ex-PALM validate the capability of the method to quantify significant differences of both CIs and distances between the positive and the negative control samples. The combination of ExM protocol with PALM allowed to consistently reduce the minimum measurable distance, even though the expansion should be further optimized to reduce the loss of proteins. With our method robustly validated we are now ready to study molecular distribution of native proteins within bacteria. To

this end we will need a bacterial strain with native HisF and HisH proteins replaced by their fluorescent counterparts, PAmCherry1-HisH and PAGFP-HisF respectively, to directly observe their physiological expression levels under their native promoter. Additionally, in order to test the hypothesis of molecular compartmentalization, we will examine the spatial organization of other pairs of enzymes of the histidine metabolic pathway. Subsequently, we will also investigate the distribution of genes within the same metabolic pathway to expand knowledge on the epigenetics of operons. The further steps of the project will be carried out simultaneously with the implementation of the localization algorithms that will be refined through the introduction of clusters' analysis using correlation functions.

To conclude, the development of this technique will allow to thoroughly investigate the subcellular environment of bacteria and thus address fundamental questions of molecular biology such as the existence of a compartmentalization within prokaryotic cells and the epigenetics of operons.

# Chapter 6

# Appendices

## 6.1 Dual View implementation and alignment

This section reports the procedure followed to implement and align the dual view on our experimental setup. The main steps are:

1) Checking the alignment of the excitation beams by checking their centering and back reflection.
2) Preparing a calibration sample made with fluorescent beads (as described in section 6.4.1) and checking the fluorescence detection alignment.
3) Taking a calibration slide (Thorlabs, 10 mm stage micrometer with 50 μm divisions, R1L3S1P) and checking the brightfield detection alignment (**Figure 6.1a**).
4) Adjusting the position and aperture of the slit to select only half of the field of view (**Figure 6.1b**).
5) Inserting first dichroic mirror (DM4 in **Figure 2.11a**) and centering the reflected image on mirror M2.
6) Inserting the second dichroic mirror (DM5 in **Figure 2.11a**) and overlapping reflected and transmitted images of the two channels.
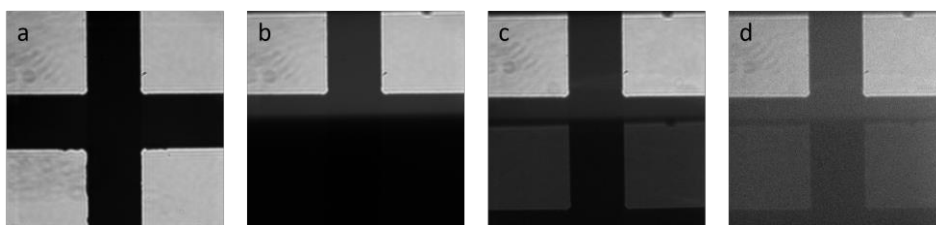


**Figure 6.1:** Main steps of dual view alignment. **(a)** Full field of view; (b) partial closure of the slit to select only half of the field of view; **(c)** insertion and alignment of dichroic mirrors in the detection path to visualize both channels; **(d)** insertion of filters to select only the peak wavelength.

7) Using mirror M2 micrometric screws to separate the images, so that the transmitted image is detected in one half and the reflected image in the other half (**Figure 6.1c**).

8) Finally, inserting the fluorescent filters in their respective optical path (**Figure 6.1d**).

## 6.2 Astigmatism calibration

As previously discussed in section 1.3.1, three-dimensional single-molecule imaging can be performed with different techniques. The most common approach is to introduce a weak cylindrical lens into the imaging path to produce a slight astigmatism in the image. As a result, the image of a single molecule become an ellipse whose ellipticity depends on the position of the emitter with respect to the focal plane. If the emitter is in focus, its image appears round; if it's above or below the focal plane, it's ellipsoidal. Calibrating the system, which means finding the relation between the widths of the ellipse and the axial position of the emitter, is necessary to localize the molecule in the three dimensions. This section reports the astigmatism calibration we performed for the two channels of our setup.

Astigmatism calibration is usually performed with a *z-stack*, that is a series of images of the same field of view but at different depths, of fluorescent beads whose size is smaller than the diffraction limit of the system. Hence, for this measurement I prepared a sample with 100 nm-diameter multicolour fluorescent beads non-specifically attached to a coverslip (as described in section 6.4.1) appropriately diluted to achieve an approximate concentration of ten non-overlapping – and thus resolvable – beads per field of view. By moving the piezoelectric translator on which the objective is mounted, I acquired a series of images of the same field of view – one for each axial position – in steps of 10 nm to cover a range of 2 μm. This multi-slice acquisition was automatically performed using the custom LabVIEW program described in section 2.3. For this measurement, the Electron

Multiplication (EM) gain and the exposure time of the EMCCD camera were set to 200 and 100 ms respectively, while the intensities of the excitation lasers (488 nm and 552 nm) were set to $\sim$34 W/cm$^2$.

Images acquired with SMLM techniques need to be processed to find the positions of single emitters through the fitting of the PSF. This task is accomplished with *ThunderSTORM* [161], an open-source plugin for the image analysis program *ImageJ* [162], [163]. ThunderSTORM was specifically developed to process and visualize images acquired with STORM and PALM microscopies. ThunderSTORM's workflow is reported in **Figure 6.2**. Briefly, ThunderSTORM takes as input a series of raw images and filters them using convolution-based filters (such as gaussian filter, wavelet filter... etc.). After that, through a user-specified intensity threshold, it performs an approximate localization of molecules (for example, detecting the local intensity maxima or calculating the centroid of connected components)[7]. Then, it performs
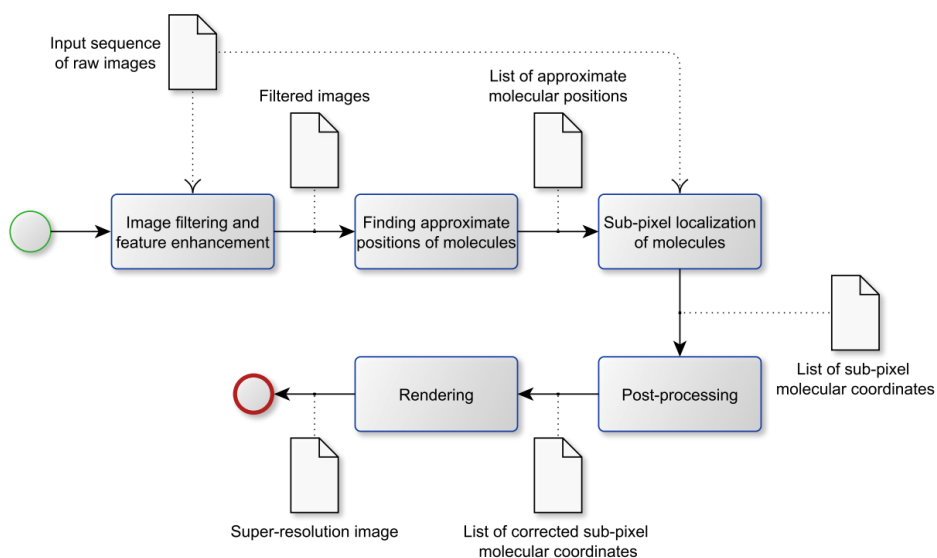


**Figure 6.2:** Main steps of ThunderSTORM data analysis workflow for an input sequence of raw images. Image retrieved from [161].

---

[7] Selecting the right threshold value is crucial for achieving accurate results. If the threshold is too high there will be lots of rejected molecules (false negatives), while if it's too low the background noise whose signal is higher than the threshold will be mistaken for real molecules (false positives).

a sub-pixel localization of molecules by fitting the intensity profile (the PSF) of the previously identified molecules with a function chosen by the operator, while the localization uncertainty is calculated using the Thompson-Larson-Webb formula corrected by Mortensen (equation 1.4). The output of the sub-pixel localization is a list of coordinates that can be rendered into a super-resolution image by displaying each molecule as a two-dimensional Gaussian (in case of 2D imaging) with an amplitude given by the maximum fluorescence intensity and a standard deviation corresponding to their respective localization uncertainty. Finally, ThunderSTORM provides a variety of post-processing methods (such as lateral drift correction, removing molecules with poor localization… etc.) that can be applied to the results obtained from previous steps.

For astigmatism-based 3D imaging, ThunderSTORM's PSF model is a rotated elliptical gaussian[8] given by the formula:

$$PSF(x, y \mid \theta, \Phi) = \frac{\theta_N}{2\pi\theta_{\sigma_1}\theta_{\sigma_2}} e^{-\left(\frac{x'^2}{2\theta_{\sigma_1}^2} + \frac{y'^2}{2\theta_{\sigma_2}^2}\right)} + \theta_b \qquad (6.1)$$

with

$$x' = (x - \theta_x)\cos\Phi - (y - \theta_y)\sin\Phi \qquad (6.2)$$
$$y' = (x - \theta_x)\sin\Phi + (y - \theta_y)\cos\Phi \qquad (6.3)$$

where $\theta_x$ and $\theta_y$ are the sub-pixel molecular coordinates, $\theta_{\sigma_1}$ and $\theta_{\sigma_2}$ are the widths of the molecule along two perpendicular axes rotated by the angle $\Phi$ with respect to $xy$ coordinates, $\theta_N$ is the total number of photons emitted by a single molecule and $\theta_b$ is the background offset. To analyze data acquired with 3D SMLM imaging, ThunderSTORM requires calibration curves to find the axial position

---

[8] ThunderSTORM's PSF model for astigmatism-based 3D imaging is a *rotated* elliptical gaussian because it considers that the camera chip might not be aligned with the cylindrical lens.

of single molecules. This can be done through ThunderSTORM's function *cylindrical lens calibration* that, given a z-stack of images of sub-diffraction fluorescent beads, allows to find the ellipsoid orientation angle $\Phi$ and the system's calibration curves $(\sigma_1(z), \sigma_2(z))$ that associate each axial position with a specific ellipticity. First, ThunderSTORM fits the images of the beads using the elliptical Gaussian given by equation (6.1) with $\Phi$ as a free parameter and, after discarding circular PSFs that cannot be used to determine the angle, calculates the final orientation angle as the circular mean of all remaining measurements. Then, using the approximate positions of single molecules and the orientation angle, the images of the beads are fit again using the elliptical Gaussian given by equation (6.1) with $\Phi$ fixed to obtain the widths of the molecule $(\theta_{\sigma_1}, \theta_{\sigma_2})$. ThunderSTORM's calibration curves are:

$$\sigma_1(z) = a_1(z - c_1)^2 + b_1 \qquad (6.4)$$
$$\sigma_2(z) = a_2(z - c_2)^2 + b_2 \qquad (6.5)$$

To estimate the coefficients $a_1, b_1, c_1, a_2, b_2, c_2$, first ThunderSTORM fits $\theta_{\sigma_1}$ and $\theta_{\sigma_2}$ of each bead with the pair of polynomials of equations 6.4 and 6.5. From these fits, it determines a common focal plane for the beads as $\frac{c_1 + c_2}{2}$ and shifts the data along the z-axis such that all beads are in the same plane. At this point, it performs another fit of all the shifted data with the pairs of polynomials to find the final coefficients. The "zero" axial position is given by the intersection of the two polynomials. In **Table 6.1** are reported the results of the calibration performed using the z-stack of images of sub-diffraction fluorescent beads described above.

| Channel | $\Phi$ [rad] | $a_1$ [pixel/nm²] | $b_1$ [pixel] | $c_1$ [nm] | $a_2$ [pixel/nm²] | $b_2$ [pixel] | $c_2$ [nm] |
|---------|-----------|--------------------|----------------|-------------|--------------------|----------------|-------------|
| Blue | $3.07 \cdot 10^{-2}$ | $1.54 \cdot 10^{-6}$ | 1.25 | 1109 | $2.69 \cdot 10^{-6}$ | 1.27 | $-641$ |
| Green | $3.88 \cdot 10^{-3}$ | $1.32 \cdot 10^{-6}$ | 1.31 | 1084 | $2.57 \cdot 10^{-6}$ | 1.39 | $-602$ |

**Table 6.1:** Ellipsoid orientation angle and calibration curves' coefficients resulting from ThunderSTORM's calibration functions.

Once the calibration curves are found, the axial position $\hat{z}$ of each molecule is determined by minimizing the distance between the fitted values $(\theta_{\sigma_1}, \theta_{\sigma_2})$ and the calibration curves $(\sigma_1(z), \sigma_2(z))$, thus by:

$$\hat{z} = \arg\min_z \left( \left( \sqrt{\theta_{\sigma_1}} - \sqrt{\sigma_1(z)} \right)^2 + \left( \sqrt{\theta_{\sigma_2}} - \sqrt{\sigma_2(z)} \right)^2 \right) \quad (6.6)$$

**Figure 6.3** shows the calibration curves obtained with ThunderSTORM for the two channels of our setup. It is evident that the second-degree polynomials do not fit the data correctly, especially $\sigma_1(z)$. Consequently, instead of using ThunderSTORM's calibration curves, we decided to use third-degree polynomials, such as

$$\sigma_1(z) = a_1 + b_1 x + c_1 x^2 + d_1 x^3 \quad (6.7)$$
$$\sigma_2(z) = a_2 + b_2 x + c_2 x^2 + d_2 x^3 \quad (6.8)$$

that could better match the data trend. Results of the correct calibration are reported in **Table 6.2**, while data fitted with the new calibration curves are shown in **Figure 6.4**.

| Channel | Blue | Green |
|---|---|---|
| $a_1$ [pixel] | $3.273 \pm 0.010$ | $2.918 \pm 0.006$ |
| $b_1$ [pixel/nm] | $(-4.43 \pm 0.04) \cdot 10^{-3}$ | $(-3.72 \pm 0.02) \cdot 10^{-3}$ |
| $c_1$ [pixel/nm²] | $(-1.9 \pm 0.8) \cdot 10^{-7}$ | $(5.2 \pm 0.3) \cdot 10^{-7}$ |
| $d_1$ [pixel/nm³] | $(5.5 \pm 0.2) \cdot 10^{-9}$ | $(4.11 \pm 0.08) \cdot 10^{-9}$ |
| $a_2$ [pixel] | $2.388 \pm 0.009$ | $2.294 \pm 0.008$ |
| $b_2$ [pixel/nm] | $(3.40 \pm 0.04) \cdot 10^{-3}$ | $(3.15 \pm 0.03) \cdot 10^{-3}$ |
| $c_2$ [pixel/nm²] | $(2.60 \pm 0.08) \cdot 10^{-6}$ | $(2.99 \pm 0.04) \cdot 10^{-6}$ |
| $d_2$ [pixel/nm³] | $(3.0 \pm 1.7) \cdot 10^{-10}$ | $(-3.7 \pm 1.0) \cdot 10^{-9}$ |

**Table 6.2:** Calibration curves' coefficients resulting from third-order degree calibration functions.
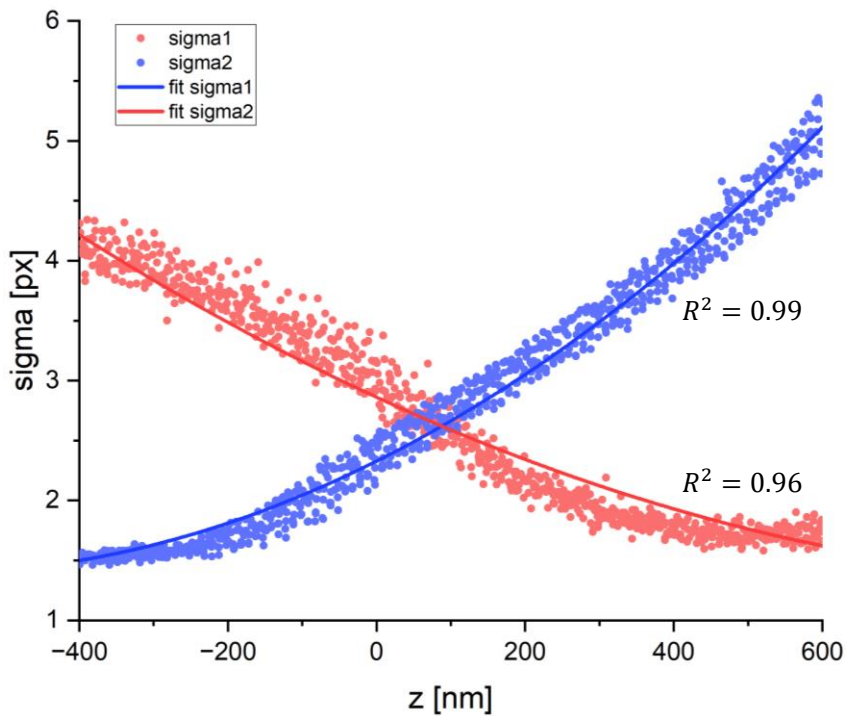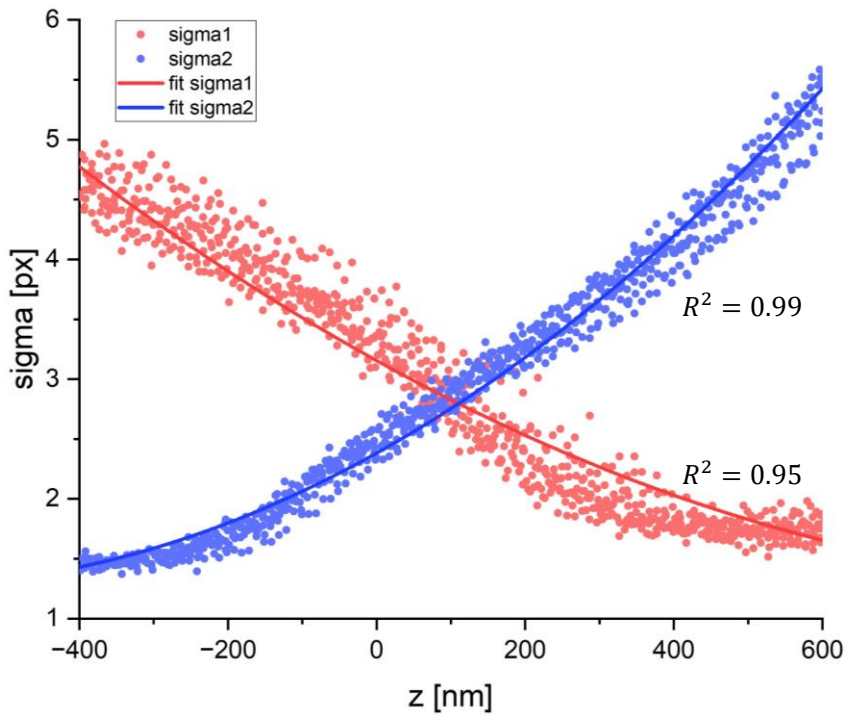
**Figure 6.3:** ThunderSTORM's calibration curves for the blue (top) and green (bottom) channels. Points represents the widths $\theta_{\sigma_1}$ and $\theta_{\sigma_2}$ obtained from the elliptical gaussian fit while the lines are the calibration curves $\sigma_1(z)$, $\sigma_2(z)$ reported in equations 6.4 and 6.5.
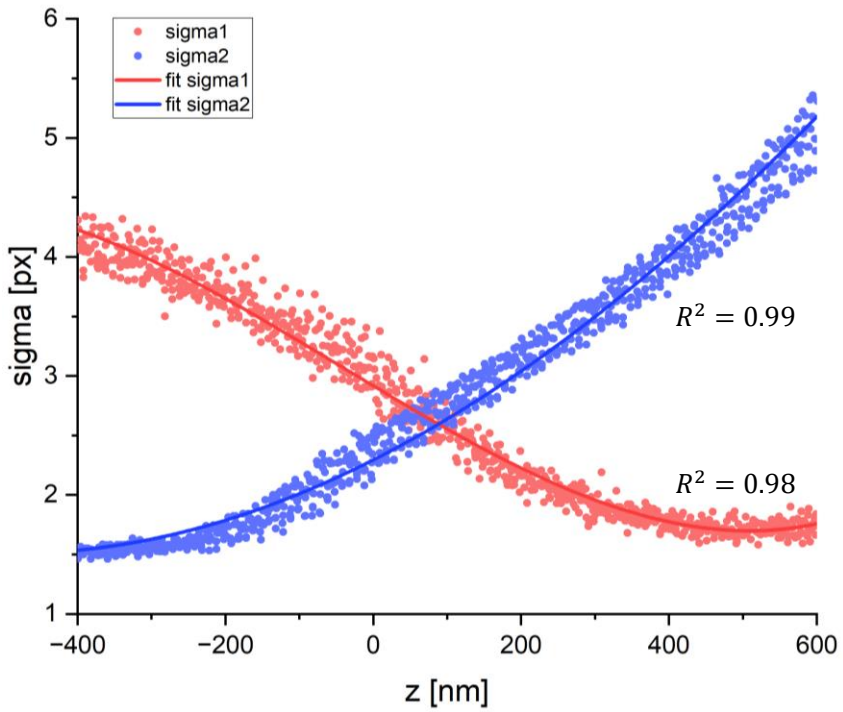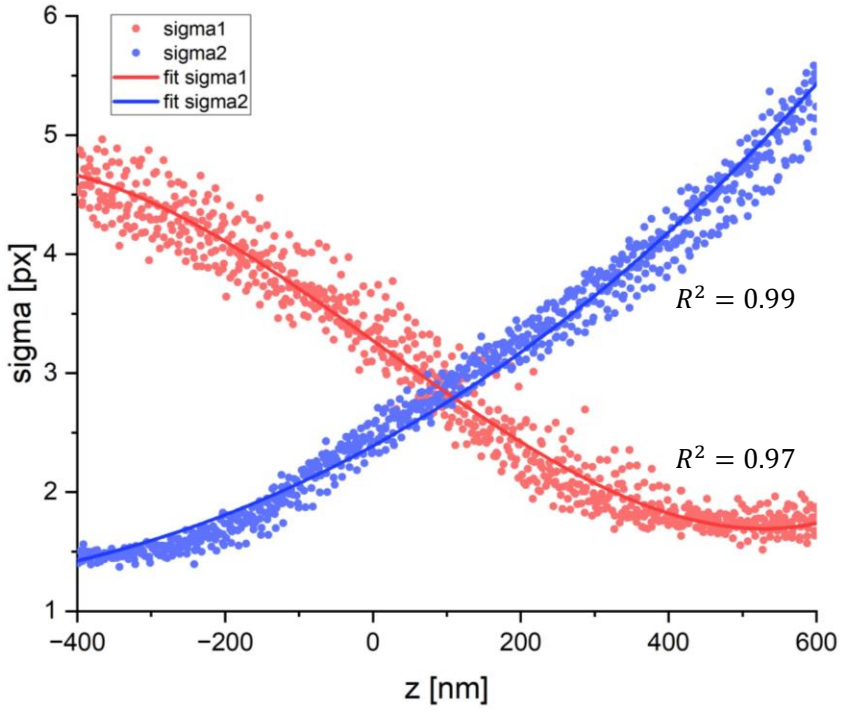
**Figure 6.4:** Calibration curves we used for the blue (top) and green (bottom) channels. Points represents the widths $\theta_{\sigma_1}$ and $\theta_{\sigma_2}$ obtained from the elliptical gaussian fit while the lines are the calibration curves $\sigma_1(z)$, $\sigma_2(z)$ reported in equations 6.7 and 6.8.
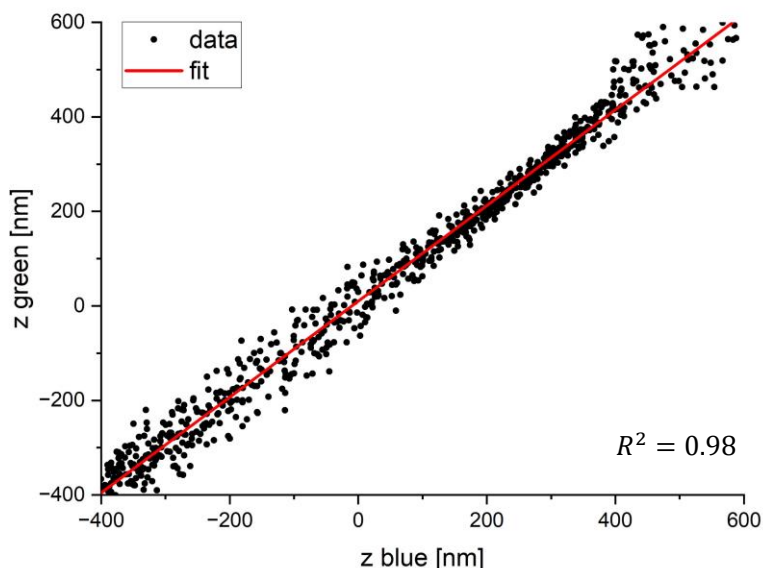
**Figure 6.5:** Relation between the axial position of the calibration beads in the two channels. The dark spots represent the z coordinate in the blue (abscissa axis) and green (ordinate axis) channels while the red line is the linear fit.

Calibration using third-degree polynomial curves enables determining the axial position of molecules with an average deviation from the real positions of only 25 nm (for the green channel) and 28 nm (for the blue channel). Moreover, since due to chromatic aberration focal planes are different for different wavelengths, we also estimated the axial shift between the two channels. By comparing the values of the axial positions of the beads in the two channels, we observed a linear relation among them (as shown in **Figure 6.5**):

$$z_{green} = a + z_{blue} \cdot b \qquad (6.9)$$

Therefore, by fitting the data with a linear curve we obtained the intercept ($a$) and the slope ($b$) of the line to correct the axial shift. Results of the linear fit are reported in **Table 6.3**.

| Intercept ($a$) [nm] | Slope ($b$) [a.u.] |
|---|---|
| $9.8 \pm 1.3$ | $1.013 \pm 0.005$ |

**Table 6.3:** Results of the linear fit used to find the axial shift between the focal planes of the two channels.

## 6.3 Highly Inclined and Laminated Optical sheet (HILO)

Single-molecule super-resolution microscopy relies on the precise localization of single fluorescent emitters. Being the localization accuracy dependent on the number of collected photons, it is of crucial importance to minimize the background contribution. This can be achieved by using special cameras cooled at very low temperatures (e.g., -80°C) to minimize the thermal noise and with efficient systems to amplify the signal for emitters (such as EMCCD cameras), and, most importantly, by adopting illumination geometries to reduce the sample excitation volume and, consequently, the out-of-focus fluorescence contribution to the acquired signal. In widefield SMLM techniques (such as STORM and PALM) there's no intrinsic optical sectioning provided by pinholes or focused illumination; therefore, the only way to limit fluorescence coming from out-of-focus planes is to act on the pattern of the excitation light, to limit the excited volume as much as possible along the z axis. One of the most effective ways to achieve excitation confinement is through *total internal reflection* (TIR) illumination. As shown in **Figure 6.6**, by focusing a beam on the back focal plane of a high-numerical aperture objective along an axis which
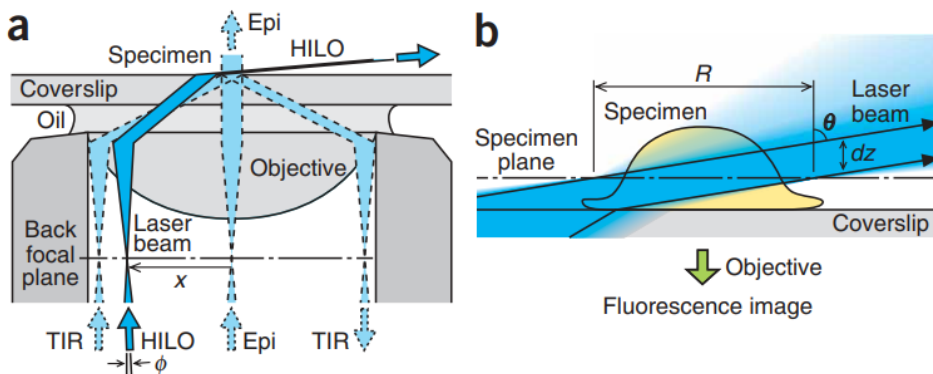


**Figure 6.6:** HILO microscopy. **(a)** Comparison between epifluorescence (Epi), TIR and HILO illumination; **(b)** Example of a sample illuminated with a thin sheet of laser beam. For geometrical optics approximation, the thickness of the light sheet $dz$ along the $z$ direction is roughly $dz = R / tan\theta$ , where $R$ is the diameter of the illuminated area at the specimen plane and θ the incident angle at the specimen. Image retrieved from [165].
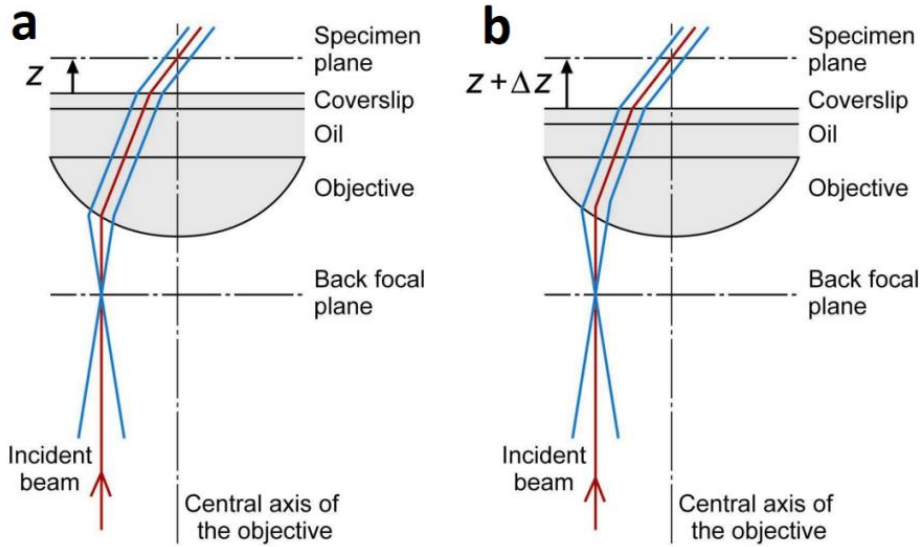
**Figure 6.7:** Beam paths of HILO microscopy before **(a)** and after **(b)** a z-directional shift of the objective. A beam parallel to the central axis of the objective (red line) passes through the center of the specimen plane [ed, the focal plane]. A beam focused at the back focal plane (blue line) becomes parallel at the specimen plane. In HILO, the illumination beam always passes through the center of the specimen plane, which means the illumination beam follows the z-directional shift of the specimen plane. Image and caption retrieved from [165].

is parallel to the optical axis, but shifted sideways from the center by a distance $x$, the beam comes out of the objective collimated and inclined by an angle $\theta$. If this angle is higher than the critical angle, total internal reflection occurs at the interface between glass (the coverslip) and water (the sample). Light no longer passes through the second medium, but it's back reflected and it creates an evanescent electromagnetic field that penetrates into the less refractive material (in this case the sample). Since this electromagnetic field decays exponentially within $\sim$100 nm from the interface, this practically greatly limits the excitation volume to the section of the sample in immediate contact with the coverslip surface [164]. Therefore, application of TIR microscopy is limited to surfaces, thus limiting its application to cell surface or in vitro experiments. This limitation can be overcome by using the *highly inclined and laminated optical sheet* (HILO) method, in which, the excitation is performed with a thin highly inclined Gaussian beam. The reduced thickness and the inclination of

the optical sheet limit the excitation volume to a "slice" of sample, thus allowing for largely reduced background fluorescence and much higher contrast compared to epifluorescence illumination, while retaining the ability to image in depth along the $z$ axis. Moreover, as shown in **Figure 6.7**, since the illumination beam always passes through the center of the specimen plane, HILO can be used to perform scanning volumetric imaging. In conclusion, HILO is a good compromise between epifluorescence and TIR because it allows volumetric imaging, but with an increased signal/noise ratio of about eightfold greater than that of epi-illumination [165]. Recent work from our group has demonstrated that an inclined beam with subcellular thickness of few microns can be obtained by specific beam shaping [159] which is crucial to achieve super-resolution in thick samples, such as expanded samples ("Single objective light sheet allows volumetric super-resolution imaging of efflux pumps distribution in bacterial biofilms" Vignolini T., Capitanio M., *Caldini C*., Gardini L. and Pavone F. S., 2024, under revision).

## 6.4 Biological protocols

This section reports all the biological protocols used to calibrate the optical system and prepare bacterial samples.

### 6.4.1 Calibration slide with multicolour fluorescent beads

Materials:

- 26x76 mm$^2$ microscope slide
- 24x40 mm$^2$ coverslip
- Double-sided tape (thickness $\sim$ 100 µm)
- TetraSpeck$^{TM}$ microspheres (ThermoFisher, T7279, 0.1 µm, blue/green/orange/dark red)
- Phosphate-buffered saline (PBS) 1x
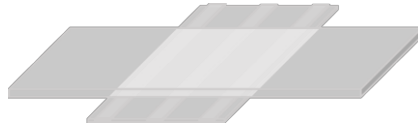
**Figure 6.8:** Two-channel chamber composed of a rectangular coverslip attached on a microscope slide through thin strips of double-sided tape, which also delimit the channels. Each channel has a volume of 20 μl. Solutions are fluxed into the channels by gently pipetting through one of the open ends.

Methods:

1) Prepare a two-channel chamber as shown in **Figure 6.8**. Usually only one channel is required for each solution, but with two it's possible to repeat the measurement under different conditions using the same chamber.

2) Dilute microspheres 1:1000 in PBS, put 20 μl of the dilution in one channel and wait 15 minutes.

3) Wash with 40 μl of PBS.

Once prepared, this sample can be used for several hours. To use it for an extended period, such as several days, it is essential to seal with silicone grease to prevent drying.

## 6.4.2 Sample preparation protocol for simultaneous multicolour PALM imaging

Materials:

- E. Coli bacteria glycerol stock
- Culture medium: M9 minimal medium with added glucose (0.4%), histidine (25 μg/ml), IPTG (50 μg/ml) and kanamycin (50 μg/ml)
- 4% Paraformaldehyde (PFA)
- 2% Agarose
- Phosphate-buffered saline (PBS) 1x
- 26x76 mm$^2$ microscope slides
- 24x24 mm$^2$ coverslip
- Scotch tape (thickness $\sim$ 100 μm)

Methods:

1) Grow bacteria in 3 ml of culture medium for around 31 hours at 37°C and 215 rpm.
2) Collect cells via centrifugation at 10000g for 2 minutes and resuspend the pellet in 1 ml of PBS.
3) Wash once with PBS via repeated centrifugation and resuspension, then incubate in PFA 4% for 10 minutes.



1. Take a microscope slide and use thin strips of scotch tape (about 300 μm) to create a square region of around 24x24 mm$^2$.

2. Drop 200 μl of liquid 2% agarose in the center of the square. If the agarose is prepared with microwave, wait 5-10 s before the next step. If the agarose temperature is too high when it's covered, it will come out of the region and the pad won't form properly.

3. Cover with another microscope slide and hold it down until the agarose solidifies. Be careful not to create bubbles during the covering because they can create issues during the imaging process.

4. Carefully remove the upper microscope slide.

5. Carefully remove the thin strips of scotch tape.

6. Take 20 μl of bacteria suspended in PBS and drop it on the surface of the solidified agarose pad.

7. Wait until it dries and the bacteria are completely embedded with the pad (~30 minutes).

8. Cover with a 24x24 mm$^2$ coverslip. If the agarose is too dry, put few μl of PBS to ease the attachment of the coverslip.

**Figure 6.9:** Step by step instructions of the assembly protocol of an agarose pad with embedded bacteria.

4) Remove the fixative, wash once with PBS and then resuspend in 1 ml of PBS.

5) Prepare the agarose pad, drop 20 µl of bacteria and wait for it to dry (around ~30 minutes) as shown in **Figure 6.9**.

Once the sample is ready it can be used for 2-3 hours before degrading.

### 6.4.3 Expansion microscopy of E. Coli bacteria

Materials:

- E. Coli bacteria glycerol stock
- Culture medium: M9 minimal medium with added glucose (0.4%), histidine (25 µg/ml), IPTG (50 µg/ml) and kanamycin (50 µg/ml)
- 4% Paraformaldehyde (PFA)
- Phosphate-buffered saline (PBS) 1x
- PBSTx: 0.3% (w/v) Triton X-100 in PBS
- 50% Methanol in PBSTx
- TAE buffer: 40 mM Tris base, 20 mM Acetic acid and 1 mM Ethylenediaminetetraacetic acid (EDTA) in MilliQ $H_2O$
- Methacrylic Acid N-HydroxySuccinimide ester (MA-NHS) stock solution: 1 M MA-NHS in dimethyl sulfoxide (DMSO)
- Phosphate buffer: 50 mM potassium phosphate in MilliQ $H_2O$. Adjust pH to 4.9. This solution should be made fresh before use.
- Mutanolysin stock solution: mutanolysin 10000 u/ml in MilliQ $H_2O$.
- Monomer solution: 2 M NaCl, 2.5% (w/w) acrylamide, 0.15% (w/w) bisacrylamide, 8.625 % (w/w) sodium acrylate in PBS.
- Gelation solution: 0.01% (v/v) 4-hydroxy-TEMPO, 0.2% (w/v) ammonium persulfate (APS), and 0.2% (v/v) tetramethylethylenediamine (TEMED) in monomer solution.

This solution should be made fresh in ice just before the gelation step. APS should be added at last.

- Digestion buffer: 0.5% Triton X-100, 0.8 M guanidine HCl and 8 units/ml Proteinase K (ProK) in TAE buffer. Digestion buffer without ProK can be stored at -20°C for some months. ProK should be added just before use.
- 0.1% Poly-L-lysine solution
- 13-mm diameter coverslips
- 18-mm diameter coverslips
- 100-mm petri dishes
- 6-well plate

Methods:

1) Grow bacteria in 5 ml of culture medium for about 31 hours at 37°C and 215 rpm.
2) Collect cells via centrifugation at 10000g for 2 minutes and resuspend the pellet in 1 ml of PBS.
3) Wash once with PBS via repeated centrifugation and resuspension, then incubate in PFA 4% for 10 minutes.
4) Replace the fixative with PBS and measure the optical density at 600 nm ($OD_{600}$). It should be within 1.8-2.1.
5) Remove PBS and resuspend in 1 ml of PBSTx by gentle pipetting. Incubate cells for 30 minutes at room temperature on a nutator to permeabilize the membrane.
6) Centrifuge at 2000g for 5 minutes and resuspend in 1 ml of 50% methanol in PBSTx and agitate for 10 minutes. Do not centrifugate at relative centrifuge force (rcf) higher than 2000g because, due to the permeabilization, bacteria are more fragile than before and using a higher rcf could break them. For this reason, all the next centrifuges are at 2000g.
7) Remove the solution and incubate in PBSTx for 10 minutes with agitation.

8) Remove PBSTx and digest cell walls by incubating in 1 ml of phosphate buffer containing 320 unit/ml mutanolysin on a rotor overnight at 37 °C.

9) Wash in PBS three times and then incubate in 1 ml of 2 mM MA-NHS in PBS for 1 hour at room temperature to attach chemical anchors to proteins.

10) Wash in PBS three times, then replace PBS with 78 µl gelation solution[9] and incubate for 1 minute at 4 °C. Each sample (bacteria pellet diluted in the gelation solution) can yield three gels. Since gels are fragile and could easily break or get ruined in the further steps for several different reasons it is better to have some spare ones.

11) To ensure successful gelation, it is essential to use a humid gelation chamber otherwise the gel will dry. To assemble it, take a 6-well plate and place a humid piece of paper in each well[10]. Then, position a 18-mm diameter coverslip at the center of each well, drop 26 µl of bacterial suspension in its center (as shown in **Figure 6.10**) and cover it with 13-mm diameter coverslip[11]. Repeat the same steps for each well and then incubate the 6-well plate for 2 hours at 37 °C. During gelation, cells should mostly settle downwards, near the surface in contact with the 18-mm diameter coverslip.

12) Carefully remove the upper coverslip from the gel and the humid paper from each well. After repositioning the gel in its

---

[9] Be careful to remove all the PBS before resuspending the pellet with the gelation solution. If some PBS is left, the gel won't form properly and it will break in next steps or it will expand non-isotropically.

[10] The gelation chamber must be humid for the gel to form without drying. However, if the chamber is too humid, the gel won't be completely formed in 2 hours, but it will take longer. If the gel is not properly formed, it will expand non-isotropically and bacteria will break during the expansion process.

[11] It is advisable to drop the bacterial suspension in the centre of the 18-mm diameter coverslip to prevent it from going out of the edges during the covering with the 13-mm diameter coverslip. If some of the suspension goes out, the final gel will be thinner and will break during next steps.
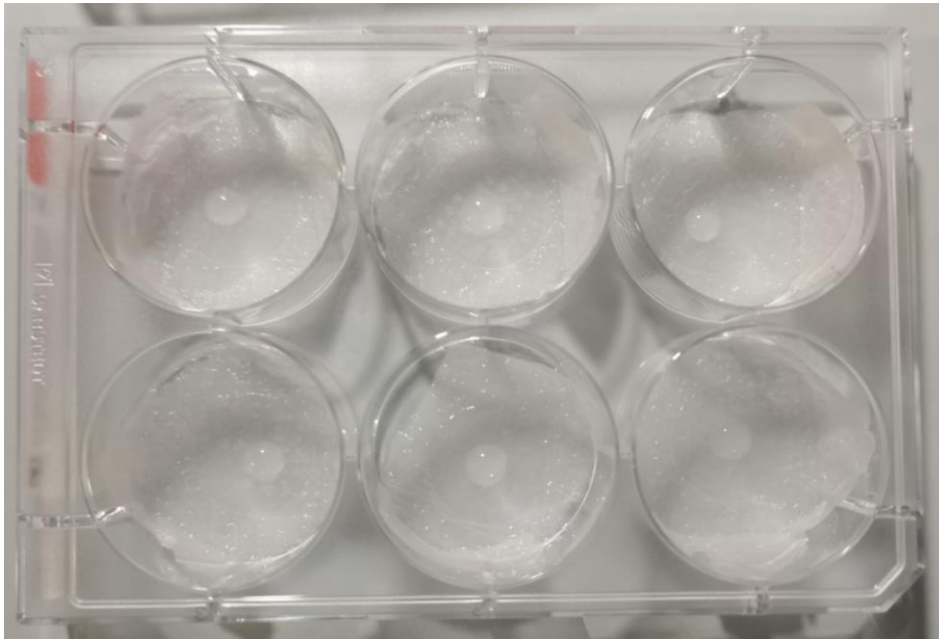
**Figure 6.10:** Assembling of the gelation chamber. Each well contains a piece of humid paper surrounded by an 18-mm diameter coverslip with 26 µl of bacterial suspension. To finalize the chamber, put a 13-mm diameter coverslip on the top.

well, add 2.5 ml of digestion buffer with proteinase K, seal the multi-well with parafilm to prevent evaporation and incubate for 3 hours at 37 °C. During digestion the gel should expand by a factor of around 1.5. For this reason, it is advisable to use a 6-well plate instead of a 12-well plate, as the gel could become too large for the latter after digestion.

13) Transfer the gel in a 100-mm petri dish using the lower coverslip, a needle and tweezers to facilitate the movement. Once the gel is in position, fill the dish with MilliQ $H_2O$ and allow the gel to expand at room temperature for 45 minutes, changing the water every 15 minutes. Alternatively, expansion can be performed overnight at 4 °C.

14) For sample mounting, coat the coverslip of the imaging chamber (**Figure 6.11**) with 0.1% poly-L-lysine for 5 minutes.

15) Remove the expansion water from the gel and cut it in small pieces to be imaged. Finally, take a piece of gel and gently place it into the imaging chamber with some expansion water to prevent drying of the gel.

**Figure 6.11:** Schematic view of the imaging chamber used for Expansion-PALM acquisitions.

Once prepared, the sample in the imaging chamber can be used for several hours.

## 6.5    Imaging protocols

This section includes imaging protocols used for calibration measurements and acquisitions with biological samples.

### 6.5.1 Calibration scan of the field of view with fluorescent beads and piezoelectric stage to correct for chromatic aberrations

The calibration scan of the field of view is performed as it follows:

1) The EM gain and the exposure time of the EMCCD camera are set respectively to 200 and 100 ms.

2) The scanning parameters are set to 63 (grid columns), 27 (grid rows), 600 nm (step size). With these parameters we scan almost the whole field of view in around 5 minutes. Other scanning parameters are reported in **Table 6.4** along with the acquisition time. It must be noted that, acquisition time depends not only by the number of frames and the exposure time, but also from the scanning procedure. It takes around 80 ms to turn off the camera, move the stage in another position and then turn the camera back on.

3) The 552 laser is turned on at 0.8 mW ($\sim$34 W/cm$^2$ out of the objective) and the sample is explored to find a region with one

or few isolated beads. The algorithm we developed to find the transformation function can identify the reference bead and discard the others if farer than 100 nm. However, if there are many beads it could happen that they occupy the same position at different timings and, when the image of the grid is reconstructed, their localizations are closer than 100 nm. This could lead the algorithm to select the wrong localization consequently compromising the accuracy of the transformation function.

4) Once the region of interest is selected, the 488 is turned on at the same power of 552 and the acquisition starts. We have developed an automated LabVIEW program that for each frame record the image, turn off the camera, move the stage in the next position, turn the camera back on. Once all the frames have been recorded, the camera is stopped and the lasers are turned off.

| Step size [nm] | Columns | Rows | Images per step | Number of frames | Acquisition time [min] |
|---|---|---|---|---|---|
| 100 | 380 | 160 | 1 | 60800 | 182.3 |
| 200 | 190 | 80 | 1 | 15200 | 45.6 |
| 300 | 127 | 53 | 1 | 6731 | 20.2 |
| 400 | 95 | 40 | 1 | 3800 | 11.4 |
| 500 | 76 | 32 | 1 | 2432 | 7.3 |
| 600 | 63 | 27 | 1 | 1701 | 5.1 |
| 700 | 54 | 23 | 1 | 1242 | 3.7 |
| 800 | 48 | 20 | 1 | 960 | 2.9 |
| 900 | 42 | 18 | 1 | 756 | 2.3 |
| 1000 | 38 | 16 | 1 | 608 | 1.8 |

**Table 6.4:** Scanning parameters for different scanning step sizes covering a field of view of around 38 x 16 μm$^2$.

## 6.5.2 Simultaneous multicolour PALM imaging of E. Coli bacteria

Simultaneous multicolour acquisition was performed as it follows:

1) The EM gain and the exposure time of the EMCCD camera are set respectively to 4 and 80 ms.

2) The halogen lamp is turned on to select the region of interest (ROI) of the sample. It's suggested to avoid having bacteria near the edges of the field of view because chromatic aberrations correction won't work over there and thus those localizations will be excluded during post-processing.

3) Once the ROI has been selected, the halogen lamp is turned off, the gain of the EMCCD camera is set to 400 and the illumination configuration of the lasers is set to HILO to maximize the signal to noise ratio.

4) The 488-nm laser is turned on at 3.56 mW (corresponding to ~200 W/cm$^2$ out of the objective), PAGFP is activated and around 10-20 frames are acquired. These initial frames of PAGFP acquisition will be used to assess and correct crosstalk. This approach is chosen as the initial frames tend to be densely populated, making it challenging to localize single molecules accurately. By adopting this strategy, we avoid losing any valuable localizations of PAGFP and discard only those that would likely be excluded anyway due to their densely populated nature.

5) 405-nm and 552-nm lasers are turned on at 80 nW and 9 mW respectively (corresponding to ~5 mW/cm$^2$ and ~500 W/cm$^2$ out of the objective), PAmCherry1 is activated and the simultaneous multicolour imaging starts. Each acquisition lasts about 2000 frames (including the first 20 frames with only PAGFP activated) as, by that point, PAGFP is fully photobleached and further localizations cannot be recorded.

### 6.5.3 Expansion-PALM microscopy of E. Coli bacteria

Expansion-PALM multicolour acquisition was performed as it follows:

1) The EM gain and the exposure time of the EMCCD camera are set respectively to 400 and 80 ms.

2) The slit in the excitation path placed after the circular iris (shown in **Figure 2.11**) is partially closed to select only a fraction of the field of view (about 10 x 20 $\mu m^2$). In fact, it has been demonstrated by Gardini et al. [159] that when using HILO illumination, reducing the thickness of the excitation beam, leads to an increase the resolution of the image. This is possible because by reducing the thickness of the beam, a thinner slice of the sample is excited, the background signal produced by the out-of-focus light decreases and thus the overall signal to noise ratio increases.

3) Since expanded bacteria are transparent and cannot be seen with brightfield, to find the plane where bacteria are placed all the lasers are turned on simultaneously at the same laser powers used for non-expanded bacteria (section 6.5.2).

4) Once the plane has been identified, the field of view is changed and the acquisition starts. Each acquisition lasts about 1000 frames. Expansion chemical treatment reduces the number of fluorescent proteins as well as their intensity. As a consequence, Ex-PALM acquisitions last less compared to PALM acquisitions and are not affected by crosstalk.

# References

[1]  J. W. Lichtman and J. A. Conchello, "Fluorescence microscopy," *Nature Methods*, vol. 2, no. 12. Nature Publishing Group, pp. 910–919, Dec. 18, 2005. doi: 10.1038/nmeth817.

[2]  A. G. Godin, B. Lounis, and L. Cognet, "Super-resolution microscopy approaches for live cell imaging," *Biophys J*, vol. 107, no. 8, pp. 1777–1784, Oct. 2014, doi: 10.1016/j.bpj.2014.08.028.

[3]  E. Abbe, "Beiträge zur Theorie des Mikroskops und der mikroskopischen Wahrnehmung," *Archiv für Mikroskopische Anatomie*, vol. 9, no. 1, pp. 413–468, 1873, doi: 10.1007/BF02956173.

[4]  M. Yamanaka, N. I. Smith, and K. Fujita, "Introduction to super-resolution microscopy," *Microscopy*, vol. 63, no. 3, pp. 177–192, Jun. 2014, doi: 10.1093/JMICRO/DFU007.

[5]  B. Huang, M. Bates, and X. Zhuang, "Super-Resolution Fluorescence Microscopy," *https://doi.org/10.1146/annurev.biochem.77.061906.092014*, vol. 78, pp. 993–1016, Jun. 2009, doi: 10.1146/ANNUREV.BIOCHEM.77.061906.092014.

[6]  G. ~B. Airy, "On the Diffraction of an Object-glass with Circular Aperture," *Transactions of the Cambridge Philosophical Society*, vol. 5, pp. 283–291, Jan. 1835.

[7]  M. Born and E. Wolf, "Principles of optics: electromagnetic theory of propagation, interference and diffraction of light," Pergamon, 1980, p. 461.

[8]  L. R. F.R.S., "XXXI. Investigations in optics, with special reference to the spectroscope,"

*https://doi.org/10.1080/14786447908639684*, vol. 8, no. 49, pp. 261–274, Oct. 2009, doi: 10.1080/14786447908639684.

[9]     "ZEISS Education in Microscopy and Digital Imaging: numerical aperture and resolution." [Online]. Available: https://zeiss-campus.magnet.fsu.edu/articles/basics/resolution.html

[10]    L. Schermelleh *et al.*, "Super-resolution microscopy demystified," *Nature Cell Biology 2019 21:1*, vol. 21, no. 1, pp. 72–84, Jan. 2019, doi: 10.1038/s41556-018-0251-8.

[11]    S. W. Hell and J. Wichmann, "Breaking the diffraction resolution limit by stimulated emission: stimulated-emission-depletion fluorescence microscopy," *Opt Lett*, vol. 19, no. 11, p. 780, Jun. 1994, doi: 10.1364/ol.19.000780.

[12]    J. A. Thorley, J. Pike, and J. Z. Rappoport, "Super-resolution Microscopy: A Comparison of Commercially Available Options," *Fluorescence Microscopy: Super-Resolution and other Novel Techniques*, pp. 199–212, Jan. 2014, doi: 10.1016/B978-0-12-409513-7.00014-2.

[13]    P. Bingen *et al.*, "Parallelized STED fluorescence nanoscopy," *Optics Express, Vol. 19, Issue 24, pp. 23716-23726*, vol. 19, no. 24, pp. 23716–23726, Nov. 2011, doi: 10.1364/OE.19.023716.

[14]    G. Donnert *et al.*, "Two-color far-field fluorescence nanoscopy," *Biophys J*, vol. 92, no. 8, pp. L67–L69, Apr. 2007, doi: 10.1529/biophysj.107.104497.

[15]    L. Meyer *et al.*, "Dual-Color STED Microscopy at 30-nm Focal-Plane Resolution," *Small*, vol. 4, no. 8, pp. 1095–1100, Aug. 2008, doi: 10.1002/SMLL.200800055.

[16]    R. Schmidt, C. A. Wurm, S. Jakobs, J. Engelhardt, A. Egner, and S. W. Hell, "Spherical nanosized focal spot unravels the interior

of cells," *Nature Methods 2008 5:6*, vol. 5, no. 6, pp. 539–544, May 2008, doi: 10.1038/nmeth.1214.

[17] C. Eggeling *et al.*, "Direct observation of the nanoscale dynamics of membrane lipids in a living cell," *Nature 2008 457:7233*, vol. 457, no. 7233, pp. 1159–1162, Dec. 2008, doi: 10.1038/nature07596.

[18] J. I. Hotta *et al.*, "Spectroscopic rationale for efficient stimulated-emission depletion microscopy fluorophores," *J Am Chem Soc*, vol. 132, no. 14, pp. 5021–5023, Apr. 2010, doi: 10.1021/JA100079W/SUPPL_FILE/JA100079W_SI_001.PDF.

[19] B. R. Rankin *et al.*, "Nanoscopy in a living multicellular organism expressing GFP," *Biophys J*, vol. 100, no. 12, pp. L63–L65, Jun. 2011, doi: 10.1016/j.bpj.2011.05.020.

[20] V. Westphal, S. O. Rizzoli, M. A. Lauterbach, D. Kamin, R. Jahn, and S. W. Hell, "Video-rate far-field optical nanoscopy dissects synaptic vesicle movement," *Science (1979)*, vol. 320, no. 5873, pp. 246–249, Apr. 2008, doi: 10.1126/SCIENCE.1154228/SUPPL_FILE/WESTPHAL.SOM.PDF.

[21] W. Lukosz, "Optical Systems with Resolving Powers Exceeding the Classical Limit. II," *JOSA, Vol. 57, Issue 7, pp. 932-941*, vol. 57, no. 7, pp. 932–941, Jul. 1967, doi: 10.1364/JOSA.57.000932.

[22] M. G. L. Gustafsson, "Surpassing the lateral resolution limit by a factor of two using structured illumination microscopy," *J Microsc*, vol. 198, no. 2, pp. 82–87, May 2000, doi: 10.1046/J.1365-2818.2000.00710.X.

[23] B. Harke, C. K. Ullal, J. Keller, and S. W. Hell, "Three-dimensional nanoscopy of colloidal crystals," *Nano Lett*, vol. 8,

no. 5, pp. 1309–1313, May 2008, doi: 10.1021/NL073164N/SUPPL_FILE/NL073164NSI20071204_024011.PDF.

[24] M. G. L. Gustafsson *et al.*, "Three-dimensional resolution doubling in wide-field fluorescence microscopy by structured illumination," *Biophys J*, vol. 94, no. 12, pp. 4957–4970, 2008.

[25] T. A. Planchon *et al.*, "Rapid three-dimensional isotropic imaging of living cells using Bessel beam plane illumination," *Nature Methods 2011 8:5*, vol. 8, no. 5, pp. 417–423, Mar. 2011, doi: 10.1038/nmeth.1586.

[26] X. Li *et al.*, "Three-dimensional structured illumination microscopy with enhanced axial resolution," *Nature Biotechnology 2023*, pp. 1–13, Jan. 2023, doi: 10.1038/s41587-022-01651-1.

[27] L. Schermelleh *et al.*, "Subdiffraction multicolor imaging of the nuclear periphery with 3D structured illumination microscopy," *Science (1979)*, vol. 320, no. 5881, pp. 1332–1336, Jun. 2008, doi: 10.1126/SCIENCE.1156947/SUPPL_FILE/SCHERMELLEH.SOM.PDF.

[28] A. C. N. Brown *et al.*, "Remodelling of Cortical Actin Where Lytic Granules Dock at Natural Killer Cell Immune Synapses Revealed by Super-Resolution Microscopy," *PLoS Biol*, vol. 9, no. 9, p. e1001152, Sep. 2011, doi: 10.1371/JOURNAL.PBIO.1001152.

[29] J. Guizetti *et al.*, "Cortical constriction during abscission involves helices of ESCRT-III-dependent filaments," *Science (1979)*, vol. 331, no. 6024, pp. 1616–1620, Mar. 2011, doi: 10.1126/SCIENCE.1201847/SUPPL_FILE/GUIZETTI.SOM.PDF.

[30] S. Lawo, M. Hasegan, G. D. Gupta, and L. Pelletier, "Subdiffraction imaging of centrosomes reveals higher-order organizational features of pericentriolar material," *Nature Cell Biology 2012 14:11*, vol. 14, no. 11, pp. 1148–1158, Oct. 2012, doi: 10.1038/ncb2591.

[31] V. Mennella *et al.*, "Subdiffraction-resolution fluorescence microscopy reveals a domain of the centrosome critical for pericentriolar material organization," *Nature Cell Biology 2012 14:11*, vol. 14, no. 11, pp. 1159–1168, Oct. 2012, doi: 10.1038/ncb2597.

[32] P. Kner, B. B. Chhun, E. R. Griffis, L. Winoto, and M. G. L. Gustafsson, "Super-resolution video microscopy of live cells by structured illumination," *Nature Methods 2009 6:5*, vol. 6, no. 5, pp. 339–342, Apr. 2009, doi: 10.1038/nmeth.1324.

[33] J. Gelles, B. J. Schnapp, and M. P. Sheetz, "Tracking kinesin-driven movements with nanometre-scale precision," *Nature 1988 331:6155*, vol. 331, no. 6155, pp. 450–453, 1988, doi: 10.1038/331450a0.

[34] E. A. Abbondanzieri, W. J. Greenleaf, J. W. Shaevitz, R. Landick, and S. M. Block, "Direct observation of base-pair stepping by RNA polymerase," *Nature 2005 438:7067*, vol. 438, no. 7067, pp. 460–465, Nov. 2005, doi: 10.1038/nature04268.

[35] A. Yildiz, J. N. Forkey, S. A. McKinney, T. Ha, Y. E. Goldman, and P. R. Selvin, "Myosin V walks hand-over-hand: Single fluorophore imaging with 1.5-nm localization," *Science (1979)*, vol. 300, no. 5628, pp. 2061–2065, Jun. 2003, doi: 10.1126/SCIENCE.1084398/SUPPL_FILE/YILDIZ.SOM.PDF.

[36] M. K. Cheezum, W. F. Walker, and W. H. Guilford, "Quantitative comparison of algorithms for tracking single fluorescent

particles," *Biophys J*, vol. 81, no. 4, pp. 2378–2388, Oct. 2001, doi: 10.1016/S0006-3495(01)75884-5.

[37] "ZEISS Microscopy Online Campus | Practical Aspects of Photoactivated Localization Microscopy (PALM)." [Online]. Available: http://zeiss-campus.magnet.fsu.edu/articles/superresolution/palm/practicalaspects.html

[38] S. Stallinga *et al.*, "Accuracy of the Gaussian Point Spread Function model in 2D localization microscopy," *Optics Express, Vol. 18, Issue 24, pp. 24461-24476*, vol. 18, no. 24, pp. 24461–24476, Nov. 2010, doi: 10.1364/OE.18.024461.

[39] R. E. Thompson, D. R. Larson, and W. W. Webb, "Precise nanometer localization analysis for individual fluorescent probes," *Biophys J*, vol. 82, no. 5, pp. 2775–2783, May 2002, doi: 10.1016/S0006-3495(02)75618-X.

[40] K. I. Mortensen, L. S. Churchman, J. A. Spudich, and H. Flyvbjerg, "Optimized localization analysis for single-molecule tracking and super-resolution microscopy," *Nature Methods 2010 7:5*, vol. 7, no. 5, pp. 377–381, Apr. 2010, doi: 10.1038/nmeth.1447.

[41] B. Rieger and S. Stallinga, "The Lateral and Axial Localization Uncertainty in Super-Resolution Light Microscopy," *ChemPhysChem*, vol. 15, no. 4, pp. 664–670, Mar. 2014, doi: 10.1002/CPHC.201300711.

[42] C. S. Smith, N. Joseph, B. Rieger, and K. A. Lidke, "Fast, single-molecule localization that achieves theoretically minimum uncertainty," *Nature Methods 2010 7:5*, vol. 7, no. 5, pp. 373–375, Apr. 2010, doi: 10.1038/nmeth.1449.

[43] A. Yildiz and P. R. Selvin, "Fluorescence Imaging with One Nanometer Accuracy: Application to Molecular Motors," *Acc Chem Res*, vol. 38, no. 7, pp. 574–582, Jul. 2005, doi: 10.1021/ar040136s.

[44] A. Yildiz, J. N. Forkey, S. A. McKinney, T. Ha, Y. E. Goldman, and P. R. Selvin, "Myosin V walks hand-over-hand: Single fluorophore imaging with 1.5-nm localization," *Science (1979)*, vol. 300, no. 5628, pp. 2061–2065, Jun. 2003, doi: 10.1126/science.1084398.

[45] A. Yildiz *et al.*, "Myosin VI steps via a hand-over-hand mechanism with its lever arm undergoing fluctuations when attached to actin," *Journal of Biological Chemistry*, vol. 279, no. 36, pp. 37223–37226, Sep. 2004, doi: 10.1074/jbc.C400252200.

[46] A. Yildiz, M. Tomishige, R. D. Vale, and P. R. Selvin, "Kinesin Walks Hand-Over-Hand," *Science (1979)*, vol. 303, no. 5658, pp. 676–678, Jan. 2004, doi: 10.1126/science.1093753.

[47] M. Lelek *et al.*, "Single-molecule localization microscopy," *Nature Reviews Methods Primers 2021 1:1*, vol. 1, no. 1, pp. 1–27, Jun. 2021, doi: 10.1038/s43586-021-00038-x.

[48] H. P. Kao and A. S. Verkman, "Tracking of single fluorescent particles in three dimensions: use of cylindrical optics to encode particle position," *Biophys J*, vol. 67, no. 3, pp. 1291–1300, Sep. 1994, doi: 10.1016/S0006-3495(94)80601-0.

[49] B. Huang, W. Wang, M. Bates, and X. Zhuang, "Three-dimensional super-resolution imaging by stochastic optical reconstruction microscopy," *Science (1979)*, vol. 319, no. 5864, pp. 810–813, Feb. 2008, doi: 10.1126/science.1153529.

[50] R. Henriques, M. Lelek, E. F. Fornasiero, F. Valtorta, C. Zimmer, and M. M. Mhlanga, "QuickPALM: 3D real-time photoactivation

nanoscopy image processing in ImageJ," *Nature Methods 2010 7:5*, vol. 7, no. 5, pp. 339–340, May 2010, doi: 10.1038/nmeth0510-339.

[51] A. Aristov, B. Lelandais, E. Rensen, and C. Zimmer, "ZOLA-3D allows flexible 3D localization microscopy over an adjustable axial range," *Nature Communications 2018 9:1*, vol. 9, no. 1, pp. 1–8, Jun. 2018, doi: 10.1038/s41467-018-04709-4.

[52] S. R. P. Pavani *et al.*, "Three-dimensional, single-molecule fluorescence imaging beyond the diffraction limit by using a double-helix point spread function," *Proc Natl Acad Sci U S A*, vol. 106, no. 9, pp. 2995–2999, Mar. 2009, doi: 10.1073/pnas.0900245106.

[53] B. Hajj, M. El Beheiry, I. Izeddin, X. Darzacq, and M. Dahan, "Accessing the third dimension in localization-based super-resolution microscopy," *Physical Chemistry Chemical Physics*, vol. 16, no. 31, pp. 16340–16348, Jul. 2014, doi: 10.1039/C4CP01380H.

[54] Y. Shechtman, S. J. Sahl, A. S. Backer, and W. E. Moerner, "Optimal point spread function design for 3D imaging," *Phys Rev Lett*, vol. 113, no. 3, p. 133902, Sep. 2014, doi: 10.1103/PHYSREVLETT.113.133902/FIGURES/3/MEDIUM.

[55] M. F. Juette *et al.*, "Three-dimensional sub–100 nm resolution fluorescence microscopy of thick samples," *Nature Methods 2008 5:6*, vol. 5, no. 6, pp. 527–529, May 2008, doi: 10.1038/nmeth.1211.

[56] S. Abrahamsson *et al.*, "Fast multicolor 3D imaging using aberration-corrected multifocus microscopy," *Nature Methods 2012 10:1*, vol. 10, no. 1, pp. 60–63, Jan. 2013, doi: 10.1038/nmeth.2277.

[57]    E. S. Ward, S. Ram, P. Prabhat, and R. J. Ober, "Improved single particle localization accuracy with dual objective multifocal plane microscopy," *Optics Express, Vol. 17, Issue 8, pp. 6881-6898*, vol. 17, no. 8, pp. 6881–6898, Apr. 2009, doi: 10.1364/OE.17.006881.

[58]    E. Betzig, "Proposed method for molecular optical imaging," *Optics Letters, Vol. 20, Issue 3, pp. 237-239*, vol. 20, no. 3, pp. 237–239, Feb. 1995, doi: 10.1364/OL.20.000237.

[59]    E. Betzig *et al.*, "Imaging intracellular fluorescent proteins at nanometer resolution," *Science (1979)*, vol. 313, no. 5793, pp. 1642–1645, Sep. 2006, doi: 10.1126/SCIENCE.1127344/SUPPL_FILE/BETZIG.SOM.PDF .

[60]    S. T. Hess, T. P. K. Girirajan, and M. D. Mason, "Ultra-high resolution imaging by fluorescence photoactivation localization microscopy," *Biophys J*, vol. 91, no. 11, pp. 4258–4272, Dec. 2006, doi: 10.1529/biophysj.106.091116.

[61]    S. Manley *et al.*, "High-density mapping of single-molecule trajectories with photoactivated localization microscopy," *Nature Methods 2008 5:2*, vol. 5, no. 2, pp. 155–157, Jan. 2008, doi: 10.1038/nmeth.1176.

[62]    O. Rossier *et al.*, "Integrins β1 and β3 exhibit distinct dynamic nanoscale organizations inside focal adhesions," *Nature Cell Biology 2012 14:10*, vol. 14, no. 10, pp. 1057–1067, Sep. 2012, doi: 10.1038/ncb2588.

[63]    M. V. Gudheti *et al.*, "Actin mediates the nanoscale membrane organization of the clustered membrane protein influenza hemagglutinin," *Biophys J*, vol. 104, no. 10, pp. 2182–2192, May 2013, doi: 10.1016/j.bpj.2013.03.054.

[64] G. Fu, T. Huang, J. Buss, C. Coltharp, Z. Hensel, and J. Xiao, "In Vivo Structure of the E. coli FtsZ-ring Revealed by Photoactivated Localization Microscopy (PALM)," *PLoS One*, vol. 5, no. 9, p. e12680, 2010, doi: 10.1371/JOURNAL.PONE.0012680.

[65] Y. Tang *et al.*, "SNSMIL, a real-time single molecule identification and localization algorithm for super-resolution fluorescence microscopy," *Scientific Reports 2015 5:1*, vol. 5, no. 1, pp. 1–13, Jun. 2015, doi: 10.1038/srep11073.

[66] F. V. Subach, G. H. Patterson, S. Manley, J. M. Gillette, J. Lippincott-Schwartz, and V. V. Verkhusha, "Photoactivatable mCherry for high-resolution two-color fluorescence microscopy," *Nat Methods*, vol. 6, no. 2, pp. 153–159, 2009, doi: 10.1038/nmeth.1298.

[67] M. J. Rust, M. Bates, and X. Zhuang, "Sub-diffraction-limit imaging by stochastic optical reconstruction microscopy (STORM)," *Nat Methods*, vol. 3, no. 10, pp. 793–795, Oct. 2006, doi: 10.1038/nmeth929.

[68] R. Wombacher *et al.*, "Live-cell super-resolution imaging with trimethoprim conjugates," *Nature Methods 2010 7:9*, vol. 7, no. 9, pp. 717–719, Aug. 2010, doi: 10.1038/nmeth.1489.

[69] M. Heilemann, S. Van De Linde, A. Mukherjee, and M. Sauer, "Super-Resolution Imaging with Small Organic Fluorophores," *Angewandte Chemie International Edition*, vol. 48, no. 37, pp. 6903–6908, Sep. 2009, doi: 10.1002/ANIE.200902073.

[70] L. Schermelleh, R. Heintzmann, and H. Leonhardt, "A guide to super-resolution fluorescence microscopy," *Journal of Cell Biology*, vol. 190, no. 2, pp. 165–175, Jul. 2010, doi: 10.1083/JCB.201002018.

[71] A. Dani, B. Huang, J. Bergan, C. Dulac, and X. Zhuang, "Superresolution Imaging of Chemical Synapses in the Brain," *Neuron*, vol. 68, no. 5, pp. 843–856, Dec. 2010, doi: 10.1016/j.neuron.2010.11.021.

[72] A. Löschberger *et al.*, "Super-resolution imaging visualizes the eightfold symmetry of gp210 proteins around the nuclear pore complex and resolves the central channel with nanometer resolution," *J Cell Sci*, vol. 125, no. 3, pp. 570–575, Feb. 2012, doi: 10.1242/JCS.098822.

[73] M. Bates, B. Huang, G. T. Dempsey, and X. Zhuang, "Multicolor super-resolution imaging with photo-switchable fluorescent probes," *Science (1979)*, vol. 317, no. 5845, pp. 1749–1753, Sep. 2007, doi: 10.1126/science.1146598.

[74] S. H. Shim *et al.*, "Super-resolution fluorescence imaging of organelles in live cells with photoswitchable membrane probes," *Proc Natl Acad Sci U S A*, vol. 109, no. 35, pp. 13978–13983, Aug. 2012, doi: 10.1073/pnas.1201882109.

[75] A. Benke, N. Olivier, J. Gunzenhäuser, and S. Manley, "Multicolor single molecule tracking of stochastically active synthetic dyes," *Nano Lett*, vol. 12, no. 5, pp. 2619–2624, May 2012, doi: 10.1021/NL301018R/SUPPL_FILE/NL301018R_SI_001.PDF.

[76] S. Wilmes *et al.*, "Triple-Color Super-Resolution Imaging of Live Cells: Resolving Submicroscopic Receptor Organization in the Plasma Membrane," *Angewandte Chemie*, vol. 124, no. 20, pp. 4952–4955, May 2012, doi: 10.1002/ANGE.201200853.

[77] S. A. Jones, S. H. Shim, J. He, and X. Zhuang, "Fast, three-dimensional super-resolution imaging of live cells," *Nature Methods 2011 8:6*, vol. 8, no. 6, pp. 499–505, May 2011, doi: 10.1038/nmeth.1605.

141

[78]  B. Huang, H. Babcock, and X. Zhuang, "Breaking the diffraction barrier: Super-resolution imaging of cells," *Cell*, vol. 143, no. 7. Cell Press, pp. 1047–1058, Dec. 23, 2010. doi: 10.1016/j.cell.2010.12.002.

[79]  M. Bates, B. Huang, and X. Zhuang, "Super-resolution microscopy by nanoscale localization of photo-switchable fluorescent probes," *Current Opinion in Chemical Biology*, vol. 12, no. 5. Elsevier Current Trends, pp. 505–514, Oct. 01, 2008. doi: 10.1016/j.cbpa.2008.08.008.

[80]  G. T. Dempsey, J. C. Vaughan, K. H. Chen, M. Bates, and X. Zhuang, "Evaluation of fluorophores for optimal performance in localization-based super-resolution imaging," *Nat Methods*, vol. 8, no. 12, pp. 1027–1040, Dec. 2011, doi: 10.1038/nmeth.1768.

[81]  H. Shroff, C. G. Galbraith, J. A. Galbraith, and E. Betzig, "Live-cell photoactivated localization microscopy of nanoscale adhesion dynamics," *Nat Methods*, vol. 5, no. 5, pp. 417–423, May 2008, doi: 10.1038/nmeth.1202.

[82]  C. E. Shannon, "Communication in the Presence of Noise," *Proceedings of the IRE*, vol. 37, no. 1, pp. 10–21, 1949, doi: 10.1109/JRPROC.1949.232969.

[83]  "Molecular Density in Super-Resolution Microscopy | Nikon's MicroscopyU." [Online]. Available: https://www.microscopyu.com/tutorials/molecular-density-in-superresolution-microscopy

[84]  "Single-Molecule Super-Resolution Imaging | Nikon's MicroscopyU." Accessed: Aug. 26, 2023. [Online]. Available: https://www.microscopyu.com/techniques/super-resolution/single-molecule-super-resolution-imaging

[85] J. Fölling *et al.*, "Fluorescence nanoscopy by ground-state depletion and single-molecule return," *Nature Methods 2008 5:11*, vol. 5, no. 11, pp. 943–945, Sep. 2008, doi: 10.1038/nmeth.1257.

[86] S. Van De Linde *et al.*, "Direct stochastic optical reconstruction microscopy with standard fluorescent probes," *Nature Protocols 2011 6:7*, vol. 6, no. 7, pp. 991–1009, Jun. 2011, doi: 10.1038/nprot.2011.336.

[87] F. Balzarotti *et al.*, "Nanometer resolution imaging and tracking of fluorescent molecules with minimal photon fluxes," *Science (1979)*, vol. 355, no. 6325, pp. 606–612, Feb. 2017, doi: 10.1126/SCIENCE.AAK9913/SUPPL_FILE/BALZAROTTI_S M.PDF.

[88] S. W. Hell, "Method and apparatus for tracking a particle, particularly a single molecule, in a sample," *Patent application WO 2013/072273 A1 B2*. Google Patents, Mar. 22, 2013.

[89] S. W. Hell, "High-resolution fluorescence microscopy using a structured beam of excitation light," *Patent application WO 2015/0970000 A1*. Google Patents, Aug. 01, 2015.

[90] Y. Eilers, H. Ta, K. C. Gwosch, F. Balzarotti, and S. W. Hell, "MINFLUX monitors rapid molecular jumps with superior spatiotemporal resolution," *Proc Natl Acad Sci U S A*, vol. 115, no. 24, pp. 6117–6122, Jun. 2018, doi: 10.1073/PNAS.1801672115/SUPPL_FILE/PNAS.1801672115. SM02.MP4.

[91] J. K. Pape *et al.*, "Multicolor 3D MINFLUX nanoscopy of mitochondrial MICOS proteins," *Proc Natl Acad Sci U S A*, vol. 117, no. 34, pp. 20607–20614, Aug. 2020, doi: 10.1073/PNAS.2009364117/SUPPL_FILE/PNAS.2009364117. SM07.MP4.

[92] R. Schmidt *et al.*, "MINFLUX nanometer-scale 3D imaging and microsecond-range tracking on a common fluorescence microscope," *Nature Communications 2021 12:1*, vol. 12, no. 1, pp. 1–12, Mar. 2021, doi: 10.1038/s41467-021-21652-z.

[93] C. P. Grabner *et al.*, "Resolving the molecular architecture of the photoreceptor active zone with 3D-MINFLUX," *Sci Adv*, vol. 8, no. 28, p. 7560, Jul. 2022, doi: 10.1126/SCIADV.ABL7560/SUPPL_FILE/SCIADV.ABL7560_MOVIES_S1_TO_S14.ZIP.

[94] K. C. Gwosch *et al.*, "MINFLUX nanoscopy delivers 3D multicolor nanometer resolution in cells," *Nature Methods 2020 17:2*, vol. 17, no. 2, pp. 217–224, Jan. 2020, doi: 10.1038/s41592-019-0688-0.

[95] "MINFLUX: Molecular resolution in 2D and 3D - 2022 - Wiley Analytical Science." Accessed: Aug. 29, 2023. [Online]. Available: https://analyticalscience.wiley.com/do/10.1002/was.000400 0269/

[96] L. M. Ostersehlt *et al.*, "DNA-PAINT MINFLUX nanoscopy," *Nature Methods 2022 19:9*, vol. 19, no. 9, pp. 1072–1075, Sep. 2022, doi: 10.1038/s41592-022-01577-1.

[97] S.-Y. Chen, R. Heintzmann, R. Heintzmann, C. Cremer, C. Cremer, and C. Cremer, "Sample drift estimation method based on speckle patterns formed by backscattered laser light," *Biomedical Optics Express, Vol. 10, Issue 12, pp. 6462-6475*, vol. 10, no. 12, pp. 6462–6475, Dec. 2019, doi: 10.1364/BOE.10.006462.

[98] A. Pertsinidis *et al.*, "Localization events-based sample drift correction for localization microscopy with redundant cross-correlation algorithm," *Optics Express, Vol. 22, Issue 13, pp. 15982-*

*15991*, vol. 22, no. 13, pp. 15982–15991, Jun. 2014, doi: 10.1364/OE.22.015982.

[99]  R. Mcgorty, D. Kamiyama, and B. Huang, "Active microscope stabilization in three dimensions using image correlation," *Opt Nanoscopy*, vol. 2, no. 1, pp. 1–7, Apr. 2013, doi: 10.1186/2192-2853-2-3/FIGURES/5.

[100]  M. J. Mlodzianoski *et al.*, "Sample drift correction in 3D fluorescence photoactivation localization microscopy," *Opt Express*, vol. 19, no. 16, p. 15009, Aug. 2011, doi: 10.1364/oe.19.015009.

[101]  S. Hak Lee *et al.*, "Using fixed fiduciary markers for stage drift correction," *Optics Express, Vol. 20, Issue 11, pp. 12177-12183*, vol. 20, no. 11, pp. 12177–12183, May 2012, doi: 10.1364/OE.20.012177.

[102]  G. Grover *et al.*, "Real-time adaptive drift correction for super-resolution localization microscopy," *Optics Express, Vol. 23, Issue 18, pp. 23887-23898*, vol. 23, no. 18, pp. 23887–23898, Sep. 2015, doi: 10.1364/OE.23.023887.

[103]  A. R. Carter, G. M. King, T. A. Ulrich, W. Halsey, D. Alchenberger, and T. T. Perkins, "Stabilization of an optical microscope to 0.1 nm in three dimensions," *Applied Optics, Vol. 46, Issue 3, pp. 421-427*, vol. 46, no. 3, pp. 421–427, Jan. 2007, doi: 10.1364/AO.46.000421.

[104]  S. Coelho *et al.*, "Ultraprecise single-molecule localization microscopy enables in situ distance measurements in intact cells," *Sci Adv*, vol. 6, no. 16, Apr. 2020, doi: 10.1126/SCIADV.AAY8271/SUPPL_FILE/AAY8271_SM.PDF .

[105] A. Pertsinidis, Y. Zhang, and S. Chu, "Subnanometre single-molecule localization, registration and distance measurements," *Nature 2010 466:7306*, vol. 466, no. 7306, pp. 647–651, Jul. 2010, doi: 10.1038/nature09163.

[106] H. Ma, J. Xu, J. Jin, Y. Huang, and Y. Liu, "A Simple Marker-Assisted 3D Nanometer Drift Correction Method for Superresolution Microscopy," *Biophys J*, vol. 112, no. 10, p. 2196, May 2017, doi: 10.1016/J.BPJ.2017.04.025.

[107] "Huygens CrossTalk Corrector | Scientific Volume Imaging." Accessed: Sep. 06, 2023. [Online]. Available: https://svi.nl/Huygens-CrossTalk-Corrector

[108] D. H. Marimont and B. A. Wandell, "Matching color images: the effects of axial chromatic aberration," *JOSA A, Vol. 11, Issue 12, pp. 3113-3122*, vol. 11, no. 12, pp. 3113–3122, Dec. 1994, doi: 10.1364/JOSAA.11.003113.

[109] L. N. Thibos, A. Bradley, D. L. Still, X. Zhang, and P. A. Howarth, "Theory and measurement of ocular chromatic aberration," *Vision Res*, vol. 30, no. 1, pp. 33–49, Jan. 1990, doi: 10.1016/0042-6989(90)90126-6.

[110] P. B. Kruger, S. Mathews, K. R. Aggarwala, and N. Sanchez, "Chromatic aberration and ocular focus: Fincham revisited," *Vision Res*, vol. 33, no. 10, pp. 1397–1411, Jul. 1993, doi: 10.1016/0042-6989(93)90046-Y.

[111] A. V Kashchuk *et al.*, "Particle Localization Using Local Gradients and Its Application to Nanometer Stabilization of a Microscope," 2022, doi: 10.1021/acsnano.2c09787.

[112] R. Parthasarathy, "Rapid, accurate particle tracking by calculation of radial symmetry centers," *Nature Methods 2012*

*9:7*, vol. 9, no. 7, pp. 724–726, Jun. 2012, doi: 10.1038/nmeth.2071.

[113] F. Long, Z.-L. Huang, H. Ma, and S. Zeng, "Fast and precise algorithm based on maximum radial symmetry for single molecule localization," *Optics Letters, Vol. 37, Issue 13, pp. 2481-2483*, vol. 37, no. 13, pp. 2481–2483, Jul. 2012, doi: 10.1364/OL.37.002481.

[114] S. L. Liu *et al.*, "Fast and High-Accuracy Localization for Three-Dimensional Single-Particle Tracking," *Scientific Reports 2013 3:1*, vol. 3, no. 1, pp. 1–5, Aug. 2013, doi: 10.1038/srep02462.

[115] H. Ma, J. Xu, J. Jin, Y. Gao, L. Lan, and Y. Liu, "Fast and Precise 3D Fluorophore Localization based on Gradient Fitting," *Scientific Reports 2015 5:1*, vol. 5, no. 1, pp. 1–9, Sep. 2015, doi: 10.1038/srep14335.

[116] N. Olivier, D. Keller, P. Gönczy, and S. Manley, "Resolution Doubling in 3D-STORM Imaging through Improved Buffers," *PLoS One*, vol. 8, no. 7, Jul. 2013, doi: 10.1371/journal.pone.0069004.

[117] L. S. Churchman, Z. Ökten, R. S. Rock, J. F. Dawson, and J. A. Spudich, "Single molecule high-resolution colocalization of Cy3 and Cy5 attached to macromolecules measures intramolecular distances through time," *Proc Natl Acad Sci U S A*, vol. 102, no. 5, pp. 1419–1423, Feb. 2005, doi: 10.1073/PNAS.0409487102/SUPPL_FILE/09487FIG5.JPG.

[118] A. Goshtasby, "Image registration by local approximation methods," *Image Vis Comput*, vol. 6, no. 4, pp. 255–261, Nov. 1988, doi: 10.1016/0262-8856(88)90016-9.

[119] J. M. Fitzpatrick, "Fiducial registration error and target registration error are uncorrelated [7261-1]," 2009, doi: 10.1117/12.813601.

[120] C. R. Maurer, J. Michael Fitzpatrick, M. Y. Wang, R. L. Galloway, R. J. Maciunas, and G. S. Allen, "Registration of head volume images using implantable fiducial markers," *IEEE Trans Med Imaging*, vol. 16, no. 4, pp. 447–462, 1997, doi: 10.1109/42.611354.

[121] S. Fields and R. Sternglanz, "The two-hybrid system: an assay for protein-protein interactions," *Trends in Genetics*, vol. 10, no. 8, pp. 286–292, Aug. 1994, doi: 10.1016/0168-9525(90)90012-U.

[122] S. Chioccioli *et al.*, "In vivo evaluation of the interaction between the Escherichia coli IGP synthase subunits using the Bacterial Two-Hybrid system," *FEMS Microbiol Lett*, vol. 367, no. 14, Jul. 2020, doi: 10.1093/femsle/fnaa112.

[123] A. B. Fulton, "How crowded is the cytoplasm?," *Cell*, vol. 30, no. 2, pp. 345–347, 1982, doi: 10.1016/0092-8674(82)90231-8.

[124] C. K. Mathews, "The cell - Bag of enzymes or network of channels?," *J Bacteriol*, vol. 175, no. 20, pp. 6377–6381, 1993, doi: 10.1128/JB.175.20.6377-6381.1993/ASSET/05B05E92-AD02-4316-99AE-E04EA7E56A6A/ASSETS/JB.175.20.6377-6381.1993.FP.PNG.

[125] J. Ovádi and V. Saks, "On the origin of intracellular compartmentation and organized metabolic systems," *Mol Cell Biochem*, vol. 256–257, no. 1–2, pp. 5–12, 2004, doi: 10.1023/B:MCBI.0000009855.14648.2C.

[126] M. Hoppert and F. Mayer, "Principles of macromolecular organization and cell function in bacteria and archaea," *Cell*

*Biochem Biophys*, vol. 31, no. 3, pp. 247–284, 1999, doi: 10.1007/BF02738242.

[127] F. M. Meyer *et al.*, "Physical interactions between tricarboxylic acid cycle enzymes in Bacillus subtilis: evidence for a metabolon," *Metab Eng*, vol. 13, no. 1, pp. 18–27, Jan. 2011, doi: 10.1016/J.YMBEN.2010.10.001.

[128] X. Weng and J. Xiao, "Spatial organization of transcription in bacterial cells," *Trends Genet*, vol. 30, no. 7, pp. 287–297, 2014, doi: 10.1016/J.TIG.2014.04.008.

[129] S. B. Zimmerman and S. O. Trach, "Estimation of macromolecule concentrations and excluded volume effects for the cytoplasm of Escherichia coli," *J Mol Biol*, vol. 222, no. 3, pp. 599–620, Dec. 1991, doi: 10.1016/0022-2836(91)90499-V.

[130] P. A. Srere, "Complexes of sequential metabolic enzymes," *Annu Rev Biochem*, vol. 56, pp. 89–124, 1987, doi: 10.1146/ANNUREV.BI.56.070187.000513.

[131] F. Haas, M. B. Mitchell, B. N. Ames A N D, and H. K. Mitchell, "A SERIES OF HISTIDINELESS MUTANTS OF NEUROSPORA CRASSA," *Genetics*, vol. 37, no. 3, pp. 217–226, May 1952, doi: 10.1093/GENETICS/37.3.217.

[132] P. Alifano *et al.*, "Histidine biosynthetic pathway and genes: structure, regulation, and evolution.," *Microbiol Rev*, vol. 60, no. 1, p. 44, Mar. 1996, doi: 10.1128/MR.60.1.44-69.1996.

[133] M. Brilli and R. Fani, "The origin and evolution of eucaryal HIS7 genes: From metabolon to bifunctional proteins?," *Gene*, vol. 339, no. 1–2, pp. 149–160, Sep. 2004, doi: 10.1016/j.gene.2004.06.033.

[134] R. A. Jensen and S. Ahmad, "Nested gene fusions as markers of phylogenetic branchpoints in prokaryotes," *Trends Ecol Evol*,

vol. 5, no. 7, pp. 219–224, 1990, doi: 10.1016/0169-5347(90)90135-Z.

[135] I. Yanai, A. Derti, and C. DeLisi, "Genes linked by fusion events are generally of the same functional category: a systematic analysis of 30 microbial genomes," *Proc Natl Acad Sci U S A*, vol. 98, no. 14, pp. 7940–7945, 2001, doi: 10.1073/PNAS.141236298.

[136] M. C. Papaleo *et al.*, "Structural, evolutionary and genetic analysis of the histidine biosynthetic 'core' in the genus Burkholderia," *Gene*, vol. 448, no. 1, pp. 16–28, Dec. 2009, doi: 10.1016/J.GENE.2009.08.002.

[137] M. Touchon and E. P. C. Rocha, "Coevolution of the Organization and Structure of Prokaryotic Genomes," *Cold Spring Harb Perspect Biol*, vol. 8, no. 1, p. a018168, Jan. 2016, doi: 10.1101/CSHPERSPECT.A018168.

[138] J. Tamames, "Evolution of gene order conservation in prokaryotes.," *Genome Biol*, vol. 2, no. 6, pp. 1–11, Jun. 2001, doi: 10.1186/GB-2001-2-6-RESEARCH0020/TABLES/1.

[139] M. Fondi, G. Emiliani, and R. Fani, "Origin and evolution of operons and metabolic pathways," *Res Microbiol*, vol. 160, no. 7, pp. 502–512, Sep. 2009, doi: 10.1016/J.RESMIC.2009.05.001.

[140] T. Dandekar, B. Snel, M. Huynen, and P. Bork, "Conservation of gene order: a fingerprint of proteins that physically interact," *Trends Biochem Sci*, vol. 23, no. 9, pp. 324–328, Sep. 1998, doi: 10.1016/S0968-0004(98)01274-2.

[141] R. T. Dame, F. Z. M. Rashid, and D. C. Grainger, "Chromosome organization in bacteria: mechanistic insights into genome structure and function," *Nat Rev Genet*, vol. 21, no. 4, pp. 227–242, Apr. 2020, doi: 10.1038/S41576-019-0185-4.

150

[142] J. A. Bryant, L. E. Sellars, S. J. W. Busby, and D. J. Lee, "Chromosome position effects on gene expression in Escherichia coli K-12," *Nucleic Acids Res*, vol. 42, no. 18, pp. 11383–11392, Oct. 2014, doi: 10.1093/NAR/GKU828.

[143] P. Sengupta, T. Jovanovic-Talisman, and J. Lippincott-Schwartz, "Quantifying spatial organization in point-localization superresolution images using pair correlation analysis," *Nature Protocols 2012 8:2*, vol. 8, no. 2, pp. 345–354, Jan. 2013, doi: 10.1038/nprot.2013.005.

[144] "VII. Mathematical contributions to the theory of evolution.—III. Regression, heredity, and panmixia," *Philosophical Transactions of the Royal Society of London. Series A, Containing Papers of a Mathematical or Physical Character*, vol. 187, pp. 253–318, Dec. 1896, doi: 10.1098/RSTA.1896.0007.

[145] E. M. M. MANDERS, F. J. VERBEEK, and J. A. ATEN, "Measurement of co-localization of objects in dual-colour confocal images," *J Microsc*, vol. 169, no. 3, pp. 375–382, Mar. 1993, doi: 10.1111/J.1365-2818.1993.TB03313.X.

[146] J. Rossy, E. Cohen, K. Gaus, and D. M. Owen, "Method for co-cluster analysis in multichannel single-molecule localisation data," *Histochem Cell Biol*, vol. 141, no. 6, pp. 605–612, Mar. 2014, doi: 10.1007/S00418-014-1208-Z/FIGURES/5.

[147] S. Malkusch, U. Endesfelder, J. Mondry, M. Gelléri, P. J. Verveer, and M. Heilemann, "Coordinate-based colocalization analysis of single-molecule localization microscopy data," *Histochem Cell Biol*, vol. 137, no. 1, pp. 1–10, Jan. 2012, doi: 10.1007/S00418-011-0880-5/FIGURES/8.

[148] F. Levet *et al.*, "A tessellation-based colocalization analysis approach for single-molecule localization microscopy," *Nature*

*Communications 2019 10:1*, vol. 10, no. 1, pp. 1–12, May 2019, doi: 10.1038/s41467-019-10007-4.

[149] J. H. Chen, T. A. Blanpied, and A. H. Tang, "Quantification of trans-synaptic protein alignment: A data analysis case for single-molecule localization microscopy," *Methods*, vol. 174, pp. 72–80, Mar. 2020, doi: 10.1016/J.YMETH.2019.07.016.

[150] A. H. Tang, H. Chen, T. P. Li, S. R. Metzbower, H. D. MacGillavry, and T. A. Blanpied, "A trans-synaptic nanocolumn aligns neurotransmitter release to receptors," *Nature 2016 536:7615*, vol. 536, no. 7615, pp. 210–214, Jul. 2016, doi: 10.1038/nature19058.

[151] S. V. Pageon, P. R. Nicovich, M. Mollazade, T. Tabarin, and K. Gaus, "Clus-DoC: A combined cluster detection and colocalization analysis for single-molecule localization microscopy data," *Mol Biol Cell*, vol. 27, no. 22, pp. 3627–3636, Nov. 2016, doi: 10.1091/MBC.E16-07-0478/ASSET/IMAGES/LARGE/MBC-27-3627-G007.JPEG.

[152] J. Willems and H. D. MacGillavry, "A coordinate-based co-localization index to quantify and visualize spatial associations in single-molecule localization microscopy," *Scientific Reports 2022 12:1*, vol. 12, no. 1, pp. 1–12, Mar. 2022, doi: 10.1038/s41598-022-08746-4.

[153] D. Bourgeois, "Single molecule imaging simulations with advanced fluorophore photophysics," *Communications Biology 2023 6:1*, vol. 6, no. 1, pp. 1–13, Jan. 2023, doi: 10.1038/s42003-023-04432-x.

[154] F. Chen, P. W. Tillberg, and E. S. Boyden, "Expansion microscopy," *Science (1979)*, vol. 347, no. 6221, pp. 543–548, Jan. 2015, doi: 10.1126/science.1260088.

[155] T. J. Chozinski *et al.*, "Expansion microscopy with conventional antibodies and fluorescent proteins," *Nat Methods*, vol. 13, no. 6, pp. 485–488, Jun. 2016, doi: 10.1038/nmeth.3833.

[156] P. W. Tillberg *et al.*, "Protein-retention expansion microscopy of cells and tissues labeled using standard fluorescent proteins and antibodies," *Nat Biotechnol*, vol. 34, no. 9, pp. 987–992, Sep. 2016, doi: 10.1038/nbt.3625.

[157] Y. Fan *et al.*, "Mechanical expansion microscopy," *Methods Cell Biol*, vol. 161, pp. 125–146, Jan. 2021, doi: 10.1016/BS.MCB.2020.04.013.

[158] V. Middelhauve, J. P. Siebrasse, and U. Kubitscheck, "Expansion Microscopy of Bacillus subtilis," *Methods in Molecular Biology*, vol. 2601, pp. 191–202, 2023, doi: 10.1007/978-1-0716-2855-3_10/COVER.

[159] L. Gardini, T. Vignolini, V. Curcio, F. S. Pavone, and M. Capitanio, "Optimization of highly inclined illumination for diffraction-limited and super-resolution microscopy," *Optics Express, Vol. 31, Issue 16, pp. 26208-26225*, vol. 31, no. 16, pp. 26208–26225, Jul. 2023, doi: 10.1364/OE.492152.

[160] T. C. Kunz *et al.*, "The Expandables: Cracking the Staphylococcal Cell Wall for Expansion Microscopy," *Front Cell Infect Microbiol*, vol. 11, p. 644750, Mar. 2021, doi: 10.3389/FCIMB.2021.644750/BIBTEX.

[161] "ThunderSTORM: a comprehensive ImageJ plug-in for PALM and STORM data analysis and super-resolution imaging | Bioinformatics | Oxford Academic." Accessed: Mar. 02, 2020. [Online]. Available: https://academic.oup.com/bioinformatics/article/30/16/2389/2748167

[162] J. Schindelin *et al.*, "Fiji: An open-source platform for biological-image analysis," *Nature Methods*, vol. 9, no. 7. Nature Publishing Group, pp. 676–682, Jul. 28, 2012. doi: 10.1038/nmeth.2019.

[163] C. A. Schneider, W. S. Rasband, and K. W. Eliceiri, "NIH Image to ImageJ: 25 years of image analysis," *Nature Methods*, vol. 9, no. 7. Nature Publishing Group, pp. 671–675, Jul. 28, 2012. doi: 10.1038/nmeth.2089.

[164] E. M. Kudalkar, T. N. Davis, and C. L. Asbury, "Single-Molecule Total Internal Reflection Fluorescence Microscopy," *Cold Spring Harb Protoc*, vol. 2016, no. 5, p. pdb.top077800, May 2016, doi: 10.1101/PDB.TOP077800.

[165] M. Tokunaga, N. Imamoto, and K. Sakata-Sogawa, "Highly inclined thin illumination enables clear single-molecule imaging in cells," *Nat Methods*, vol. 5, no. 2, pp. 159–161, Feb. 2008, doi: 10.1038/nmeth1171.

[166] N. Durisic, L. Laparra-Cuervo, Á. Sandoval-Álvarez, J. S. Borbely, and M. Lakadamyali, "Single-molecule evaluation of fluorescent protein photoactivation efficiency using an in vivo nanotemplate," *Nature Methods 2013 11:2*, vol. 11, no. 2, pp. 156–162, Jan. 2014, doi: 10.1038/nmeth.2784.